

AEROSPACE RESEARCH IN BULGARIA

Founded in 1978

Volume 29, Sofia, 2017
Space Research and Technology Institute
Bulgarian Academy of Sciences

Editorial Board

Prof. Garo Mardirossian (*Editor-in-Chief*)
Assoc. Prof. Lachezar Filchev (*English Language Editor*)
Tsveta Srebrova, MS (*Technical Editor*)

Acad. Valeri Bondour – Russia
Prof. Gerassimos Papadopoulos – Greece
Prof. Stefano Tinti – Italy
Assoc. Prof. Premysl Štych – Czech Republic
Corr. Member Petar Getsov
Corr. Member Filip Filipov
Corr. Member Petar Velinov
Prof. Petko Nenovski
Prof. Eugenia Roumenina
Prof. Dimitar Teodossiev
Assoc. Prof. Tania Ivanova
Assoc. Prof. Lachezar Filipov
Assoc. Prof. Bozhidar Srebrov

Address

AEROSPACE RESEARCH IN BULGARIA
Space Research and Technology Institute
Acad. Georgi Bonchev St., block 1, 1113 Sofia, Bulgaria

web-site: <http://journal.space.bas.bg>
e-mail: journal@space.bas.bg

Pre-Publication Processing
Tsveta Srebrova

© Space Research and Technology Institute – Bulgarian Academy of Sciences

p-ISSN 1313 – 0927

e-ISSN 2367 – 9522

This issue of *Aerospace Research in Bulgaria* is published with financial support from the Bulgarian National Science Fund – Contract No ДНП 06/44 – 20.12.2017

Aerospace Research in Bulgaria

29

Sofia, 2017

C o n t e n t s

1. *Alexander Shibaev*
CONNECTION BETWEEN PERIOD OF LOW-FREQUENCY COMPONENT
WOLF'S NUMBERS (WNS) AND LENGTH OF WOLF'S NUMBERS SERIES. . . . 5
2. *Dimitrinka Tomova, Peter Velinov, Yordan Tassev*
COMPARISON BETWEEN EXTREME SOLAR ACTIVITY DURING
PERIODS MARCH 15-17, 2015 AND SEPTEMBER 4-10, 2017
AT DIFFERENT PHASES OF SOLAR CYCLE 24. 10
3. *Yana Asenovska, Simeon Asenovski*
HIGH SPEED SOLAR WIND STREAMS OVER THE LAST FOUR SOLAR
CYCLES. 30
4. *Ivan Yanev*
SATELLITE SENSORS USED IN THERMAL REMOTE SENSING. 35
5. *Ivan Yanev, Lachezar Filchev*
ASSESSMENT OF THE LAND SURFACE TEMPERATURE DYNAMICS
IN THE CITY OF SOFIA USING LANDSAT SATELLITE DATA. 45
6. *Ilina Kamenova, Lachezar Filchev, Iliana Ilieva*
REVIEW OF SPECTRAL VEGETATION INDICES AND METHODS
FOR ESTIMATION OF CROP BIO PHYSICAL VARIABLES. 72
7. *Dimitar Dimitrov*
SPACE TECHNOLOGIES FOR STUDYING AND MONITORING
OF SEISMOGENIC ZONES. 83

8.	<i>Petar Getsov, Wang Bo, Dimo Zafirov, Georgi Sotirov, Stanimir Nachev, Ruslan Yanev, Pavlin Gramatikov, Valentin Atanassov, Hristo Lukarski, Svetoslav Zabunov</i>	
	AN UNMANNED AERIAL SURVEILLANCE SYSTEM IN URBAN ENVIRONMENTS.....	94
9.	<i>Petar Getsov, Wang Bo, Svetoslav Zabunov, Garo Mardirossian</i>	
	INNOVATIONS IN THE AREA OF UNMANNED AERIAL VEHICLES.....	111
10.	<i>Pavlin Gramatikov</i>	
	ELECTRIC MOTOR-GENERATORS FOR UNMANNED AERIAL VEHICLES.....	120
11.	<i>Boris Hotinov, Pavlin Gramatikov</i>	
	ONBOARD DIGITAL BLOCK FOR ELECTRIC FIELD MEASUREMENTS IN SPACE.....	133
12.	<i>Konstantin Metodiev</i>	
	GENERATING A PULSE-WIDTH MODULATED SIGNAL BY MEANS OF TIMER MODULE INTERRUPT OF PIC18F2550 MCU.....	141
13.	<i>Peter I. Y. Velinov</i>	
	DEVELOPMENT OF ADVANCED SPACE SCIENCES AFTER FIRST ARTIFICIAL SATELLITE. 60-TH ANNIVERSARY OF THE SPACE AGE....	147

С Ъ Д Ъ Р Ж А Н И Е

1. *Александр Шибаев*
ЗАВИСИМОСТЪ ПЕРИОДА «ВЕКОВОЙ» ГАРМОНИКИ РЯДА ЧИСЕЛ
ВОЛЬФА ОТ ДЛИНЫ ИССЛЕДУЕМОГО РЯДА. 5
2. *Димитринка Томова, Петър Велинов, Йордан Тасев*
СРАВНЕНИЕ МЕЖДУ ИЗВЪНРЕДНАТА СЛЪНЧЕВА АКТИВНОСТ
В ПЕРИОДИТЕ 15–17 МАРТ 2015 И 4–10 СЕПТЕМВРИ 2017
В РАЗЛИЧНИ ФАЗИ НА 24-ТИ СЛЪНЧЕВ ЦИКЪЛ. 10
3. *Яна Асеновска, Симеон Асеновски*
ВИСОКОСКОРОСТНИ ПОТОЦИ БЪРЗ СЛЪНЧЕВ ВЯТЪР ПРЕЗ
ПОСЛЕДНИТЕ ЧЕТИРИ СЛЪНЧЕВИ ЦИКЪЛА. 30
4. *Иван Янев*
СПЪТНИКОВИ СЕНЗОРИ, ИЗПОЛЗВАНИ ЗА ТОПЛИННИ
ДИСТАНЦИОННИ ИЗСЛЕДВАНИЯ. 35
5. *Иван Янев, Лъчезар Филчев*
ОЦЕНКА НА ДИНАМИКАТА НА ТЕМПЕРАТУРАТА НА ЗЕМНАТА
ПОВЪРХНОСТ НА ГРАД СОФИЯ С ИЗПОЛЗВАНЕ НА СПЪТНИКОВИ
ДАННИ ОТ ЛАНДСАТ. 45
6. *Илина Каменова, Лъчезар Филчев, Илиана Илиева*
ОБЗОР НА ИНДЕКСИТЕ И МЕТОДИТЕ ЗА ИЗСЛЕДВАНЕ
НА БИОФИЗИЧНИ ПРОМЕНЛИВИ НА ЗЕМЕДЕЛСКИ КУЛТУРИ. 72
7. *Димитър Димитров*
КОСМИЧЕСКИ ТЕХНОЛОГИИ ПРИ ИЗСЛЕДВАНЕ И МОНИТОРИНГ
НА СЕИЗМОГЕННИ ЗОНИ. 83
8. *Петър Гецов, Ванг Бо, Димо Зафиров, Георги Сотиров,
Станимир Начев, Руслан Янев, Павлин Граматиков,
Валентин Атанасов, Христо Лукарски, Светослав Забунов*
БЕЗПИЛОТНА СИСТЕМА ЗА НАБЛЮДЕНИЕ В ГРАДСКА СРЕДА. 94
9. *Петър Гецов, Ванг Бо, Светослав Забунов, Гаро Мардиросян*
ИНОВАЦИИ В ОБЛАСТТА НА БЕЗПИЛОТНИ ЛЕТАТЕЛНИ АПАРАТИ. . 111
10. *Павлин Граматиков*
ЕЛЕКТРИЧЕСКИ МОТОР-ГЕНЕРАТОРИ ЗА БЕЗПИЛОТНИ
ЛЕТАТЕЛНИ СРЕДСТВА. 120

11. ***Борис Хотинов, Павлин Граматиков***
БОРДЕН ЦИФРОВ БЛОК ЗА ИЗМЕРВАНЕ НА КОСМИЧЕСКО
ЕЛЕКТРИЧЕСКО ПОЛЕ.133
12. ***Константин Методиев***
ГЕНЕРИРАНЕ НА ШИРОЧИННОИМПУЛСНО МОДУЛИРАН СИГНАЛ
ЧРЕЗ ПРЕКЪСВАНЕ ОТ ТАЙМЕР НА МИКРОКОНТРОЛЕР PIC18F2550. . .141
13. ***Петър Велинов***
РАЗВИТИЕ НА СЪВРЕМЕННИТЕ КОСМИЧЕСКИ НАУКИ
СЛЕД ПЪРВИЯ ИЗКУСТВЕН СПЪТНИК НА ЗЕМЯТА.
60 ГОДИШНИНА НА КОСМИЧЕСКАТА ЕРА.147

CONNECTION BETWEEN PERIOD OF LOW-FREQUENCY COMPONENT WOLF'S NUMBERS (WNS) AND LENGTH OF WOLF'S NUMBERS SERIES

Alexander Shibaev

“Lomonosov” Moscow State University, Faculty of Mechanics and Mathematics

Abstract

The long-period component of Sun's activity and Gleissberg cycle are in focus of this work. The main reason is they affect daily life on Earth, for instance minimum and maximum ages change each other. For the last 60 years, many researchers have been considering that period of Gleissberg cycle limit is 80 and 110 years. Some of them consider 88 years specifically. Different researchers were analyzing WNS in different time, so they had different row length. It makes sense to analyze dependence between WNS length and period of approximation sine of low-frequency component Wolf's numbers.

Monthly Wolf number since 1749 is analyzed, the shortest part of WNS includes 18 cycles (from 1749 to 1954.37) and the longest line includes a part of a cycle No 24 (1749-2014.376). It's noticed that during increasing WNS's length, sine approximation period also increases from 84 years up to 110 years. The eighty eight years period appears at several conditions.

Because of increasing period of approximation sine it's rather difficult to extrapolate sine at the future time. It should be noticed that in case of analyzing part of WNS since 1849÷2015 a reliable part, period of sine approximation equals 150 years. The problem concerning matching reliable part of WNS and reconstructed part remains open.

Introduction

Sustainable interest in long-period cycles of solar phenomena, which includes the Gleisberg cycle, is associated with the manifestation of eras of the phenomena maximum or minimum in everyday life. In the works of various authors written for the last 60 years, its period is estimated within 80÷110 years. A number of researchers point out certain value of the period of the Gleisberg cycle which equals to 88 years. As various authors have analysed the Wolf numbers sequence of different lengths, it makes sense to investigate influence of length of sequence on an approximating sine of a long-period component of Wolf numbers sequence.

A minimum length of the fragment under investigation is eighteen cycles (1749÷1954.37 yy); a maximum length is 24 to a cycle maximum (1749÷2014.376 yy). It is noted that once the sequence length increases the period of a sine increases from 84 to 110 years, and the 88-year period comes out under certain conditions [1]. The unstable (growing) valuation of the "century" harmonic

curve period being obtained in the work complicates its extrapolation on an external time interval.

Sine approximation

At the present day the Zurich sequence of average monthly Wolf numbers W is the most representative and is widely used in various applications. Quite a complete review of these questions is presented in the monograph [2] and the review [3]. We would like to remind, that sequence of average monthly numbers W includes a sequence of the regular instrumental observations since 1849 till present – a reliable sequence W_{tool} , and a sequence of the restored values from 1749 to 1849 - a sequence W_{rest} ($W=W_{rest} \cup W_{tool}$). In the work [4] are noted the considerable characteristics differences, when comparing the properties of the sequences W_{rest} and W_{tool} . This work is based on a long-period component $P1$ of the sequence W^* (a modified sequence of monthly Wolf numbers) since 1749, which are presented on the Fig. 1.

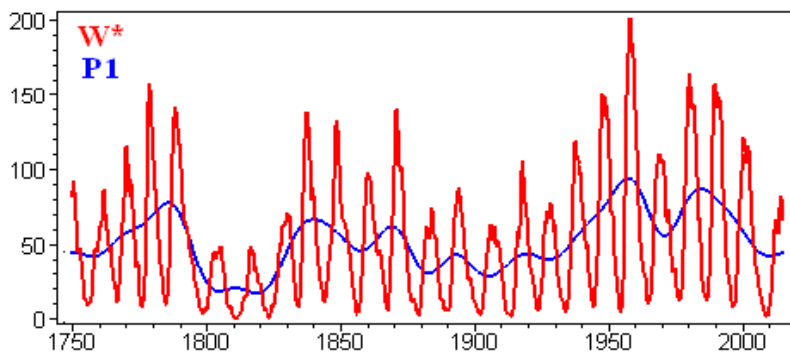


Fig. 1. A modified sequence of monthly Wolf numbers W^ and a long-period component $P1$*

On Fig. 2 is presented the result of approximation of two options of long-period components by a sine: from 1749 to 1954.37 and from 1749 to 2014.376. The sine parameters, the period and the phase, were adjusted by the least square method, i.e. by the minimum value of a result when scanning the concerned sequences by a sine. The period was tested within 50÷200 years, the phase $0 \div 2\pi$. The studied sequences were commensurately scaled beforehand, i.e. after a subtraction of the mean value they were normalized on a root mean square. The 84-years period is allocated for the first sequence, for the second sequence is allocated the 110-years period.

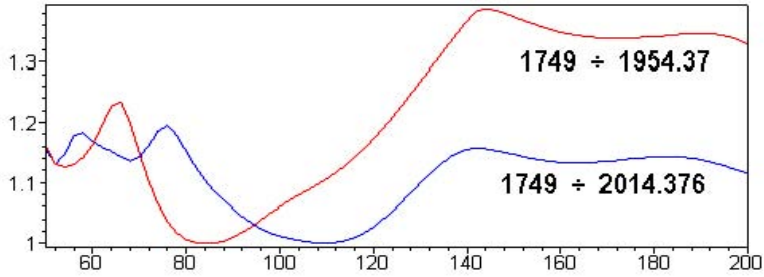


Fig. 2. Result of approximation of two options of long-period components by a sine; the axis OX – sine's period.

The Fig. 3 depicts the dependence of an approximating sine period (vertical axis advanced in years) on length of a sequence; the date of the last sequence point on an axis OX is postponed. The situations of optimum approximation of a long-period component are expressly discernible by the 88-year harmonic curve. The increase of the period after the 20th cycle, i.e. increase in proportion of a reliable data in the sequence W is also notable. It speaks well to the mismatch of characteristics of the restored and certain sequences.

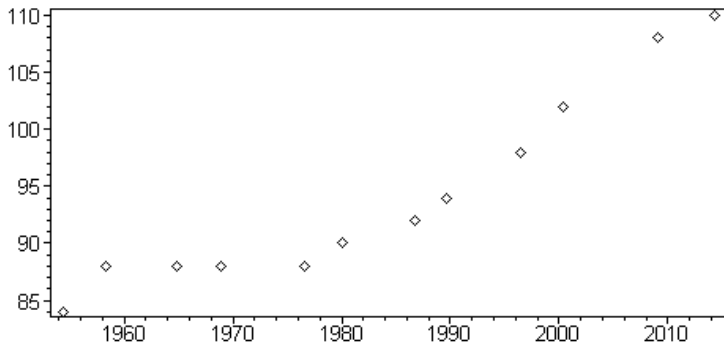


Fig. 3. Dependence of an approximating sine period on length of a W^* sequence.

We would also like to note, that as the long-period component of only a reliable part of a sequence was approximated, and the period of a sine was 150 years [4].

Conclusion

In conclusion we would like to illustrate the degree of coherence of the sequence W with the 88-year harmonic curve. Basing on the optimum

characteristics "frequency phase" for the sequence 1749÷1968.958 (to the maximum of the cycle 20) the approximating sequence is comparable to W numbers sequence Fig. 4. The local character of manifestation of the 88-year harmonic curve is clearly notable.

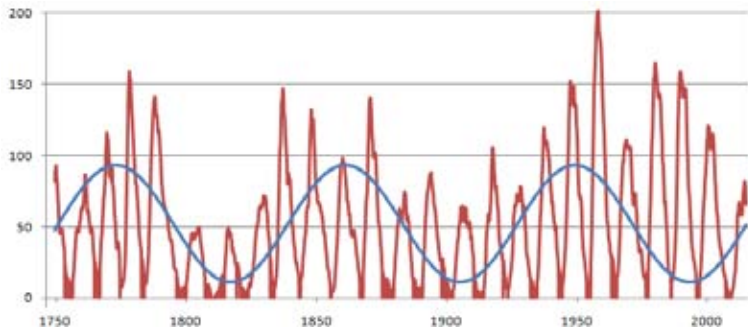


Fig. 4. Comparing 88-year harmonic curve and Wolf numbers W^*

Gleisberg evaluated the period of the maxima envelope of solar cycles as early as in 1955 in the work [5]. The sequence W , by which the researchers were guided at that time, included no more than 18 cycles, a half of which refers to the restored part of the Wolf number sequence, the soundness of which calls on question. As the ratio of lengths of the W_{rest} and the W_{tool} influences the estimation value, it is logical that the different values were obtained for a "century" sequence component in works of different researchers written at different times. Range of these estimations variance conforms well to the ones received in this work.

References

1. Feynman, J., B. Gabriel Stephen. Period and phase of the 88-year Solar cycle and the Maunder minimum: evidence for a chaotic Sun, *Solar Physics*, 1990, 127 (2), pp. 393–403.
2. Витинский, Ю. И., М. Копецкий, Г. В. Куклин. Статистика пятнообразовательной деятельности Солнца. М.: Наука, 1986, 296 с.
3. Иванов-Холодный, Г. С., В. Е. Чертопруд. Солнечная активность, Исследование космического пространства, 1990, 33, с. 3–99. (Итоги науки и техники. ВИНТИ АН СССР.)
4. Shibaev, I. G. Estimation of the Reconstructed Part of the Wolf Series and the Possibility of its Correction, *Solar System Research*, 42, 1, 2008, pp. 63–72. DOI: 10.1134/S0038094608010073.
5. Gleisberg, W. Publ. Istanbul Univ. Obs. 57, 1955.

ЗАВИСИМОСТЬ ПЕРИОДА „ВЕКОВОЙ“ ГАРМОНИКИ РЯДА ЧИСЕЛ ВОЛЬФА ОТ ДЛИНЫ ИССЛЕДУЕМОГО РЯДА

Ал. Шубаев

Резюме

Устойчивый интерес к длиннопериодным циклам солнечной активности, в том числе к циклу Гляйсберга, связан с проявлением эпох максимума или минимума активности в повседневной жизни. В работах разных авторов, сделанных за последние 60 лет, его период оценивается в пределах 80÷110 лет. Ряд исследователей выделяют конкретное значение периода цикла Гляйсберга равное 88 годам [1]. Так как разные авторы анализировали ряд чисел Вольфа различной длины, то имеет смысл исследовать влияние длины самого ряда на период аппроксимирующего синуса длиннопериодной компоненты ряда чисел Вольфа.

Минимальная длина исследуемого фрагмента – восемнадцать циклов (1749÷1954.37 г.), максимальная длина – до максимума цикла 24 (1749÷2014.376 г.). Отмечено, что при увеличении длины ряда период синуса возрастает с 84 лет до 110 лет, а 88-летний период проявляется при определенных условиях. Полученная в работе неустойчивая (растущая) оценка периода «вековой» гармонике затрудняет экстраполяцию её на внешний временной интервал.

COMPARISON BETWEEN EXTREME SOLAR ACTIVITY DURING PERIODS MARCH 15-17, 2015 AND SEPTEMBER 4-10, 2017 AT DIFFERENT PHASES OF SOLAR CYCLE 24

Dimitrinka Tomova¹, Peter I. Y. Velinov², Yordan Tassev²

¹*Sofia University "St. Kliment Ohridski", Sofia
e-mail: tomova@fmi.uni-sofia.bg*

²*Space Research and Technology Institute – Bulgarian Academy of Sciences
e-mails: pvelinov@bas.bg, yktassev@bas.bg*

Abstract

Some of the most powerful Earth's directed coronal mass ejections (CMEs) from the current 24 solar cycle have been investigated. These are CMEs on 15 March 2015 and on September 4, 6 and 10, 2017. As a result of these impacts of Sun on Earth, the highest intensity of the geomagnetic storms for the 24th solar cycle is observed. These G4 - Severe geomagnetic storms are in the periods March 17–19, 2015 and September 7–10, 2017.

We use the solar wind parameters (velocity V , density or concentration N , temperature T_p and intensity of the magnetic field B) from measurements by WIND, ACE and SOHO spacecrafts in the Lagrange equilibrium point L1 between Sun and Earth. We make calculations for the kinetic (dynamic) energy density E_k , thermal energy density E_t and magnetic energy density E_m during the investigated periods May 10–24, 2015 and September 2–16, 2017. Both the energy densities for the individual events and the cumulative energy for each of them are evaluated.

The quantitative analysis shows that not always the size of the geomagnetic reaction is commensurate with the density of the energy flux reaching the magnetosphere. In both studied periods, the energy densities have different behavior over time. But for both periods, we can talk about the prognostic effect - with varying degrees of increase of the dynamic and thermal energies. Such an effect is not observed in the density of magnetic energy.

An interesting state of Forbush decreases in the galactic cosmic ray (GCR) intensity is recorded. In cases of higher energy density there is a lower percentage of GCR in March 2015. Again, at a lower energy density, there is a greater reduction of the GCRs in September 2017.

Introduction

In the second half of the current 24th solar cycle (2009–2019) (Fig. 1), when solar activity begins to decrease, there are several powerful Coronal Mass Ejections (CMEs) [1, 2]. These are the CMEs on March 15, 2015 (2015 St. Patrick's Day storm) and on September 4, 6 and 10, 2017 [2, 3]. It is characteristic of them that these CEMs are directed to the Earth. The first one is in the phase of maximum of solar activity and the others in the solar minimum. Both groups CMEs

are accompanied by G4 - Severe geomagnetic storms. They develop about 2 days after the respective CME – on 17–19 March 2015 and 7–8 September 2017.

The CMEs are huge explosions of magnetic field and plasma from the Sun's corona. When CMEs impact the Earth's magnetosphere, they are responsible for geomagnetic storms and enhanced aurora. CMEs originate from highly twisted magnetic field structures, or "flux ropes", on the Sun, often visualized by their associated "filaments" or "prominences", which are relatively cool plasmas trapped in the flux ropes in the corona. When these flux ropes erupt from active regions on the Sun (regions associated with sunspots and very strong magnetic fields), they are often accompanied by large solar flares; eruptions from quiet regions of the Sun, such as the "polar crown" filament eruptions, sometimes do not have accompanying flares [4, 5].

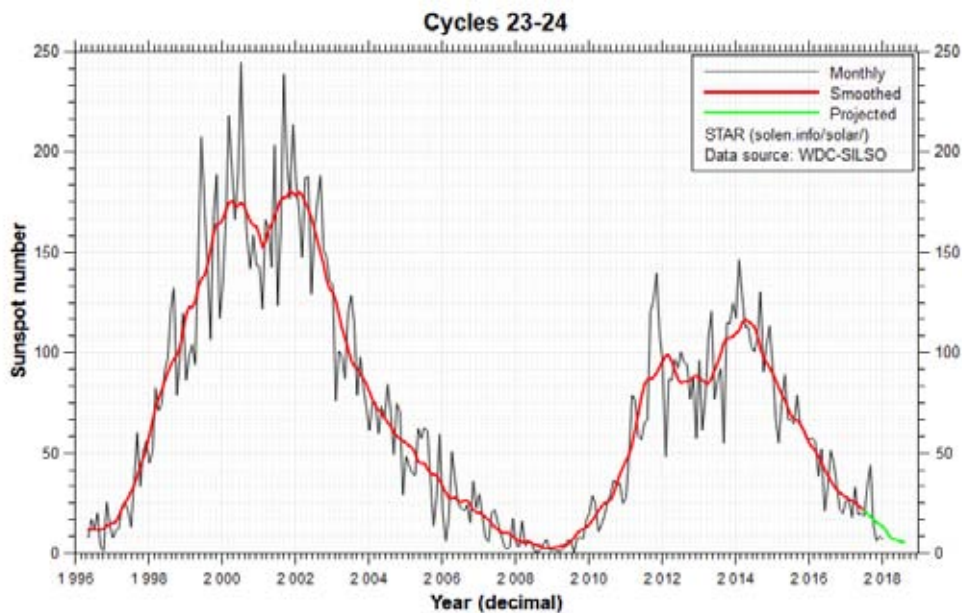


Fig. 1. Distribution of the sunspot numbers in 23 and 24 solar cycles [1].

In the present work will made a comparison between the physical events and the situation in solar-terrestrial environment during the two CME periods under review. Calculations of the solar wind parameters from measurements by WIND, ACE and SOHO spacecrafts in the point of Lagrange will be made: the kinetic (dynamic) energy density E_k , thermal energy density E_t and magnetic energy density E_m during the investigated periods May 10–24, 2015 and September 2–16, 2017. Evidence of geoefficiency [6–8] of these parameters will be provided.

Coronal mass ejection (CME) on March 15, 2015 in solar maximum

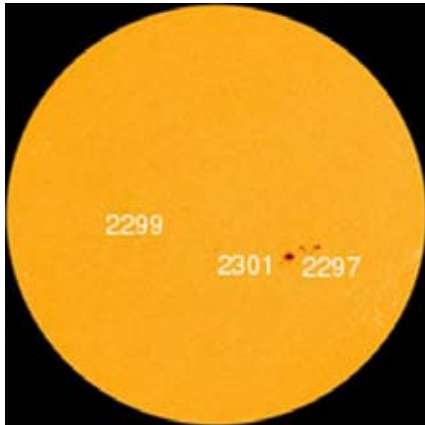


Fig. 2. a) Solar Active Region AR2297 on March 15, 2015

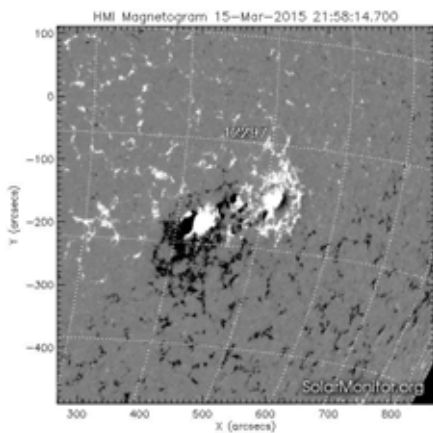


Fig. 2. b) The "beta-gamma-delta" local magnetic field of Active Region AR2297 (Fig. 2a)

The Active Region AR2297 (Fig. 2a), despite its modest size, became the most flare active region of the year 2015. It produced more than 20 M-class flares and 1 X-class event, the latter on 11 March. On 15 March, the region produced a rather moderate, but 2-hour long C9 flare which was accompanied by a fast partial halo CME with an Earth-directed component.

As expected, the CME hit Earth early on Saint Patrick's day, sparking the most intense geomagnetic storm of the current solar cycle ($Kp = 8$; $Ap = 108$; $Dst = -223$ nT) so far.

As early as March 11, 2015 the Active Region AR2297 (Fig. 2a) has a pronounced "beta-gamma-delta" local magnetic field (Fig. 2b). This is a sign of the presence of instability in the movement of solar plasma through the magnetic filament arches (Fig. 2c) [4]. This instability occurs in the breakage of a plasma thread leading to a flare in the early hours of March 15th between 00:45 UT and 02:00 UT (Fig. 2d). This eruption is accompanied by X-ray radiation class C9. Such was the mechanism of CME's emergence on March 15, 2015.

Prior to the CME on March 15, 2015, solar wind velocity ranges from 302 to 337 km/s measured by SOHO in the Lagrange equilibrium point L1 between Sun and Earth (0.99 AU). On March 17, SOHO is measured a speed from 367 to 692 km/s, and on 18 March the minimum speed is 540 km/s and the maximum is 656 km/s.

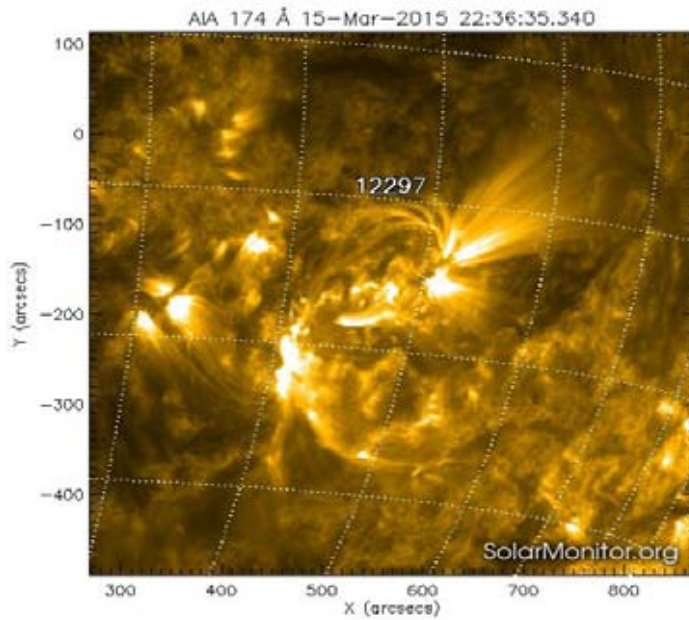


Fig. 2. c) Instabilities in the movement of solar plasma through the magnetic filament arches of Active Region AR2297 (Fig. 2a)

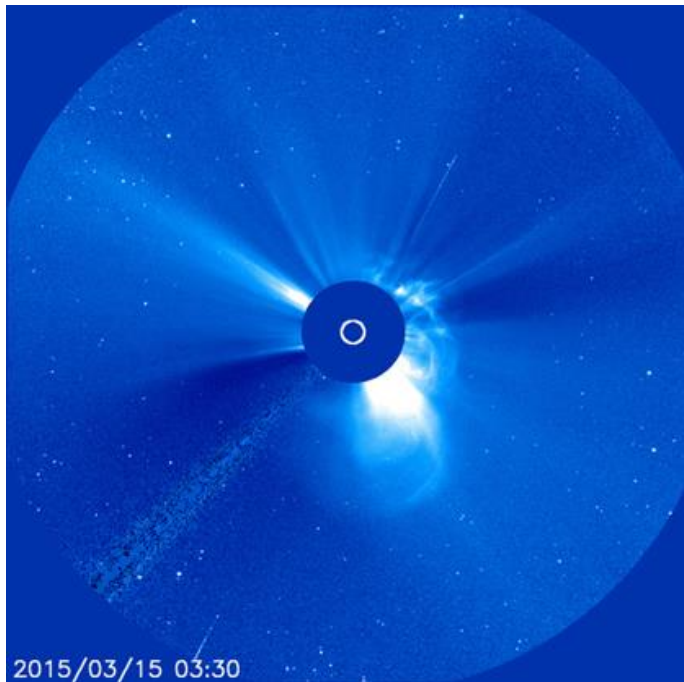


Fig. 2. d) A snapshot of the shock wave triggered by CME is shown on March 15, 2015 at 03:30 UT, taken by SOHO's LASCO C3.

The shock wave reaches the Earth on March 17 at ~18:00 UT, more than two and a half days after the corresponding CME (Fig. 3). In its interplanetary propagation, the shock wave of solar plasma induced by the CME on March 15 is divided into two "clouds".

The right cloud structure struck the Earth's magnetosphere around 18:00 UT and caused a geomagnetic storm. The process of solar plasma development is visualized by the WSA-ENLIL model of Space Weather Forecast Office at NOAA (USA) (Fig.3). This is a large-scale, physically based prognostic model of the heliosphere for prediction solar wind and CMEs from 1 to 4 days.

On Fig. 3 is clearly seen the spiral structure of solar wind in the interplanetary space. At the centre of the circle is the Sun, and the Earth (in green) is located on the right side.

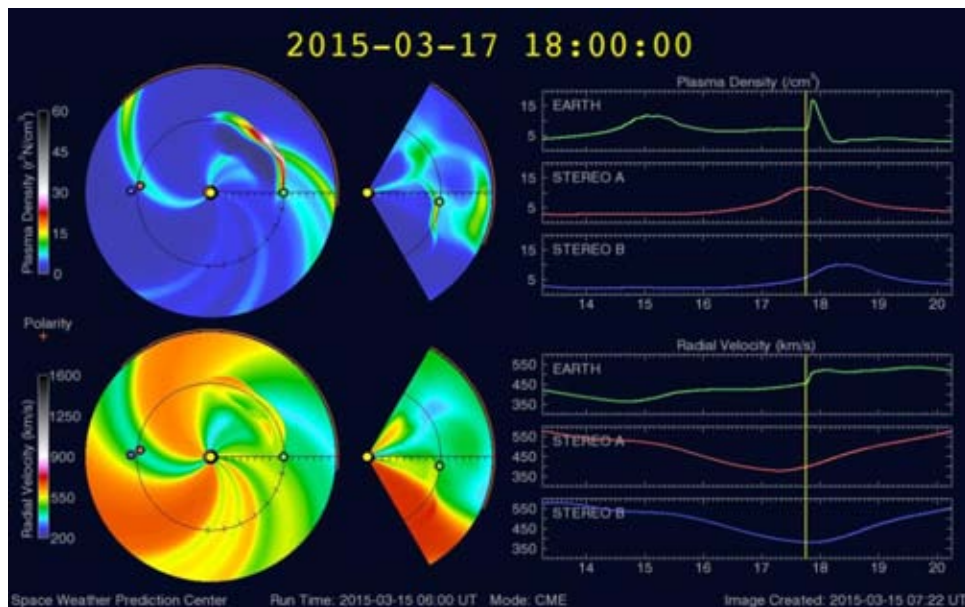


Fig. 3. The process of solar plasma propagation in interplanetary space on March 15, 2015 is visualized by the model WSA-ENLIL of Space Weather Forecast Office, NOAA, USA. At the centre of the circle is the Sun, and the Earth (in green) is on the right side.

The considered CME on March 15, 2015 also creates modulation of the Galactic Cosmic Ray (GCR) flux in the Earth's environment. This is the well-known Forbush effect of the GCRs. The Forbush decrease exceeds -4% and lasts more than 3 days (Fig. 4) [9]. As a result of these processes, a geomagnetic storm lasting three days from 17 to 19 March 2015 with $Dst = 225$ nT occurred [1, 2].

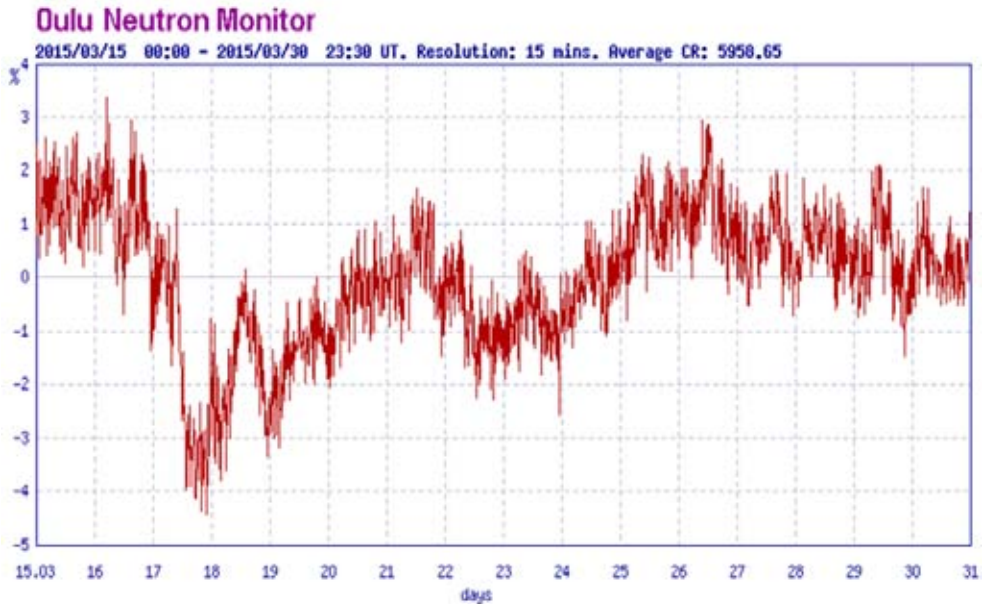


Fig. 4. Results from Oulu Neutron Monitor [10]. Time course (resolution: 15 mins) of the neutron component of cosmic rays during the period March 15–31, 2015. There are seen the Forbush decreases on March 17 (-5%) and March 18 (-3%) which correspond to the geomagnetic storms with $K_p,max = 8$ and $K_p,max = 6$ on these two days.

Coronal mass ejections on September 4, 6 and 10, 2017 in solar minimum

The beginning of the intensive solar-terrestrial disturbances in early September 2017 at minimum of solar cycle 24 was the Active Region AR2673 (Fig. 5a), which produced four powerful eruptions class X, including the strongest flare X9.3 of Solar Cycle 24 on September 6, 2017, after which began G4 – Severe geomagnetic storm on 07–08.09.2017 with $A_p = 96$, and also the second strongest flare X8.2 of Solar Cycle 24 on September 10, 2017, which generated instantly the ground level enhancement of cosmic rays or Ground Level Event № 72 (GLE72). This GLE72 is the second GLE in the current solar cycle (Solar Cycle 24) after GLE71 on 17 May 2012 during the solar maximum [8, 9]. Therefore the new GLE72 in solar minimum represents special interest.

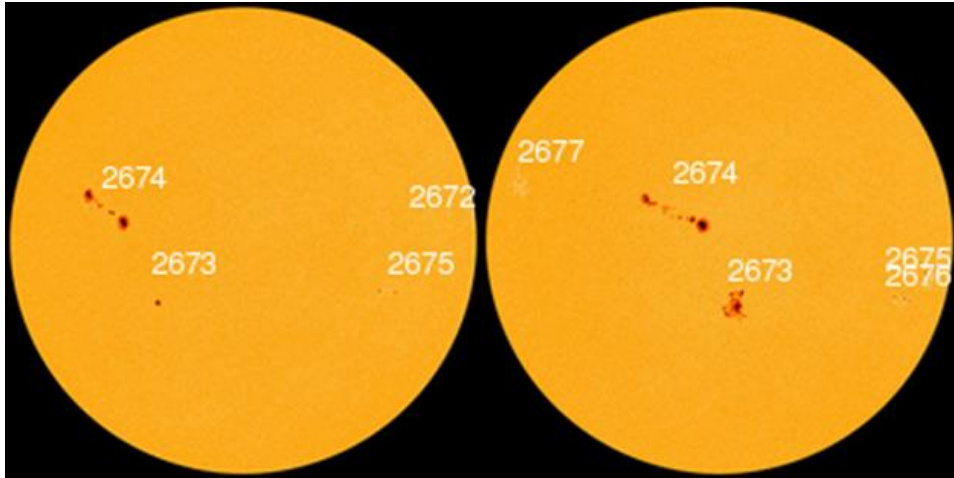


Fig. 5. a) and b): Development of sunspot groups – Active Regions AR2673 and AR2674 for 24 hours – on September 2 and September 3, 2017. It is seen the rapid development of the AR2673 for 24 hours. The active region increases its area four times.

In the investigated period (02–08.09.2017), the two CMEs were observed in sequence over two days. The events began on September 2, 2017. Then there are four active regions in the solar photosphere (Fig. 5a) [1, 8].

Two of the active regions are in the eastern part. The Active Regions AR2673 and AR2674 are to pass through the central meridian and occupy a frontal position with respect to the Earth. The double solar spot 2674 grows relatively rapidly, expanding both in terms of area and number of sunspots. As the number of sunspots increases, the magnetic field becomes more unstable. There is evidence of the development of a combined "beta-gamma" magnetic field, which is a prerequisite for outbreaks in the X-ray bursts of the solar spectrum, at least of class M [1, 2].

On September 3, 2017 it was found that while the AR2674 sunspot group grew for days, the AR2673 group increased its area four fold, and the sunspots in just 24 hours (Fig. 5b).

The fast-growing solar AR2673 has a "beta-gamma-delta" magnetic field that charges energy for M-class solar flares. On September 4, two eruptions have already been detected in the M1 class of X-ray area. On 4 September at 19:00 UT there was a CME directed to the Earth (Fig. 6a, b).

The observed CME spreads frontally to the Earth and reaches terrestrial magnetosphere on 07 September 2017 in the morning hours. On September 6, 2017 at 12:24 UT, there was a second CME, from the same AR2673 targeting the Earth (Fig. 6b).

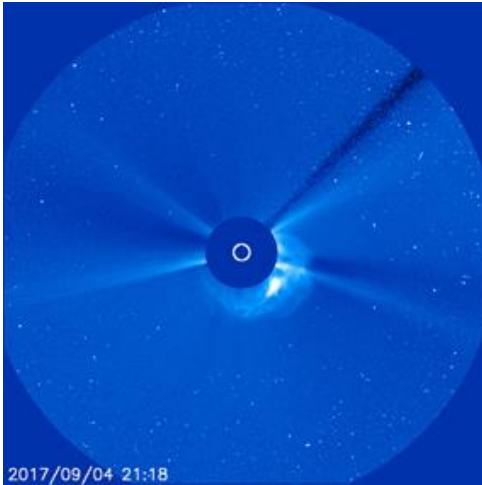


Fig. 6a

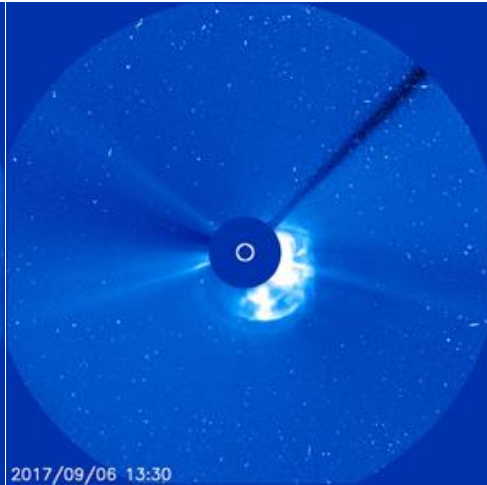


Fig. 6b

Fig. 6. a) The X-ray eruption on September 4, 2017 starting at 21:18 UT and the corresponding coronal mass ejection; b) The X-ray eruption on September 6, 2017 starting at 12:24 UT and the corresponding coronal mass ejection et 13:30 UT.

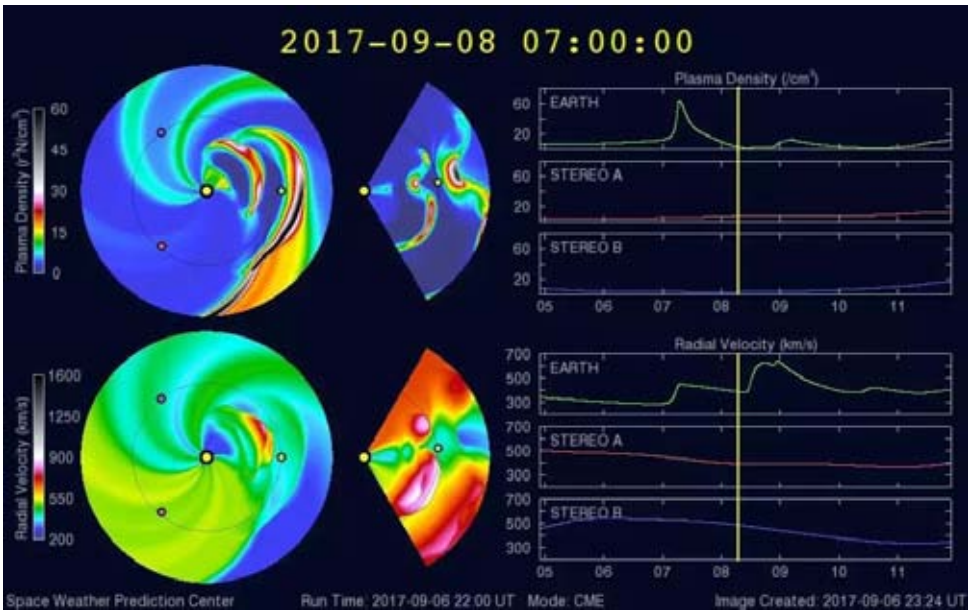


Fig. 7. Visualization by the WSA-ENLIL Solar Wind Prediction model of the first shock wave from CME and the second shock wave from the CME on September 6, 2017 from the sunspot group 2673 spreading towards the Earth.

It is estimated that the shock wave from the second CME will reach Earth's magnetosphere on September 8, 2017 in the afternoon. The situation is modeled by the NOAA (WSA) – ENLIL Solar Wind Prediction model and is shown in (Fig. 7). The photos are from the SOHO platform – LASCO C3.

CMEs on 4 and 6 September 2017 cause a geomagnetic storm, with the Dst geomagnetic index reaching 150 nT. As a result of the two events, there is a deep Forbush decrease in the galactic cosmic ray flux, which in the maximum phase reaches around 15 % in South Pole cusp [1] caused on September 04 and 06, 2017 two Coronal Mass Ejections. The Forbush decrease measured with the neutron monitor in Oulu is -8% (Fig. 8). Compared with the previous event of March 15, 2015, where the decline is -4%, this decrease on 4 and 6 September is doubled.

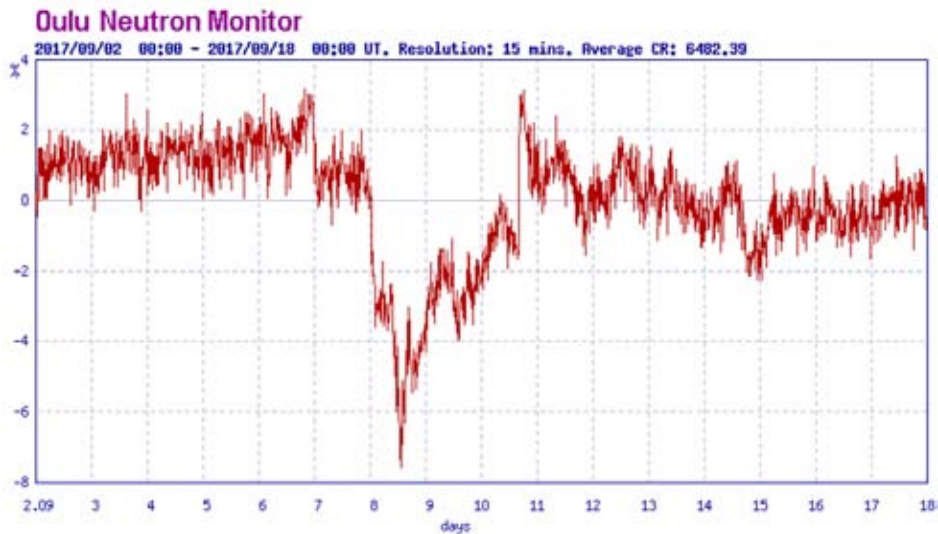


Fig. 8. Results from Oulu Neutron Monitor [10]. Time course (resolution: 15 mins) of the neutron component of cosmic rays during the period September 02–18, 2017. It is seen the two-stage Forbush decrease on September 07–08 (-10%) which corresponds to the geomagnetic storms with $K_p,max = 8$ and $K_p,max = 8$ on these two days.

Going behind the apparent horizon of the solar disk, almost on the edge, the Active Regions AR2673 provoked another, the third very strong CME accompanied by a powerful X-ray eruption class X8.2 at 16:47 UT on 10 September 2017. At the same time, begins a high energy proton emission,

Coronal mass ejections on September 10, 2017

Only four days after September 6, 2017 there was a new CME. Going behind the apparent horizon of the solar disk, almost on the edge, the AR2673 solar

region caused another strong CME accompanied by a powerful X-ray eruption class X8.2 at 16:47 UT on 10.09.2017 (Fig. 9a). At the same time, this event has high energy proton emission (Fig. 9b), accompanied by relativistic solar cosmic rays, i.e. GLE72 [1, 8, 9]. But this is another event that requires separate consideration and analysis.

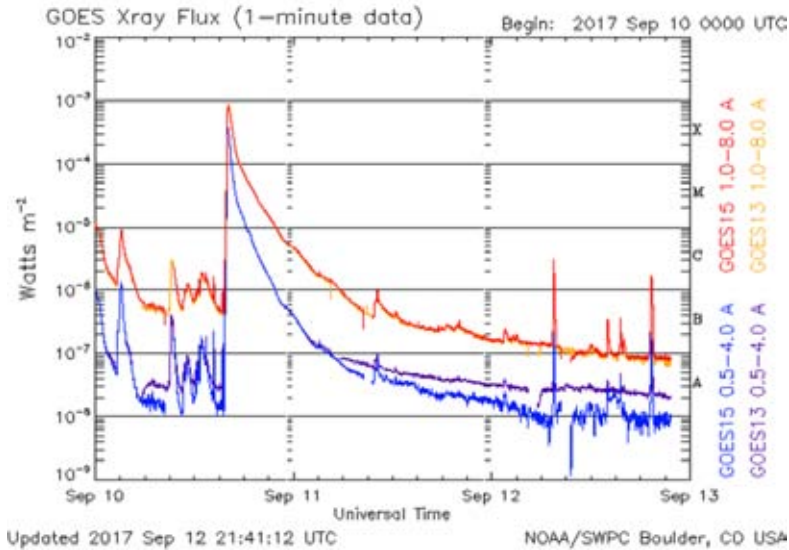


Fig. 9. a) X-ray eruption class X8.2 at 16:47 UT on 10.09.2017

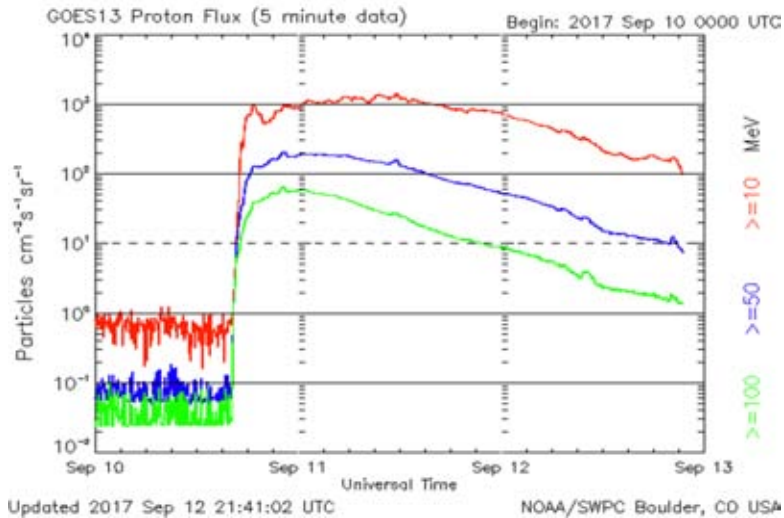


Fig. 9. b) radiation flux of high energy protons ≥ 10 MeV, ≥ 50 MeV and ≥ 100 MeV

Using the NOAA (WSA) – ENLIL model for distribution of solar wind in the interplanetary environment on Fig. 9c is shown the situation in solar system until 2 AU. Fig. 9 reflects the event of 10.09.2017, where it clearly shows the direction of the percussion wave perpendicular to the Sun-Earth axis. In theory, this CME should not affect the Earth, but this is not quite the case. Virtually part of the right flank reaches the Earth. This is because CME has a full halo. Which means the propagation of the shock wave in almost all directions or at 360° .

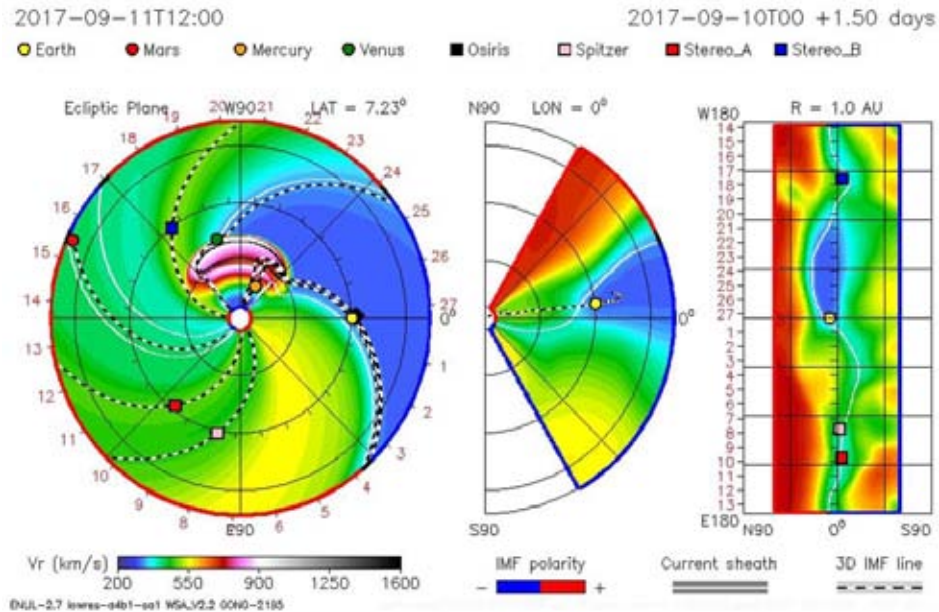


Fig. 9. c) The solar wind in the interplanetary space during the third CME on September 10, 2017

Geophysical efficacy of the two coronal mass ejection periods

The so-called events of the Sun caused significant reactions in the Earth's magnetosphere. G4 Severe Geomagnetic storms, GLE72 as well as Forbush decreases of Galactic Cosmic Rays were observed during the investigated helio-active periods.

The geomagnetic storms on 17–19 March 2015 are the most powerful storms during the current solar cycle. They develop in time period of three days. In the first day, on 17 March 2015, the geomagnetic index Kp reaches the value $Kp = 8$, in the second day $Kp = 6$ and in the third day $Kp = 5$, respectively. The considered geomagnetic storms occur in the decreasing part of the 24th solar cycle (Fig. 10a).

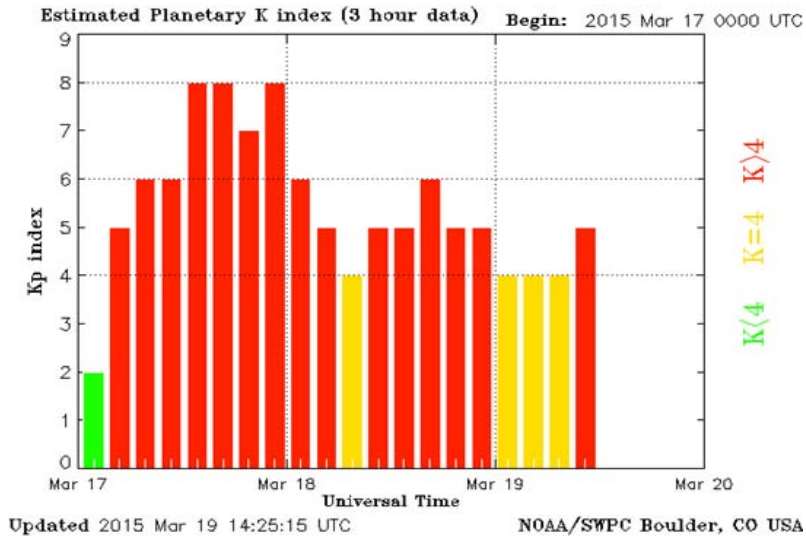


Fig. 10. a) The 3-hour Kp-index during G4 Severe Geomagnetic storms during the period 17–19 March 2015

On March 17, 2015, the largest value of the SSCgeomagnetic Ap-index was 108 nT. This value, and now, almost at the end of the 24th solar cycle, remains the largest measured Ap (Fig.10b).

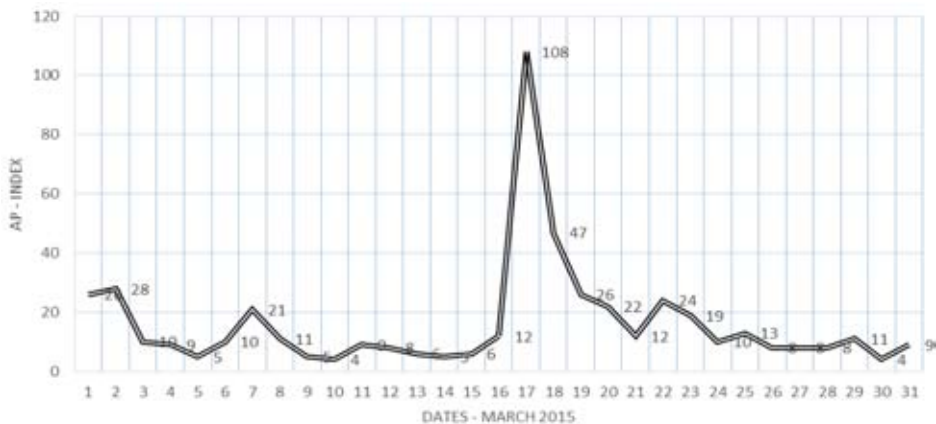


Fig. 10. b) Values of Ap-index for March 2015 according Geo Forschungs Zentrum – Potsdam [9].

In the next active period September 4–10, 2017, the second stronger geomagnetic storm was observed. It begins on September 7 in the evening with a sudden increase of $K_p = 8$. On September 8 it continues with $K_p = 8$, passes through a brief decrease and again $K_p = 8$, after which the geomagnetic storm ceases until the end of the day (Fig. 11a).

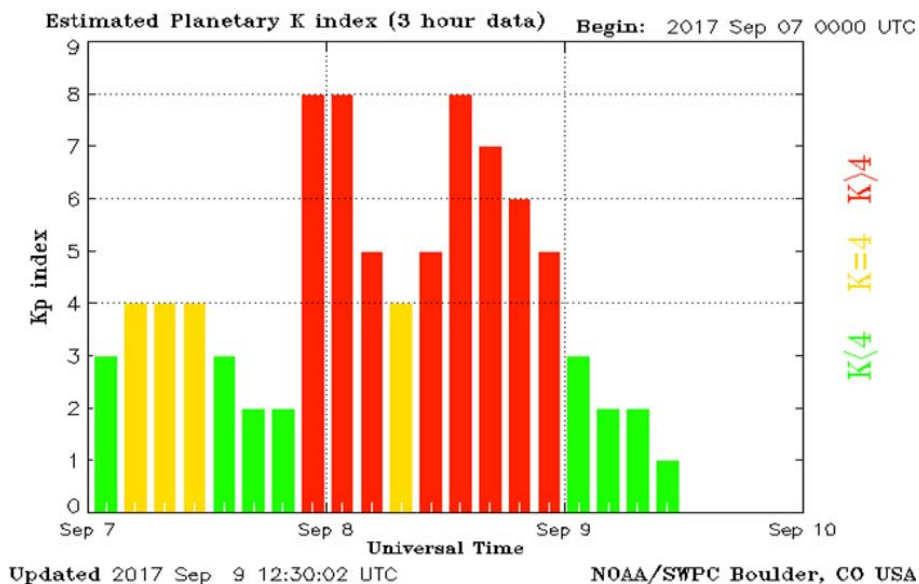


Fig. 11. a) The 3-hour K_p -index during geomagnetic storms on 07–08 September 2017

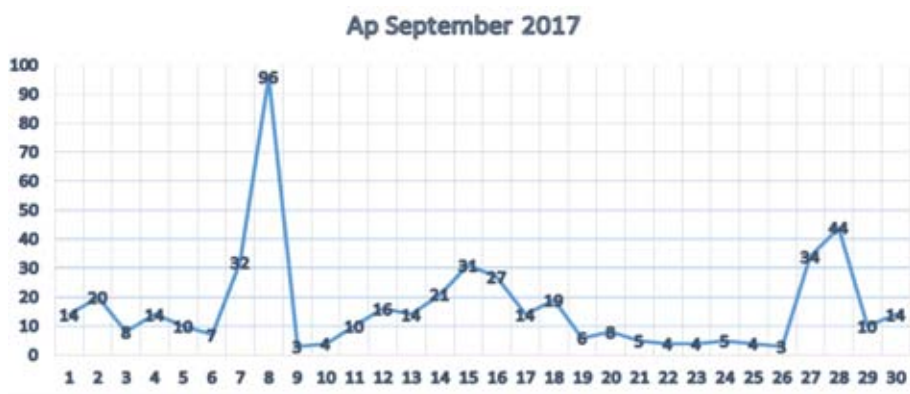


Fig. 11. b) Daily course of A_p -index during September 2017 according Geo Forschungs Zentrum – Potsdam [9]

On September 8, 2017, the second largest value in 24th solar cycle of planetary geomagnetic Ap -index was 96 (Fig. 11b).

Comparison of the state of interplanetary space, solar wind and its basic parameters during GLEs in solar maximum and solar minimum

Solar wind parameters are measured by space probes such as SDO, SOHO, ACE, DSCOVR and WIND, all located at the Lagrange Equilibrium Point L1 between the Sun and the Earth (0.99 AU). Exceptions are the two STEREO A and STEREO B platforms, which are located just opposite to the Earth.

Measurements of the basic parameters of the solar wind are taken for the period March 10–24, 2015 and September 2–15, 2017. These parameters are: the velocity V , density or concentration N and temperature T_p of solar wind and the intensity of Interplanetary Magnetic Field (IMF) B . In this study, measured solar wind parameters from the SOHO, ACE and WIND probes were taken. SOHO data for 2017 show the jump in growth of radial velocity, first on 07.09. and significantly on 08.09.2017. At the same time, the vector of IMF is in south direction. There are all preconditions for the presence of geo-efficiency of these parameters [8].

For quantification of the different energies from the investigated CME events were calculated the following energetic parameters of solar wind [8]:

$$\begin{aligned} \text{the thermal energy } E_t &= 3/2 N k T_p, \\ \text{the magnetic energy } E_m &= \mathbf{B}^2 / 2\mu_0, \\ \text{the dynamic energy } E_k &= 1/2 N V^2, \end{aligned}$$

where k is the constant of Boltzmann, T_p is the temperature of the protons, μ_0 is the magnetic permeability of vacuum.

Using the WIND, ACE and SOHO measured solar wind parameters, we determine the density of the three types of energies: kinetic (dynamic), thermal and magnetic (Table 1). The results of the calculations are shown in Fig. 12. As can be seen from Table 1, SOHO has no magnetic field data, and ACE has many interruptions in measurements. Thus, only the calculation results of the WIND data energy have been shown because they are more representative.

At the beginning on Fig. 12a and Fig. 12b are presented graphically the values of Dst index from the geomagnetic observatory in Kyoto, Japan. The minimum values for the index $Dst = 225$ nT for 2015 and $Dst = 150$ nT for 2017. This indicates that the geomagnetic response is significantly weaker in September 8, 2017 than in March 17, 2015.

Table 1. The maximum values of the kinetic (dynamic) energy density, thermal energy density and magnetic energy density, calculated from measurements of the three space platforms WIND, SOHO, and ACE following the solar events of March 15, 2015 and September 4 and 6, 2017

Energy	Satellite	March 10-24, 2015			September 2-16, 2017		
		Date and Time		Peak Value [J/m ³]	Date and Time		Peak Value [J/m ³]
Kinetic (Dynamic) energy density	WIND	17.3.2015	05:30	7,22E-09	07.9.2017	00:30	3,26E-09
	ACE	17.3.2015	05:00	4,75E-09	07.9.2017	05:00	2,53E-09
	SOHO	17.3.2015	05:00	7,35E-09	07.9.2017	00:00	4,91E-09
Thermal energy density	WIND	17.3.2015	08:30	2,68E-10	07.9.2017	04:30	9,34E-10
	ACE	17.3.2015	06:00	1,05E-10	07.9.2017	05:00	6,78E-11
	SOHO	17.3.2015	06:00	1,06E-10	07.9.2017	00:00	3,23E-11
Magnetic energy density	WIND	17.3.2015	13:30	4,06E-10	08.9.2017	00:30	2,26E-10
	ACE	17.3.2015	13:00	4,39E-10	08.9.2017	13:00	9,31E-11

The same are the thermal energy Fig. 12e – for 2015, and Fig. 12f – for 2017 and finally the magnetic energy – Fig. 12g, for 2015, and Fig. 12h, for 2017.

The comparison shows that the kinetic energy density E_k is higher on 17 March 2015 then E_k from 07 September 2017 on both SOHO and WIND space platforms – Fig. 12c and Fig. 12d.

Compared to the *Dst* index, the development of geomagnetic storms reveals that the maximum density of both kinetic and thermal energies are almost 24 hours before the maximum of *Dst* (Figs. 12a, 12b) of the geomagnetic field characterizing the first geomagnetic storm on September 07, 2017.

It is interesting that the magnetic energy has only one peak, and it is in the late hours of September 07, approximately 12 hours before the second magnetic storm, which is on September 08 around noon. It can be concluded that in both cases, the kinetic energy density and the thermal energy density can be used as an short-term predictor for strong geomagnetic storms.

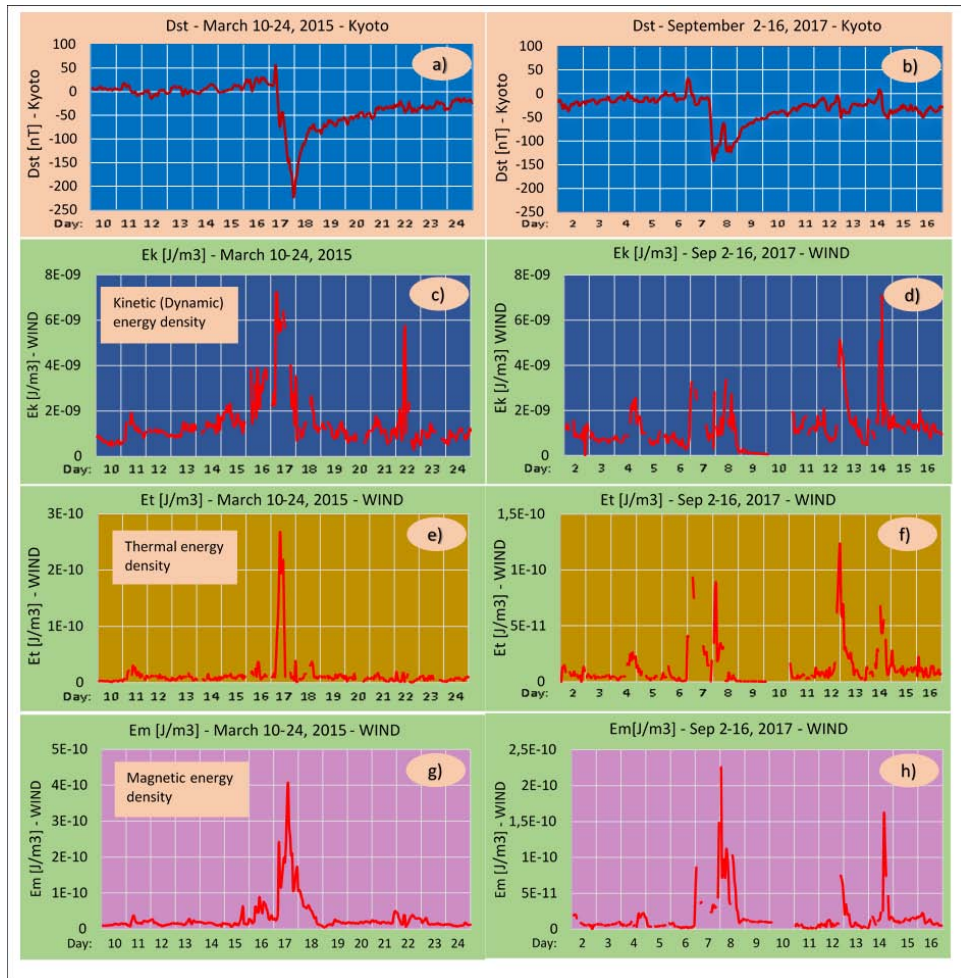


Fig. 12. (a–b) Values of Dst index from the geomagnetic observatory in Kyoto, Japan;
(c–h) Results from calculations of the solar wind parameters from measurements by WIND spacecraft in the point of Lagrange L1 (Table 1):
(c, d) the kinetic (dynamic) energy density E_k ;
(e, f) thermal energy density E_t ;
(g, h) magnetic energy density E_m .

The left side of Figure relates to the investigated period March 10–24, 2015 (a, c, e, g).
The right side relates to the period of September 2–16, 2017 (b, d, f, h)

Accordingly, in Figs. 12c and 12d the dynamic energy for 2015 is greater than that for 2017 years.

The same situation, 24 hours ahead of the peak of kinetic energy density, was also observed for the event of March 15, 2015, comparing Fig. 12a with Fig. 12c. This process has been noticed by us in a previous study [8] and is now confirmed in another CME event. This shows that this is not a random event, but a normal physical process of overtaking by 24 hours the maximum of the kinetic energy density relative to the maximum of the geomagnetic storm.

Table 1 reflects the three maximum energies at peak times after 15 March 2015 and 4 and 6 September 2017. The maximum values were actually reached between 15 and 19 March 2015 and between 04 and 10 September 2017. After 10 September 2017, there is another strong event that is not a subject of this study, because this CME is not targeted toward the Earth. The energies from all three WIND, ACE and SOHO satellites are shown. Highest are the kinetic energy values. Both WIND $E_k = 7.22E-9$ [J/m³] and SOHO $E_k = 7.35E-9$ [J/m³] are approximately the same for kinetic energy at March 15, 2015 event and registered on March 17, 2015.

CME "tunnel" effect around the Earth's environment

In Fig. 7e, the first shock wave from CME from 04.09 and the second CME shock wave from 06.09 spreading towards the Earth is clearly shown. Very interesting is the passing of the two shock waves of CME around the Earth, creating a sort of "tunnel" of lower-speed plasma of solar wind. In other cases, there was a similar "tunneling" of the Earth from a low-speed solar wind, but in this case we have two consecutive coronal mass ejections with the same behavior [8].

Similar behavior of solar plasma is also present at the event of March 15, 2015. By comparing Fig. 3e with Fig. 7e, the following conclusions can be drawn: at the event of March 15, 2015, the separation of solar plasma into two "cloud" is in the plane of the ecliptic. At the event of 04 and 06 September 2017, the division of two "cloud" is perpendicular to the plane of the ecliptic.

At the period of early September 2017 two consecutive CMEs (in one day) are observed. We have seen the spread of the waves around the Earth, creating a specific "tunnel" of the lower-speed solar wind in the plane perpendicular to the plane of the ecliptic.

There are two main reasons for this behavior of solar plasma [4, 8]. One is related to the very source of CME and its magnetic structure. The other with an external source of influence on the interplanetary environment in which solar plasma propagates and the possible influence of the giant planets from the Jovian group, which have strong magnetic fields.

Conclusion

We found some interesting phenomena in the investigated CME periods in different phases of solar activity:

1. When comparing the two CME events of 2015 and 2017, it is found that the kinetic, thermal and magnetic energy densities recorded at Lagrange point L1 (0.99 AU) are proportional to the geomagnetic reaction.
2. The peak of kinetic and thermal energies is 24 hours before reaching the maximum of the geomagnetic storm caused by CME.
3. The observed Forbush decreases in GCR intensity after the occurrence of CME is not proportional to the density of kinetic, thermal and magnetic energies. It is possible with less energy, as in the case of September 7–8, 2017, to have a stronger GCR modulation.

So it is established an inverse relationship between the magnitude of the density of solar wind energies and the effect of Forbush decrease of the galactic cosmic rays.

We are planning calculations of the ionizing profiles of cosmic rays in the atmosphere and estimation the ionization on short and mid time scales [11]. These considerations are of interest for the chemical composition of atmosphere, in particular for its small constituents, which determine the ozone distribution and the temperature regime) [12, 13]. For this purpose are developed both analytical [14, 15] and numerical [16, 17] models.

All these considerations have not only theoretical but also practical significance for solar physics and space weather [18–20].

References

1. Space Weather Prediction Center, National Oceanic and Atmospheric Administration, <http://www.swpc.noaa.gov/>
2. Space Weather, <http://www.spaceweather.com/index.html>
3. Space Weather, <https://www.spaceweatherlive.com/en/news/view/307/20170911-x82-coronal-mass-ejection>
4. Schrijver, C.J., G.L. Siscoe, Heliophysics, Plasma Physics of the Local Cosmos, Cambridge University Press, 2009.
5. Abseim, A.-A., M. Semeida, M. Saleh, S. Youssef, P. Stoeva, and A. Stoev. Modified cloud method validation by determination of physical parameters of the solar flare on June 26, 1999, *Comptes Rendus de l'Acad. Bulg. Sci.*, 2017, 70, 6, pp. 839–848.
6. Richardson, I.G., E.W. Cliver, and H.V. Cane. Sources of geomagnetic storms for solar minimum and maximum conditions during 1972-2000, *Geophys. Res. Lett.*, 2001, 28, 13, 2569–72.
7. Gonzalez, W. D., B. Tsurutani, and A.L. Clúa de Gonzalez. Geomagnetic storms contrasted during solar maximum and near solar minimum, *Adv. Space Res.*, 2002, 30, 10, 2301–04.

8. Tassev, Y., P.I.Y. Velinov, L. Mateev, and D. Tomova. Analysis of extreme solar activity in early September 2017: G4 - Severe geomagnetic storm (07-08.09) and GLE72 (10.09) in solar minimum, *Comptes Rendus de l'Acad. Bulg. Sci.*, 2017, 70, 10, 1437–44.
9. NMDB: Real-Time Database for high-resolution Neutron Monitors. <http://www.nmdb.eu/>
10. Planetarische Kennziffern der geomagnetischen Aktivität. <http://www.gfz-potsdam.de/kp-index>
11. Mishev, A., P.I.Y. Velinov. Ionization effect due to cosmic rays during Bastille Day Event (GLE 59) on short and mid time scales, *Comptes Rendus de l'Acad. Bulg. Sci.*, 2016, 69, 11, 1479–84.
12. Kilifarska, N. An autocatalytic cycle for ozone production in the lower stratosphere initiated by galactic cosmic rays, *Comptes Rendus de l'Acad. Bulg. Sci.*, 2013, 66, 2, pp. 243–252.
13. Kilifarska, N., V. Bakhmutov, G. Melnyk. Energetic Particles Influence on the Southern Hemisphere Ozone Variability, *Comptes Rendus de l'Acad. Bulg. Sci.*, 2013, 66, 11, 1613–22.
14. Velinov, P.I.Y. Formulas for Ionization Yield Functions and Ionization Capability of Solar Cosmic Rays in the Ionosphere and Atmosphere. *Comptes Rendus de l'Acad. Bulg. Sci.*, 2014, 67, 11, 1555–60.
15. Velinov, P.I.Y. Expressions for ionizing capability due to sub-relativistic solar cosmic rays with anisotropic and isotropic penetration in the ionosphere and atmosphere. *C.R. Acad. Bulg. Sci.*, 2015, 68, 1, pp. 79–88.
16. Mishev, A., P.I.Y. Velinov. Ionization rate profiles due to solar and galactic cosmic rays during GLE 59 Bastille day 14 July, 2000. *Comptes Rendus de l'Acad. Bulg. Sci.*, 2015, 68, 3, 359–366.
17. Mishev, A., P.I.Y. Velinov. Determination of medium time scale ionization effects at various altitudes in the stratosphere and troposphere during ground level enhancement due to solar cosmic rays on 13.12.2006 (GLE 70). *Comptes Rendus de l'Acad. Bulg. Sci.*, 2015, 68, 11, 1427–32.
18. Semeida, M., B. Marzouk, P. Stoeva, and A. Stoev (2015) Empirical investigation of solar photosphere and faculae in Ca II IR triplet lines using non-local thermodynamic equilibrium method, *Comptes Rendus de l'Acad. Bulg. Sci.*, 2015, 68, 10, 1287–94.
19. Semeida, M., B. Marzouk, P. Stoeva, and A. Stoev. Physical models for Ca II IR triplet lines in solar photosphere and faculae in non-local thermodynamic equilibrium, *Comptes Rendus de l'Acad. Bulg. Sci.*, 2016, 69, 8, 1047–56.
20. Mateev, L., Y. Tassev, and P.I.Y. Velinov. Application of the idea of morphism in solar-terrestrial physics and space weather, *Comptes Rendus de l'Acad. Bulg. Sci.*, 2016, 69, 12, 1533–42.

СРАВНЕНИЕ МЕЖДУ ИЗВЪНРЕДНАТА СЛЪНЧЕВА АКТИВНОСТ В ПЕРИОДИТЕ 15–17 МАРТ 2015 И 4–10 СЕПТЕМВРИ 2017 В РАЗЛИЧНИ ФАЗИ НА 24-ТИ СЛЪНЧЕВ ЦИКЪЛ

Д. Томова, П. Велинов, Й. Тасев

Резюме

Изследвани са две от най-мощните слънчеви събития с коронално изхвърляне на маса (СМЕ), насочени към Земята, от последния 24-ти слънчев цикъл. Това са СМЕ от 15 март 2015 и СМЕ от 4, 6 и 10 септември 2017. Изчислени са трите основни плътности на енергии: магнитна, термична и динамична енергии, достигащи в точката на Лагранж L1, разположена между Слънцето и Земята. Използвани са данни от космическите станции WIND, ACE, SOHO и DSCOVR, измерващи параметри на слънчевия вятър. От тези параметра: скорост, плътност и температура на потока слънчев вятър, както и интензитета на междупланетното магнитно поле, се изчисляват плътностите на трите енергии - магнитна, термична и динамична. Оценени са плътностите на енергиите, както за отделните събития, така и кумулативната енергия за всяко едно от тях. Количественият анализ показва, че не винаги размера на геомагнитната реакция е съизмерим с плътността на потока енергия, достигащ до магнитосферата. При двете изследвани събития плътностите на енергиите имат различно поведение във времето, но и при двете може да се говори за прогностичен ефект, но с различна степен на нарастване на динамичната и термична енергии. Такъв ефект не се наблюдава в плътността на магнитната енергия. Регистрира се интересно поведение на Форбуш ефектите, т.е. пониженията в потока на галактическите космически лъчи (GCR). В случаите с по-висока плътност на енергията (периода през март 2015) има по-малко процентно понижение на GCR. И обратно при по-ниска плътност на енергията се наблюдава по-голямо понижение на GCR (периода през септември 2017).

HIGH SPEED SOLAR WIND STREAMS OVER THE LAST FOUR SOLAR CYCLES

Yana Asenovska, Simeon Asenovski

*Space Research and Technology Institute – Bulgarian Academy of Sciences
e-mail: asenovski@space.bas.bg*

Abstract

Studying the high speed solar wind streams (HSS) behavior over the course of a solar cycle (SC) can give a valuable knowledge about solar activity. Using the experimental data for the solar wind parameters close to Earth, the variation of the HSS over the last four SC (21÷24) is shown. While the HSS velocity and appearance for the SC 21÷23 have similar distribution – the maximum of both is around declining phase of solar activity cycle; the situation in SC 24 is not well defined. For the last 24 cycle 302 HSS events were isolated and their maximum speed was estimated.

Introduction

According to the flow properties, the near-Earth's solar wind generally is treated as a three component system: high speed streams (HSS), slow solar wind and streams associated with coronal mass ejections (CME) [1]. The frequency of occurrence and intensity of these three components depends strongly on the phase of the solar activity cycle, as large scale Sun's magnetic field modulates the expansion of the solar wind [2]. HSS are characterized with high speed (> 500 km/s), high proton temperature and low plasma density. They originate from coronal holes, which are unipolar open magnetic field areas [3–5]. HSS and CME are the main types of solar generated drivers that affect Earth. The strong sporadic storms during maximum are caused by CMEs [5, 6], and especially by magnetic clouds with strong and smoothly rotating magnetic field inside the structure providing prolonged periods of southward B_z [7].

Coronal holes are the largest and the most geoeffective during the sunspot declining phase [8], when a second maximum in the geomagnetic activity is observed (the first maximum is caused by CME).

High speed solar wind streams for solar cycles 21÷23

The periods of HSS for solar cycles 21÷23 are determined by several catalogues: [9–11]. In Fig. 1 and Fig. 2 averaged values of the maximum speed of

the HSS (red line), duration of the HSS (blue line) and sunspot number (black line) are presented.

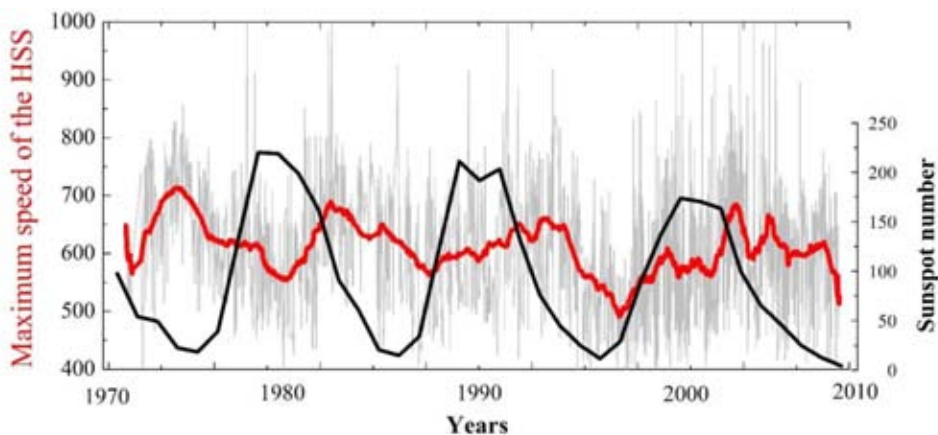


Fig. 1. Maximum speed of the HSS for solar cycles 21÷23

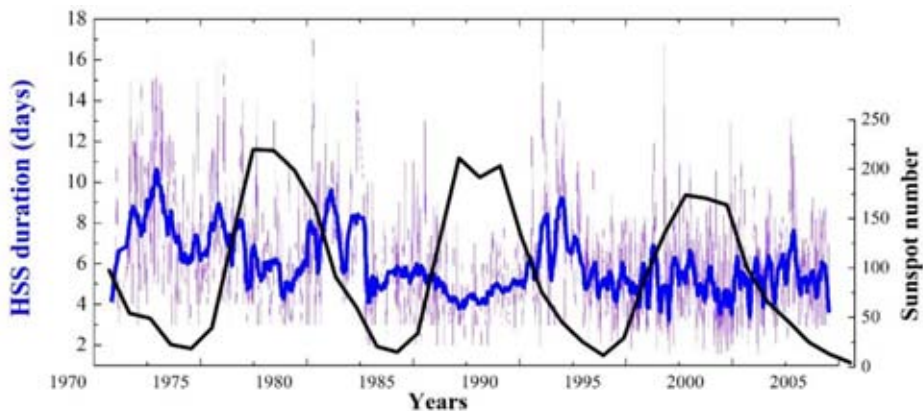


Fig. 2. Duration of the HSS for solar cycles 21÷23

High speed solar wind streams for 24 solar cycle

In order to characterize the HSS, we have used the hourly values of the plasma parameters gathered in OMNI data base (<http://omniweb.gsfc.nasa.gov/>) and the identifying criteria for a HSS which include an increase of the solar wind velocity by at least 100 km/s in no more than one day to at least 450 km/s for at least five hours along with high proton temperature and low plasma density.

For the last 24 cycles we have isolated 302 HSS events and estimated their maximum speed.

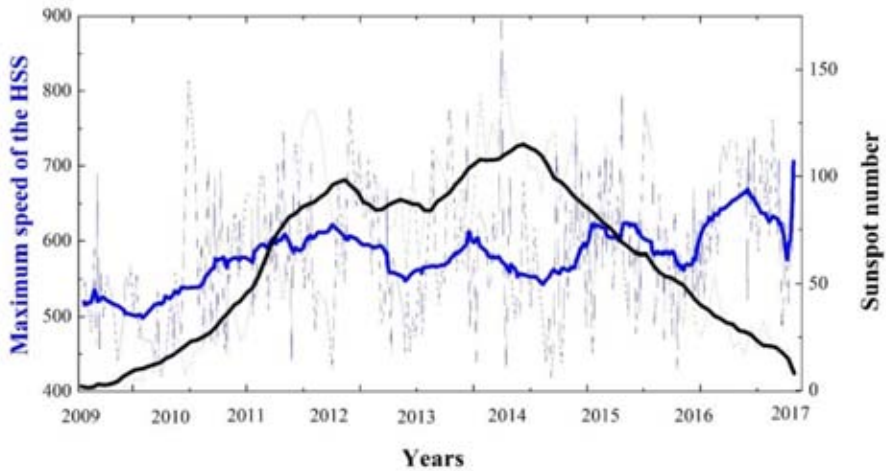


Fig. 3. Maximum speed of the HSS for 24 solar cycle

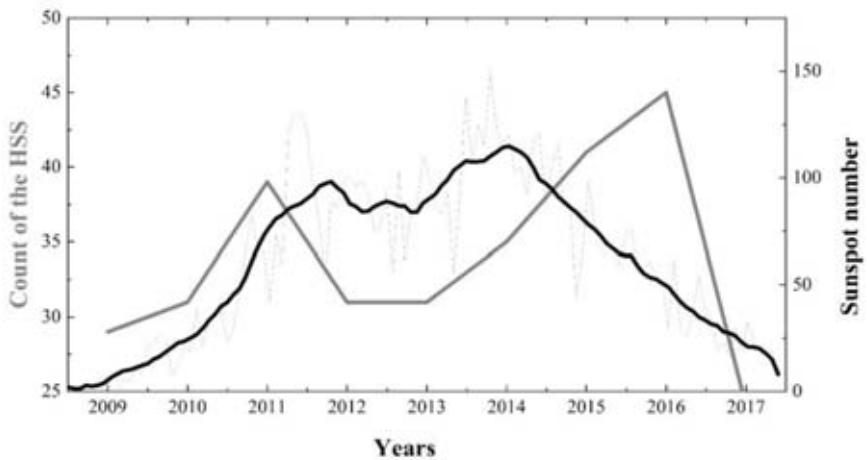


Fig. 4. Count of the HSS for 24 solar cycle

Conclusion

The results of the presented work can be summarized as:

- During the descending phase of the solar cycles 21÷23 the highest values of maximum HSS speed is observed.

- The duration of the HSS is the longest (8÷10 days) during the descending phase of the solar cycles 21÷23.
- 302 HSS events have been isolated for the last 24th solar cycle and their maximum speed was estimated.
- The profile of the maximum speed of HSS within the 24th solar cycle is different compared to the previous solar cycles and no maximum value is observed.
- The count of the HSS is the greatest during the descending phase of 24th solar cycle.

Acknowledgments

This work was supported by the National Science Fund under Competition for financial support for projects of junior researchers – 2016, grant № DM 04/4 from 14.12.2016 “Investigation of the impulsive solar activity agents throughout the 11-year solar cycle”.

References

1. Richardson, I.G., H.V. Cane, Solar wind drivers of geomagnetic storms during more than four solar cycles, *J. Space Weather Space Clim.*, 2012, A01, DOI: 10.1051/swsc/2012001.
2. Pneuman, G.W., R.A. Kopp, Gas-Magnetic Field Interactions in the Solar Corona, *Solar Physics*, 1971, Vol18, 2, 258–270. DOI: 10.1007/BF00145940.
3. Krieger, A.S., A.F. Timothy, and E.C. Roelof, A coronal hole and its identification as the source of a high velocity solar wind stream, *Sol. Phys.*, 1973, 29, 2, pp. 505–525.
4. Sheeley, Jr. N.R., J.W. Harvey, and W.C. Feldman, Coronal holes, solar wind streams, and recurrent geomagnetic disturbances: 1973-1976, *Sol. Phys.*, 1996, 49, pp. 271–278.
5. Tsurutani, B.T., W.D. Gonzalez, F. Tang, and Y.T. Lee, Great magnetic storms, *Geophysical Research Letters*, 1992, 19, 1, pp. 73–76.
6. Echer, E., W.D. Gonzalez, B.T. Tsurutani, and A.L.C. Gonzalez, Interplanetary conditions causing intense geomagnetic storms (Dst = –100 nT) during solar cycle 23 (19962006), *J. Geophys. Res.*, 2008, 113, A05221, DOI: 10.1029/2007JA012744.
7. Georgieva, K., B. Kirov, and E. Gavrusseva, Geoeffectiveness of deferent solar drivers, and long-term variations of the correlation between sunspot and geomagnetic activity, *Physics and Chemistry of the Earth*, 2006, 31, pp. 1–3, 81.
8. Phillips, J., S.J. Bame, W.C. Feldman, J.T. Gosling, C.M. Hammond, D.J. McComas, B.E. Goldstein, M. Neugebauer, E.E. Scime, and S.T. Suess, Ulysses Solar Wind Plasma Observations at High Southerly Latitudes, *Science*, 1995, 268, 1030–33.
9. Lindblad, B., A. Lundstedt, H. A catalogue of high-speed plasma streams in the solar wind, *Solar physics*, 1981, 74, pp. 197–206.
10. Mavromichalaki, H., Vassilaki, A., Fast plasma streams recorded near the Earth during 1985-1996, *Solar physics*, 1998, 183, pp. 181–200.

11. Xystouris, G., E. Sigala, and H. Mavromichalaki. A complete catalogue of high-speed solar wind streams during solar cycle 23. *Solar Physics*, 2014, 289, 3, pp. 995–1012.

ВИСОКОСКОРОСТНИ ПОТОЦИ БЪРЗ СЛЪНЧЕВ ВЯТЪР ПРЕЗ ПОСЛЕДНИТЕ ЧЕТИРИ СЛЪНЧЕВИ ЦИКЪЛА

Я. Асеновска, С. Асеновски

Резюме

Изучаването на поведението на високоскоростните потоци бърз слънчев вятър (БСВ) може да даде ценни сведения за слънчевата активност. Използвайки експериментални данни за параметрите на слънчевия вятър близо до Земята, тази работа показва вариациите на БСВ през последните четири слънчеви цикъла (21÷24). Докато появяването и скоростта на БСВ имат сходно разпределение за слънчевите цикли 21÷23 – максимални стойности и на двете периода на спадане на слънчевата активност, то подобно поведение по време на 24 слънчев цикъл не се наблюдава. За последния 24 цикъл са определени 302 БСВ събития и са изчислени техните максимални скорости.

SATELLITE SENSORS USED IN THERMAL REMOTE SENSING

Ivan Yanev

ESRI Bulgaria Ltd.

e-mail: ivan.yanevmail@gmail.com

Abstract

The presented article makes an overview of the most used contemporary satellite remote sensing missions operating in the thermal range of the electromagnetic spectrum. Discussed are the main environmental applications of satellite missions such as Landsat, ASTER, MODIS, CBERS and HJ-1B. Some issues and future perspectives are outlined in conclusion.

Introduction

With the advent of the first satellites equipped with equipment operating in the thermal range in the early 1970s, the Earth's surface temperature has been also studied by remote sensing. Urban climate and environmental studies would be rather difficult, if not impossible, without the ability of satellite sensors to capture images in the thermal range [1]. Today there is a wide variety of sensors that record such data. They range from low spatial resolution (several tens km to 1 km) with acquisition capability every day or even several hours (MODIS, AVHRR) to medium spatial resolution (~60÷90 m) and only 1–2 times a month Landsat ETM+, ASTER, see Table 1. Depending on the spatial coverage, some sensors are more suitable for mapping of large areas, while others provide monitoring of small regions. Temporal resolution determines for what time period the temperature model can be explored – daily, weekly, monthly, or yearly.

The presence of multiple instruments, recording data in the thermal part of the electromagnetic spectrum, also requires a good knowledge to choose the most appropriate or combination of sensors for the purpose of the particular study. Depending on the purpose of the study, the characteristics of the sensors used – spatial resolution, the opportunity to revisit the territory or the temporal resolution, the radiometric resolution that determines the number of brightness levels in the image, the number of spectral bands, as in the thermal range, as well as in the whole electromagnetic spectrum.

Table 1. Sensors in the thermal range of the electromagnetic spectrum [2–4, with changes]

Sensor	Platform	TIR SR (km)	Temporal res. (days)	Swath width (km)	Spectral range (μm)	Agency	Start Year
SR	ITOS-1	7.4				NASA	1970
VHRR	NOAA-3, -5	1.0			~6.00÷~15.0	NOAA	
HCMM	HCMR	0.6	16	715	10.50÷12.5	NASA	1978
AVHRR	NOAA-6, -7	1.1			10.30÷12.5	NOAA	
ETM+	Landsat 7	0.06	16	185	10.40÷12.5	USGS, NASA	1999
TM	Landsat 5	0.12	16	185	10.40÷12.5	USGS, NASA	1984
TIRS	Landsat 8	0.1	17	186	10.90÷12.0	USGS, NASA	2013
ASTER	TERRA	0.09	4–16	60	8.125÷11.6	NASA	1999
IRMSS	CBERS-1, -2, -2b	0.16	26	120	10.40÷12.5	CRESDA INPE	1999/2003, 2003, 2007/2010
IRSCAM	CBERS-3 and -4, 4b	0.08	26	120	10.40÷12.5	CRESDAI NPE	2012, 2014, 2016
MERSI	FY-3A, FY-3B	0.25	1	2 800	11.25	NRSCC, CAST, NSM a.o.	2008, 2010
InfraredCam	HJ-1B	0.3	31	720	10.50÷12.5	CRESDA CAST, NRSCC	2008
NIRST	Aquarius	0.35 1	<1–2	182–1 060	10.70÷11.7	NASA, CONAE	2011
BIRD	BIRD	0.37	10	190	8.50÷9.30	DLR	2001/2004
TET-1	TET-1	0.35 6	10	180	8.50÷9.30	DLR	2012
VIIRS	Suomi NPP	1.6	<1	3 000	8.40÷12.49	NASA/NOAA	2011
CrIS	Suomi NPP	14	<1	2 200	9.14÷15.38	NASA/NOAA	2011
CERES	Suomi NPP	20	<1	3 000	8.00÷12.00	NASA/NOAA	2011
IIR	CALIPSO	1	16	64	8.65÷12.05	CNES	2006
MODIS	TERRA, AQUA	1	4 per day	2 330	10.78÷12.27	NASA	1999, 2002

Sensor	Platform	TIR SR (km)	Temporal res. (days)	Swath width (km)	Spectral range (μm)	Agency	Start Year
ATSR-2	ERS-2	1	3	512	10.80÷12.00	ESA, UKSA, CSIRO	1995/2011
AATSR	Envisat	1	35	500	10.80÷12.00	ESA, UKSA	2002/2012
AVHRR/1	TIROS-N, NOAA 6, 8, 10	1.1	<1	2 600	10.50÷11.50	NOAA	1978/1986
AVHRR/2	NOAA 9, 10, 11, 12, 13, 14	1.1	<1	3 000	10.30÷11.30	NOAA	1984/2005
AVHRR/3	NOAA 15-19, Metop A, B	1.1	<1	3 000	10.30÷12.5	NOAA, EUMET-SAT	1998, 2000, 2002, 2005, 2006, 2012
MSG-SEVIRI	Meteosat-8/9/19	1-3	<1	Full disk	9.38÷14.40	ESA, EUMET-SAT	2002, 2005, 2012
MVIRI	Meteosat-3/4/5/6/7	3	30 min	Full disk	10.50÷12.5	EUMET-SAT, ESA	1988, 1989, 1991, 1993, 1997
MSU-MR	Meteor 3 M, and -M N1	1	37	3 000	10.50÷12.5	ROS-HYDRO-MET a.o.	2001, 2009
MSU-GS	Elektro-L N1	4	geost. <1	Full disk	9.20÷12.05	ROSHY-DROM-ET a.o.	2011
IMAGER	MTSAT-1, 2, 3	4	geost. <1	Full disk	10.30÷12.5	JMA	1999, 2006, 2013
MVISR	FY-1C, 1D	1.1	3-4	3 200	10.50÷12.5	CMA, NRSCC	1999, 2002
IVISSR	FY-2C, 2D, 2E, 2F	5	1	Full disk	10.30÷12.5	NRSCC, CAST, NSMC	2004, 2006, 2008, 2012
VHRR	Insat-2A, E, -3A	8	30 min	Full disk	10.50÷12.5	ISRO	1992, 1993, 1999, 2003

Sensor	Platform	TIR SR (km)	Temporal res. (days)	Swath width (km)	Spectral range (μm)	Agency	Start Year
IASI	MetOP-A/B	25	29	2 052	8.26÷15.50	CNES, EUMETSAT	2006, 2012
HIRS/3	NOAA-15, -16, -17	20.3	<1	2 240	11.11	NOAA	1998, 2000, 2002
HIRS/4	NOAA 18/19, MetOP A/B	20.3	<1	2 240	6.70÷15.00	NOAA, EUMETSAT	2005, 2006, 2009, 2012
ScaRaB	Meteor-3, Resurs-01, Megha Tropiques	40	1	2 200	10.50÷12.5	CNES	1994, 1998, 2011
GOES imager	GOES	4	3 hours	Full disk	10.20÷12.5		1974

The most commonly used surface temperature sensors are presented in the following Table 2.

Table 2. The most commonly used satellite sensors for LST extraction [4]

Sensor	SR	TR	Satellite	Agency
MSG-SEVIRI	1-3 km	<1 d	Meteosat-8, 9, 19	ESA/EUMETSAT
AVHRR	1.1 km	< d	NOAA	NOAA, EUMETSAT
MODIS	1 km	4 per day	TERRA, AQUA	NASA
AATSR	1 km	35 d	Envisat	ESA, UKSA
InfraredCam	300 m	31 d	HJ-1B	CRESDA, CAST, NRSCC
MERSI	250 m	1 d	FengYun	NRSCC, CAST, NSM,
MVISR	1.1 km	3-4 d		CMA
IVISSR	5 km	1 d		
IRMSS	160 m	26 d	CBERS-2	CRESDA, INPE
TM	120 m	16 d	Landsat 5	USGS, NASA
ETM+	60 m	16 d	Landsat-7	USGS, NASA
ASTER	90 m	16 d	Terra	NASA

According to the Scopus indexed documents, the sensors with the highest spatial resolution are the most commonly used. Therefore, leaders in this regard are sensors aboard Landsat, followed by ASTER and MODIS. Of course, this is highly dependent on the scale of the study. For example, for large-scale studies, the lower spatial resolution is not an obstacle, so the most used sensors in this case are MODIS and NOAA AVHRR. Fig. 1 presents the thermal sensors most commonly used in the articles in Scopus.

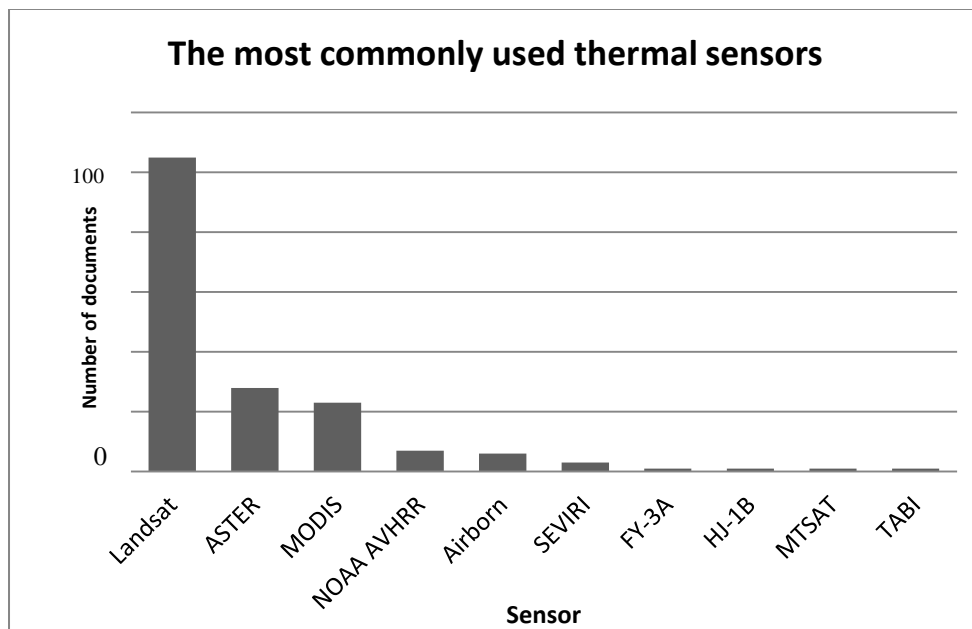


Fig. 1. The most commonly used thermal sensors according to Scopus

Despite the relatively weaker interest in thermal satellite data studies (compared to the visible range of the electromagnetic spectrum, for example), applications in this area are quite wide – agriculture, climatology, hydrology, analysis of urban thermal islands and thermal pits, monitoring of volcanoes, geothermal analysis, forest fires and exposure of burned areas, observation of industrial zones, extraction of soil moisture data etc. In addition, thermal data is used not only for land applications but also on the water surface of the Earth by extracting Sea Surface Temperature (SST). It is quite natural for different applications that there are different sensing requirements for the remote sensors. Since the urban environment is quite heterogeneous, high spatial resolution (SR) sensors are needed for its study. Unfortunately, despite the wide variety of thermal sensors, there are several limiting factors in the choice of images: 1). There is a

lack of high SR sensors in the thermal range. The highest SR at the moment is 60 m from Landsat 7 ETM+. This necessitates the use of algorithms for artificially improving the SR; The higher the SR, the lower the temporal resolution and vice versa. This appears to be a limiting factor in exploring the dynamics of temperature on a large scale, particularly in cities; due to the high and densely built-up urban areas, images captured in a central projection are required. Below is a description of some of the most frequently used remote sensing sensors – ETM+, ASTER, CBERS, HJ-1B, and MODIS.

Landsat

Landsat 7 ETM+ has for many years been, in a scientific jargon, the "work horse" for thermal remote sensing. The Landsat ETM+ sensor has one thermal band in the range 10.4÷12.5 μm delivering data with 60 m SR [5]. Each band records data either in low- or high-gain mode, depending on the Sun's angle and the type of land cover specified in the Long Term Acquisition Plan (LTAP) – land/land, desert, ice/snow, water, sea ice, and volcano. These types of land cover are pre-mapped. Only band 6 of Landsat 7 is always available in low- and high-gain mode, which extends the range of registered temperature values. However, detect illumination may occur if the surface has an extremely high temperature, and vice versa, the surface will not be captured if its temperature is below a certain threshold. The minimum and maximum temperatures in the low-gain mode range from – 34 to 51 $^{\circ}\text{C}$ and high-gain respectively – 134 to 77 $^{\circ}\text{C}$. These are the temperature values that can be captured within one pixel in Band 6. Band 5 (middle infrared), with a wavelength of 1.55÷1.75 μm , can be used to detect thermal anomalies with temperature values of 200÷450 $^{\circ}\text{C}$, which lead to saturation of Band 6. Even Band 4 (NIR) offers the possibility of exploring extremely high temperatures – 600÷1 000 $^{\circ}\text{C}$. Although low- and high-gain options are new compared to the previous Landsat TM, the thermal band of ETM+ is less suitable for high temperature testing. Its maximum is 51 and 77 $^{\circ}\text{C}$, while on Band 6 of the TM sensor this value is about 90 $^{\circ}\text{C}$. As a disadvantage of ETM+, an obsolete 8 bit dynamic range (radiometric resolution) can be seen as a limiting factor for the brightness levels to 256 instead of 4 096, for example if a 12 bit system is used. The main difference between Landsat TM and ETM+ is SR – 120 m (at 60 m for ETM+), lack of double gain as well as absence of panchromatic channel in the visible range and weaker radiometric sensitivity. At special order it is possible to capture at night (only in the thermal channel). However, the number of the night data is limited, as more energy (downstream orbit) is consumed to capture. The capture of one scene leads to skipping seven day scenes when the orbit is ascending. The data from the ETM+ have been available since 1999. However, in May 2003 a failure occurred in one of the scanning mirrors. According to official data, 78 % of data are unaffected. Since February 2013, the latest Landsat Data

Continuity Mission (LDCM) sensor has been in orbit, which also has a thermal sensor, but unfortunately its SR is only 100 m. The LDCM specifications are comparable to those of the previous sensors – SR, swath width, radiometric and geometric accuracy, range of bands. Both the Operational Land Imager (OLI), VIS, NIR and SWIR and TIRS (thermal infrared sensor), are pushbroom sensors, while the previous Landsat sensors are whiskbroom type. The technological improvements of the new heat sensor include pushbroom mode, two spectral bands, TIRS optics are cooled to reduce side noise, better signal-to-noise ratio (SNR), and 12-bit data allow for more accurate temperature measurements with a range of – 330 to 870 °C – a slightly higher range than previous sensors. An important advantage of TIRS is the presence of two spectral bands with a central wavelength of 10.9 and 12 µm. This allows the thermal influence of the atmosphere to be compensated for transforming the sensors recorded at the surface temperature. In order to do this with the ETM+ thermal band, additional atmospheric status data should be used.

ASTER

Since December 1999, ASTER has been orbiting in a polar, solar-synchronous orbit (30 minutes behind Landsat 7), and data began to receive at the end of February 2000 with a 16-day revisiting period [6]. The registered images cover an area of 60 km × 60 km and are captured around 10:30 AM local time. Unlike Landsat 7, which records data permanently and thus provides coverage almost all over the world (excluding poles), ASTER scans the Earth's surface only at the request of users and therefore does not guarantee coverage of a given territory. Night images with 5 thermal bands, taken around 10:30 local time, can also be tasked. A great advantage of the thermal night data is that at that time the Sun's influence on the heat signal is almost completely eliminated. The impact of unequal heating due to tilt and exposure is minimized. The great advantage and unique feature of ASTER is the presence of 5 spectral bands in the thermal range between 8.125 and 11.65 µm, the 90 m SR and the 12 bits dynamic range. For MODIS, there are two channels in the thermal range, and the 1 km SR. ASTER therefore provides a spectrum of surface emissivity based on 5 measurements, as the transmitting power varies with the wavelength.

MODIS

The MODIS sensor records data in 36 spectral channels in the range between 0.62 and 14.385 µm [7, 8]. The spatial resolution is 250 m for VIS bands 1 and 2, 500 m for bands 3–7 (VIS – NIR) and 1000 m for other channels from 8 to 36 (visible, near infrared (NIR), medium IR (MIR) and thermal (TIR) infrared, at the maximum shooting angle of 55° pixels at the margins of the image can be between 2 and 5 km, however, the wide range of the sensor ensures a high shooting

frequency so that the data of MODIS are available daily for the vast majority of the earth's surface. MODIS is on board of two satellite platforms – Terra (1999) and Aqua (2002), which allows most areas to be captured 4–5 times per day, including nighttime imaging, allowing for the accumulation of long time series without cloud coverage, for thermal exploration using bands 20–23 with a spectral range of 3.66–4.08 μm) and most of all bands 31 and 32 (10.78–12.27 μm).

Chine-Brazil Earth Resource Satellite (CBERS)

CBERS-1 has been operating from 1999 to 2003 when the CBERS-2 is being delivered in orbit and it is delivering data to this day [9]. Infrared Multi-Spectral Scanner (IRMSS) is one of the three satellite instruments that has a thermal band (10.4–12.5 μm) with 156 m SR [10]. CBERS-2b has been running for 3 years starting in 2007. The CBERS-3, originally planned for 2010, then autumn 2012, is still launched in December 2013. However, a problem with the carrier rocket has led to the loss of the satellite, which carries an improved infrared scanner that delivers thermal data (10.4–12.5 μm) with 80 m SR and a swath width of 120 km. Depth of acquisition is 8 m. The panchromatic band has a SR of 5 m and the multispectral 10 m and a swath width of 60 km. CBERS-4 is on a sun-synchronous orbit from the end of 2014, although planned for 2015, replacing the failed mission of CBERS-3. The CBERS-4b are in the production phase and are not yet in orbit, although it is planned for 2016.

HJ-1B

HJ-1B is the second of the three HJ satellites (HuanJing, “environment” in Chinese) [10]. HJ-1A and HJ-1B were removed in September 2006, and in November 2012 HJ-1C. The three satellites are mainly used for natural disasters and environmental monitoring. They provide multispectral and radar images. The HJ-1A, which has 2 thermal bands with 1.1 km SR, is no longer operating. The HJ-1B features an infrared camera that outputs data in the thermal range between 10.5–12.5 μm at 300 m SR and 720 km swath. A MIR channel between 3.5–3.9 μm collects data with 150 m SR and allows detection of extreme temperature anomalies. Thermal data from HJ-1B is mainly used for more generalized LST studies.

Issues and Perspectives

A major issue of thermal satellite data is the low SR. The SR of the thermal images by the currently operating satellites is not high enough, especially when exploring an urban environment where the Earth's surface is extremely heterogeneous. The lack of proper SR leads to the need to use different algorithms for its "artificial" improvement (downscaling) [11–14].

Temporal resolution (TR) is another problem, especially when it comes to exploring dynamic processes. It is, for example, difficult to investigate 24-hour LST changes in cities. High SR heat tools perform no more than 2 observations per month. The basic pattern in thermal imaging is the inverse proportionality between SR and TR – the higher the SR, the lower the TR and vice versa.

Another factor to be taken into account is the urban scattering surface and the instantaneous field of view (IFOV) of the sensor. To extract LST in an urban environment, a tool is needed that "sees" the Earth's surface in a central projection. This is another limiting factor in selecting images for a particular territory.

Speaking of SR and TR of thermal data, the user community needs a high-speed satellite and a roughly daily revisit [15]. There are currently several projects that are trying to meet the user's expectations. One of them, MISTIGRI (MicroSatellite for Thermal Infrared Ground Surface Imaging), is a joint project between the French Space Agency (CNES) and the University of Valencia, Spain. Currently, the project is completed in phase A. TIREX (Thermal Infrared Explorer) is a proposal submitted in 2010 to an announcement of opportunity by the European Space Agency (ESA) on Earth Explorer Opportunity Missions. In the end, the proposal was rejected for phase A. Both missions should have about 50 m SR and a re-visiting time of 1 or 2 days. The HypsIRI (Hyperspectral Infrared Imager) project developed by NASA is expected to capture thermal data with 60 m SR and 5 days of re-visit. The mission is currently under study.

In conclusion, further research is needed in the other areas of LST applications. Thermal IRs has already a number of applications, but research focuses on a narrower range of topics. These data provide a good opportunity to combine thermal analysis of buildings, energy losses from buildings, calculation of cooling/heating degree day indices, with the capabilities of the latest 3D modeling products. Another niche for extensive studies is the dynamic processes in urban micro-climate and, in particular, the dynamics of the Earth's surface temperature (LST).

References

1. Weng, Q. Thermal infrared remote sensing for urban climate and environmental studies: Methods, applications, and trends, *ISPRS Journal of Photogrammetry and Remote Sensing*, 2009, 64, 4, 335–344. DOI: 10.1016/j.isprsjprs.2009.03.007
2. Voogt, J.A. Thermal remote sensing of urban surface, 1995, The University of British Columbia.
3. Tomlinson, C. J. et al. Remote sensing land surface temperature for Meteorology and climatology: A review, *Meteorological Applications*, 2011, 18, 3, 296–306.
4. Kuenzer, C. et al. Spaceborne thermal infrared observation – an overview of most frequently used sensors for applied research, in: Kuenzer, C. and S., Dech, (eds) *Thermal Infrared Remote Sensing SE-7*. Springer Netherlands (Remote Sensing and Digital Image Processing), 131–148. DOI: 10.1007/978-94-007-6639-6_7.

5. Landsat Missions, <https://landsat.usgs.gov/using-usgs-landsat-8-product> (last day accessed November 26, 2017)
6. ASTER, <https://asterweb.jpl.nasa.gov/> (last day accessed November 26, 2017)
7. MODIS, <http://modis.gsfc.nasa.gov/about/design.php> (last day accessed November 26, 2017)
8. MODIS Land Team, <http://landval.gsfc.nasa.gov/ProductStatus.php?ProductID=MOD11> (accessed Nov. 26, 2017)
9. CBERS, <http://www.cbears.inpe.br/ingles> (last day accessed November 26, 2017)
10. eoPortal Directory, <https://directory.eoportal.org/web/eoportal/satellitemissions/> (last accessed November 26, 2017)
11. Stathopoulou, M. and C. Cartalis, Downscaling AVHRR land surface temperatures for improved surface urban heat island intensity estimation, *Remote Sensing of Environment*, 2009, 113, 12, 2592–05.
12. Zhiwei, Y., G. Huili, and Z. Wenji, Subpixel urban area thermal pattern analysis using ASTER and SPOT-5, in: 2009 Joint Urban Remote Sensing Event. College of Resource Environment and Tourism, Capital Normal University, Beijing, China (2009 Joint Urban Remote Sensing Event).
13. Cao, G. et al. Analysis on the spatial distribution of urban heat island with downscaled FY-3A VIRR land surface temperature', in Proceedings of the 2nd International Workshop on Earth Observation and Remote Sensing Applications, EORSA 2012. LREVCS, China Meteorological Administration, Beijing, China (2nd International Workshop on Earth Observation and Remote Sensing Applications, EORSA 2012), 2012, 36–40.
14. Zakšek, K. and K. Oštir, Downscaling land surface temperature for urban heat island diurnal cycle analysis, *Remote Sensing of Environment*. 2012, 117, 114–124.
15. Sobrino, J. et al. Review of High Resolution Thermal Infrared Applications and Requirements: The Fuegosat Synthesis Study, in: Kuenzer, C. and S. Dech, (eds) *Thermal Infrared Remote Sensing SE-10*. Springer Netherlands (Remote Sensing and Digital Image Processing), 2013, 197–214.
DOI: 10.1007/978-94-007-6639-6_10

СПЪТНИКОВИ СЕНЗОРИ, ИЗПОЛЗВАНИ ЗА ТОПЛИННИ ДИСТАНЦИОННИ ИЗСЛЕДВАНИЯ

Ив. Янев

Резюме

Настоящата статия прави преглед на най-използваните съвременни спътникови мисии, работещи в топлинния диапазон на електромагнитния спектър. Обсъдени са основните приложения в изследванията на околната среда с помощта на данни от спътникови мисии като Landsat, ASTER, MODIS, CBERS и HJ-1B. В заключение се очертават някои проблеми и бъдещи перспективи пред спътниковите топлинни дистанционни изследвания.

ASSESSMENT OF THE LAND SURFACE TEMPERATURE DYNAMICS IN THE CITY OF SOFIA USING LANDSAT SATELLITE DATA

Ivan Yanev¹, Lachezar Filchev²

¹*ESRI Bulgaria Ltd.*

²*Space Research and Technology Institute – Bulgarian Academy of Sciences
e-mail: ivan.yanevmail@gmail.com*

Abstract

The article presents the first attempt to analyse the urban heat island of the city of Sofia using satellite data. For this purpose the thermal data from Landsat ETM+ and TIRS sensors have been used. A statistical analysis of the results was carried out as well as an analysis of the changes in the surface temperature for the selected time interval – 2000–2015. The impact of the type of land cover was analyzed. For this purpose, a visual land-cover classification has been drawn up, whereby the surveyed territory is divided into 16 classes. A detailed analysis of the data over the entire survey period shows a gradual rise in the city's temperature due to the change in the urban environment. One of the conclusions of the study is that thermal images over time can be successfully used to detect changes in the land cover by temporal analysis.

Introduction

With the advent of the first satellites equipped with sensors in the thermal range of the electromagnetic spectrum in the early 1970s, the Earth's surface temperature began to be investigated also by remote sensing means. The possibility of urban areas being identified by thermal data obtained from a satellite was first demonstrated by [1, 2]. In this study the authors used data from the SR (Scanning Radiometer) satellite sensor ITOS-1 (Improved TIROS Operational Satellite). Then, with the commissioning of new thermal sensors worn by various satellite platforms, a more in-depth study of the city's thermal island began through satellite data.

One of the pioneers to explore urban heat islands by remote sensing methods are [2, 3–8]. While [1] attempted to roughly outline the boundaries of cities, Matson et al. (1978) uses thermal data (10.5–12.5 μm) from the NOAA Very High Resolution Radiometer (VHRR), recorded overnight, to investigate differences in temperature on urban and non-urban surfaces; [5] uses data (10.5–12.5 μm) from the Heat Capacity Mapping Mission (HCMM) to estimate the spatial coverage and intensity of urban surface warming. Later on [7] use

Advanced High Resolution Radiometer (AVHRR) thermal data to assess the intensity of the city's thermal islands in three coastal cities in North America.

Although the Landsat 5 Thematic Mapper (TM) mission started in 1984, we do not have data for research using TM sensor data over the next few years of satellite operation. The graphs presented above for the number of articles per year show that only in 1990 there were more research, with a major part based on Landsat 5 TM. Authors such as [9] evaluate the feasibility of the thermal band of the TM, which has 120 m spatial resolution, to classify terrain in urban environments. The team [10] investigated the model of surface temperature in Tokyo, and [11] the impact of the urbanization process on the formation of thermal islands. The so-called "heat sinks" and the effect of green areas in the city have been analysed for the first time by [8, 12]. The thermal radiation of various discrete surfaces were studied by [13], and [14] map the formation of micro-UHI.

Study area

The area of interest is the city of Sofia – the capital and the biggest city of Bulgaria, and the 16th largest city in the EU [15]. It is located in the West part of the country in the central part of the *Sofia* valley ($\lambda = 23^{\circ}19'28.443''$ E, $\varphi = 42^{\circ}41'48.492''$ N) which in turn extends from North-West to South-East between *Balkan* Mountains on the North and the mountains *Viskyar*, *Lyulin*, *Vitosha*, *Lozenska* on the South, the rivers *Slivnishka* and *Gaberska* on the West and to the East it borders with *Vakarel* Mountain. The entire character of the landscape defines the climate of Sofia. According to climate classification adopted in Bulgaria, Sofia falls into temperate continental climate subzone of European continental climate zone [16].

The city of Sofia is constantly growing in population. The official population estimate in 2015 is around 1.3 million people (2011 census) [17].

Materials and Methods

Satellite data

Considering the timeframe of the study, we have used data from Landsat ETM+ and Landsat TIRS. Both sensors allow acquisition in the thermal range. Given the fact that the former has one thermal band and the second one – two, a different approach to image processing should be used. According to official information about Landsat 8 the mission (URL: http://landsat.usgs.gov/Landsat8_Using_Product.php), however, thermal bands 10 and 11 are affected by heat outside the range of the normal field of view called stray light. Band 11 is significantly more affected than Band 10, so it is recommended that users refrain from using Band 11 in split-window LST extraction algorithms. For this reason, only Band 10 is used on Landsat 8. Below, we will look at various processing

methods for both sources. The Landsat data used is level 1T imagery downloaded from URL: <http://earthexplorer.usgs.gov/>, as well as Landsat Higher Level Science Product Product downloaded from URL: <http://espa.cr.usgs.gov/>. Both products use the original, unprocessed Level 1 product as original data and are radiometrically and geometrically corrected, with a 30 m spatial resolution in the thermal range (resized from 60 m ETM+ and 100 m TIRS), Universal Transverse Mercator (UTM), World Geodetic System (WGS) 84 and GeoTIFF (URL: http://landsat.usgs.gov/Landsat_Processing_Details.php). The higher-level product contains most of the images since 1982 and includes reflection and brightness data recorded by the sensor (Top of Atmosphere Reflectance and Brightness Temperature), Surface Reflectance and related indexes, such as Normalized Difference Vegetation Index (NDVI), etc., as well as Cloud Mask. In addition, images can be downloaded in a different format, coordinate system, spatial range, and pixel size. It is planned to have a ready LST product in the future. Some of the available Landsat images were dropped out of the analysis for a variety of reasons – cloud cover, missing product data of higher level, or missing data on atmospheric parameters. Therefore, only valid images totaling 35 – 6 images from Landsat 8 between 2013 and 2015 and 29 images from Landsat 7 from 2000 to 2015 – were included in the analysis. After a careful review of all the images, a difference in quality of images. In spite of the lower spatial resolution, the Landsat 8 images are much more pronounced than the thermal island in the city, while those from Landsat 7 appear to be slightly fuzzy, possibly due to the fact that Landsat 8 has almost twice the dynamic range – 12 bits against 8 bits for Landsat 7. This means that the first sensor records 4096 shades while the second only 256 shades of gray. However, both types of data require a very careful selection of the color scheme of the images in order to best visualize the temperature differences.

Meteorological data

We have used meteorological data provided by National Institute of Meteorology and Hydrology (NIMH-BAS) in order to evaluate the accuracy of the derived temperature values. For the date of each image, we have three ground measurements of the land surface temperature at 7, 14 and 21 h local time. Since Landsat's daytime images are captured at about 12 h local time, and at night around 23 h, we used the values of 14 and 21 h for validation of LST extraction methods.

Satellite data processing

The first step in the processing of thermal satellite images is the conversion of pixel values into at-sensor spectral radiance. The conversion is done by the following formula:

$$1) \quad L_{\lambda} = M_L * DN + A_L,$$

where: L_{λ} is the spectral emission registered at sensor (Watts/(m² * srad * μm)); M_L is a multiplicative scale factor from the metadata (REFLECTANCE_MULT_BAND_x, where x is the band number); A_L is an additive scale factor from the metadata (REFLECTANCE_ADD_BAND_x, where x is band number).

It is clear that each type of earth land cover has a different emissivity that is influenced by the instant physical state of the object. Therefore, it is important that the value of ε is measured at the time of the satellite platform's passage for each individual image. Because we do not have such field measurements, we need to use one of the methods to calculate this parameter. An average value (based on published measurements or spectral libraries) for each type of land surface is assigned to the classification method, but the current state of the site may not be taken into account. Therefore, we decide to use the method using NDVI (taken from the Landsat product), where the values for one type of land cover can vary depending on the time of data acquisition. We use threshold values for NDVI as follows:

- If NDVI < 0.2 type of land cover is considered soil, and $\varepsilon = 0.97$;
- If NDVI > 0.5 type of land cover is considered vegetation, and $\varepsilon = 0.99$;
- If $0.2 \leq \text{NDVI} \leq 0.5$ type of land cover is considered mixed,

$$2) \quad \varepsilon = mP_v + n,$$

where:

P_v is vegetation proportion,

$$3) \quad P_v = \left[\frac{\text{NDVI} - \text{NDVI}_{\min}}{\text{NDVI}_{\max} - \text{NDVI}_{\min}} \right]^2$$

$$m = \varepsilon_v - \varepsilon_s - (1 - \varepsilon_s)F\varepsilon_v,$$

$$n = \varepsilon_s + (1 - \varepsilon_s)F\varepsilon_v,$$

where:

ε_v is vegetation emissivity,

ε_s is soil emissivity,

F is a geometry factor = 0.55, therefore the final equation for ε (at NDVI between 0.2 and 0.5) is:

$$4) \quad \varepsilon = 0.004P_v + 0.986$$

We have used two methods for calculating surface radiance the radiative transfer equation (RTE) and Jimenez-Munoz and Sobrino (SC) Single-Channel

Algorithm [18]. Transformation of the surface emissivity into surface temperature for LST retrieval from thermal images is to convert the resulting surface radiance value to a LST.

$$5) \quad T = \frac{K_2}{\ln\left(\frac{K_1}{L\lambda} + 1\right)},$$

where: $K_1 = c_1/\lambda^5$, $K_2 = c_2/\lambda$, including c_1 and c_2 , which are 1st and 2nd radiation constants, and λ is effective wavelength.

Table 1. K_1 and K_2 values for Landsat 7 and Landsat 8 thermal bands

	L7B6	L8B10
K₁	666.09	774.89
K₂	1282.71	1321.08

Results and Discussions

Here we present a brief visual analysis of the obtained images and in the following paragraphs we will analyze in more detail the influence of the type of land cover, the changes in the land cover, the change and the dynamics of the surface temperature.

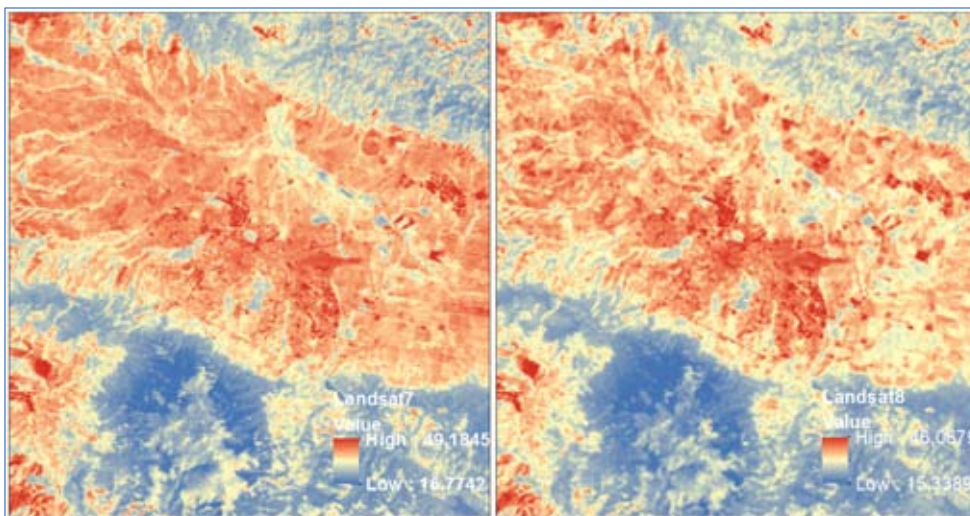


Fig. 1. Average of all images used in the analysis for Landsat 7 (left) and Landsat 8 (right)

On Fig.1 is depicted the influence of the city on the LST. At first glance, several characteristic areas with particularly elevated temperature values in the range of 35÷45 °C stand out. These are the districts around Sofia Airport and to the south of it in the *Druzhba* neighborhood, the Center quarter, as well as in the northwestern part of the *Nadezhda* district. The high temperature of the whole valley of Sofia is also clearly visible, compared to the surrounding mountains of *Stara Planina* in North and *Vitosha* in the South. During the summer months, the bare and dry soil has values close to those on the impermeable surfaces of the city. This is evidenced by the increase in temperature on the mountain ridges. In addition to elevated temperatures, however, the outlines of larger parks such as *South Park* and *West Park*, which values are significantly lower – about 23÷24 °C, are clearly visible. A cool strip along the *Iskar* River valley also stands out. As we observe the temperatures for a period of 15 years, it is especially interesting to see if and in which direction the LST values are developing. For this purpose, we divided the images into three intervals – from 2000 to 2005, 2006–2010 and 2011–2015. Thus, the images are divided in the first interval of four images, and in the next two 12 and 19 respectively.

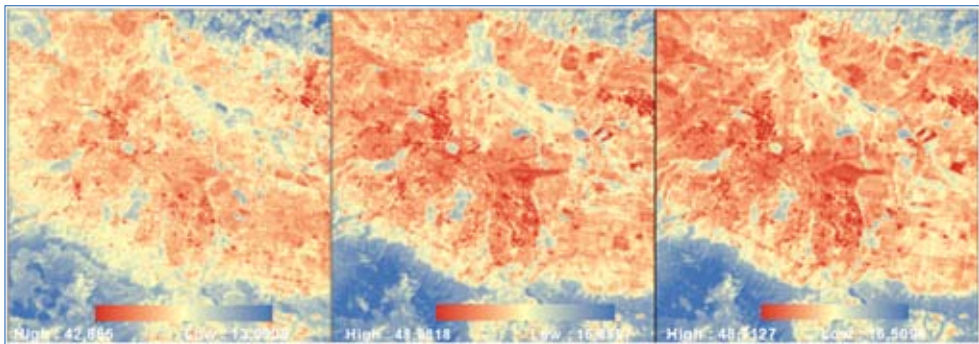


Fig. 2. LST averaged over three time intervals: 2000–2005, 2006–2010, and 2011–2015 (left to right)

The tendency for a gradual increase in reddish areas in images is seen, and this is much more noticeable between the first two intervals. When carefully examining the images on the appropriate scale, a saturation at each of the temperature ranges is noticed. Once a tendency for surface temperature increase is observed at these intervals, it is necessary to follow the heat stroke a little in detail. For this purpose, we have devoted one image to each of the years which we have, giving priority to the dates around and after mid-July. This gave us a total of 13 images under the most similar acquisition conditions, which we averaged in proportions in five consecutive acquisitions with a displacement of each proportion in a single forward, i.e. if P1 covers the interval between 2000 and 2004, then

$P2 = P1 + 1$ or from 2001 to 2005, etc. Thus, a total of 9 five-year averaged images were obtained.

The different methods of data averaging have a significant impact on the absolute values of the surface temperature. In the first "Method 1", within the selected timeframe, all the available images in the database are determined by the image selection criteria. The second "Method 2" includes selected images captured under the most similar conditions during the warmest and driest period of the year. This leads to an increase in surface temperature and a distinct manifestation of the urban heat island. In the following Fig. 4, the visualization of the UHI for the period 2011–2015 can be visually compared to the two averaging methods.

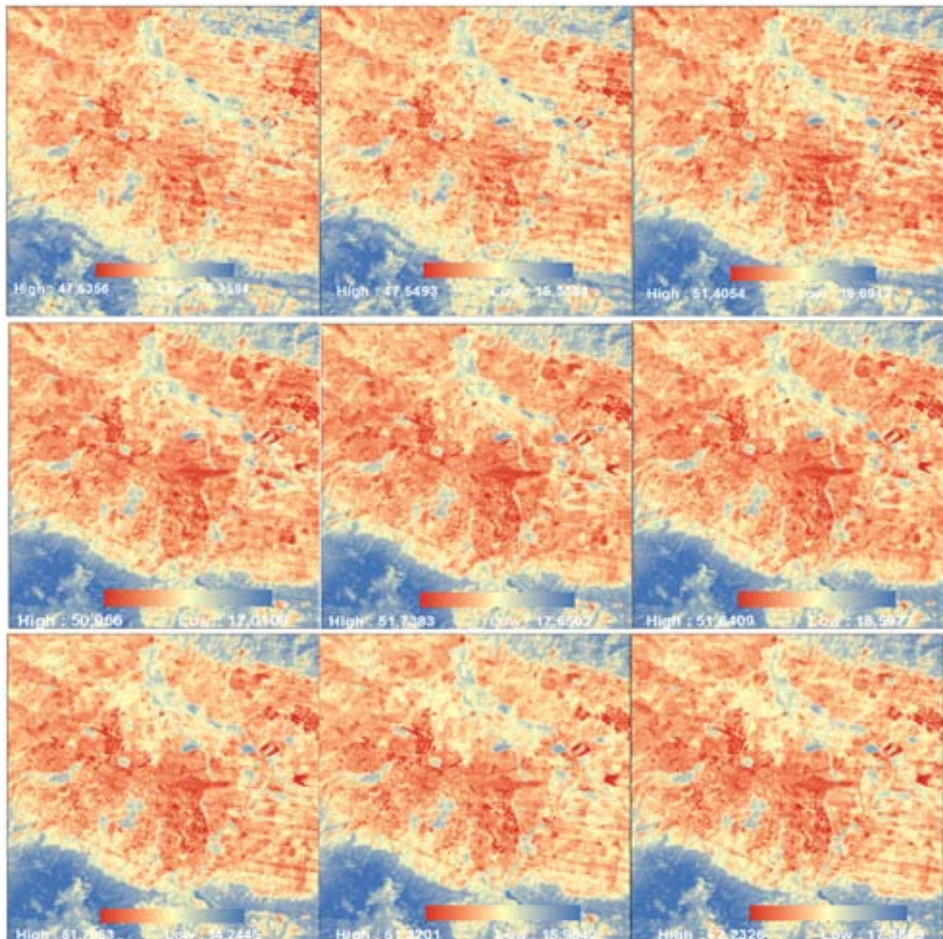


Fig. 3. LST averages for 9 five-year intervals, respectively 2001–2007, 2002–2008, 2005–2009, 2006–2010, 2007–2011, 2008–2012, 2009–2013, 2010–2014, and 2011–2015 (sequentially from left to right).

In both methods, the same rating for surface temperature visualization is used. A Natural Breaks classification of seven classes has been used. The second method clearly shows an increase in pixel values. The UHI is apparently distinct on the first image where distinctive areas of extremely high temperatures are distinguished. In addition to the city, the increase in pixel values is also observed in the sub-urban areas – the *Sofia* valley resembles the urban area of the first image and in the surrounding mountains the bare mountain ridges are outlined.

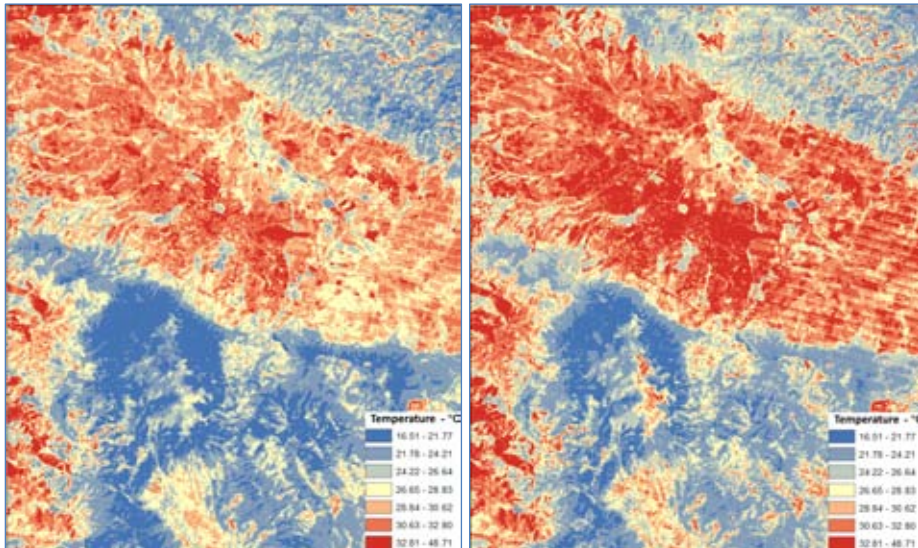


Fig. 4. LST averages for 2011–2015 by "Method 1" (left) and "Method 2" (right)

Spatial model of the urban land surface temperature

The city of Sofia forms a thermal island with typical spatial characteristics. Because of the terrain of the plain in the Sofia valley, a clear cliff or steep temperature gradient at the border with the town is observed only from the South, where the city territory borders directly with the *Vitosha* Mountain. From North, West and East there is a slight decrease in the temperature of the border between the town and the *Sofia* valley. The city is characterized by great heterogeneity of the temperature profile. The so-called "plateau", or the territory of a gradual increase in temperature from the periphery to the center of the city, is often interrupted by micro-urban thermal islands in places with large anthropogenic sites and industrial areas and so-called "heat sinks" or especially cold areas formed by large urban parks and places with distinct dense vegetation. The thermal profile is distinguished by a clear peak of the temperature in the city center.

When it comes to the results obtained, it is interesting to look at the difference in the temperature profile depending on the spatial direction. By building a Northwest-Southeast profile (Fig. 5a), the temperature profile is closer to the theoretical profile of an UHI. Surface temperature outside the city ranges from 30÷32 °C. At the city border, micro-UHIs are caused by industrial objects rising to 36÷38 °C, after which the temperature in the city moves about a degree over that outside the city in the range of 31÷33 °C until reaching the first cold zone due to the *West Park*. The temperature here decreases to 25 °C, and then it is constantly rising to reach the central city area. The temperature reaches 37 °C. Near the peak of the temperature in the center lies another cold zone linked to the *South Park*. The temperature then re-runs in the range of 30÷34 °C with interruptions of microUHI exceeding 40 °C. At the eastern boundary there is *Vrana Park*, which forms another cold area, after which the temperature in the extra-urban part gradually decreases from 30 °C downwards.

The temperature profile with the Southwest-Northeast direction is also interesting. Visually, the higher temperature in the North of the city is visible vis-à-vis the South. This is due to the southern neighborhoods situated at the foot of the *Vitosha* Mountain. They are characterized by low density of construction, lack of large anthropogenic sites, and more vegetation. The temperature profile on Fig. 5b start from the mountain where the temperature is ~ 20 °C before it reaches a brightly defined cliff on the city's border where the temperature rises sharply to 28 °C. Then there is a rapid temperature growth of up to 30 °C through the built-up footsteps of *Vitosha* Mountain. After the Sofia ring road, the temperature gradually rises to more than 33 °C in the center of the city and over 34 °C in the industrial zone to the North before passing through a typical cold zone created by the park of the Central Sofia Cemetery where the temperature drops to 25 °C. Thereafter, the temperature profile follows a smooth stroke at a decrease of 33 °C to about 30 °C at the border with the extra-urban section, and continues the gradual decrease outside the city to about 28 °C.

To investigate the temperature increase by moving away from the mountain, we divided the urban area into several zones. For this purpose, we used areas or zones, meaning the boundaries of the city districts and the obtained LST after averaging the values for the period 2011–2015. In the two southern-most zones are the districts situated between *Vitosha* mountain and *Okolovrasten pat* Str. In the "Intermediate zone" bordering part of the "South Zone – East" there are several neighborhoods where there is still significant involvement of undeveloped areas. The zone located in the "Middle zone" of the city covers the neighborhoods between *Ovcha kupel* quarter and *Mladost* quarter. In the next zone there are the neighborhoods on the *Lyulin* quarter – *Druzhdza* district and north of them. In particular zones are the "Center" quarter and the bigger urban and cemetery parks. For each zone, we calculated the average temperature. The following Fig. 7 show the temperature rise in the city from the South to the North by > 4 °C.

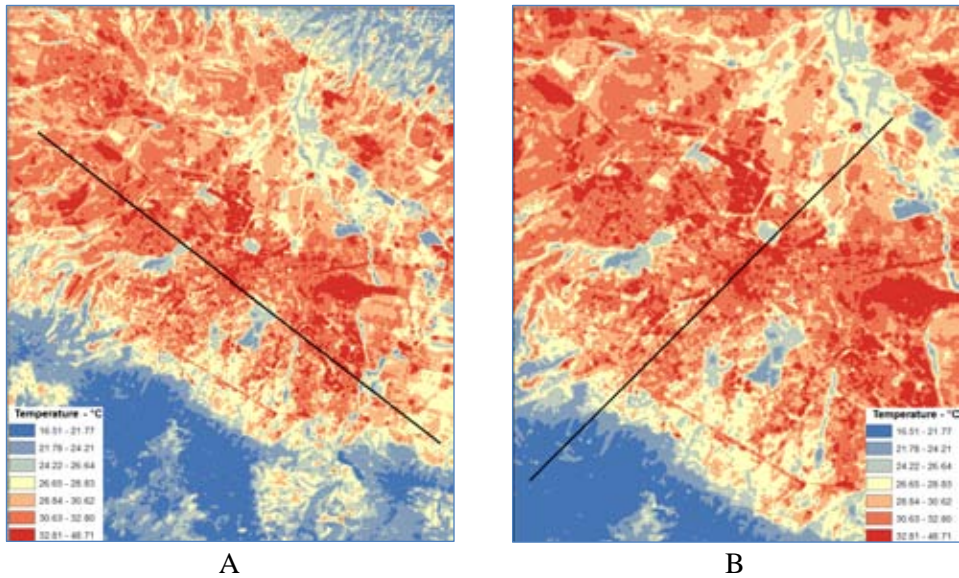


Fig. 5. (A) Temperature profile in Northwest-Southeast direction and (B) temperature profile in Southwest-Northeast on selected Landsat images ("Method 2") for 2011–2015.

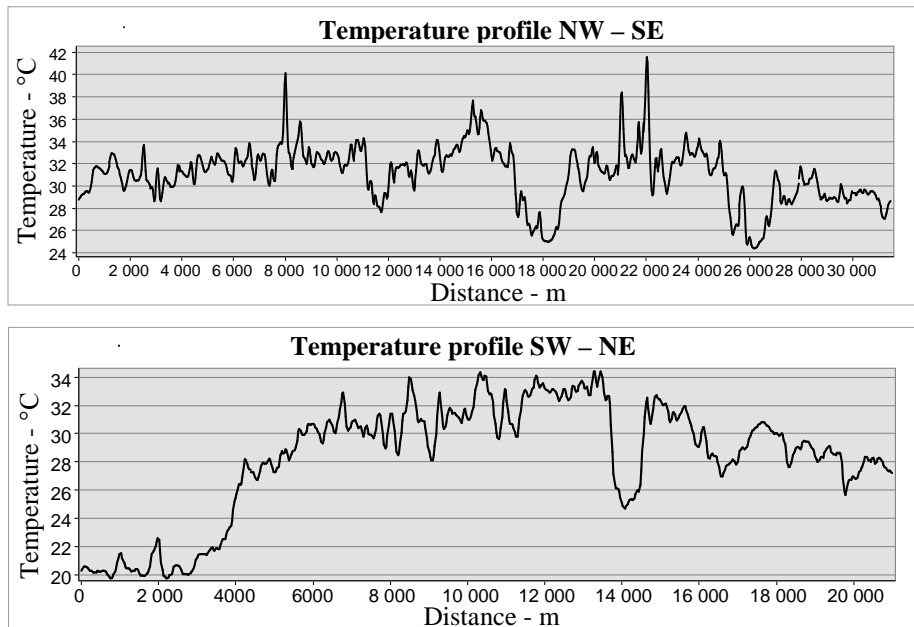


Fig. 6. Profile of the LST for Northwest-Southeast direction on selected Landsat images ("Method 2") for the period 2011–2015 (above). Southwest-Northeast LST on selected Landsat images ("Method 2") for the period 2011–2015 (below).

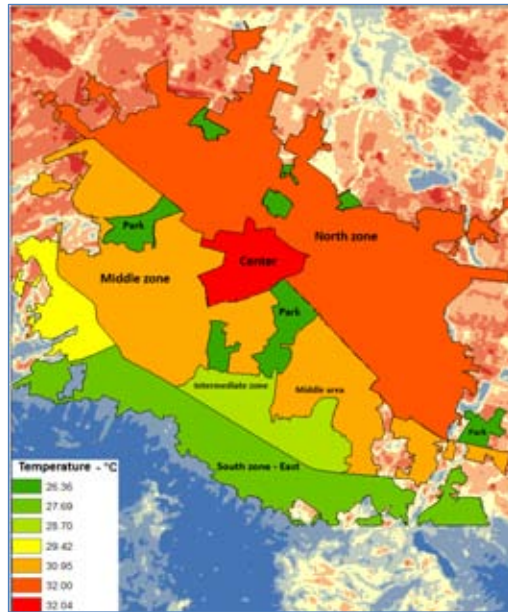


Fig. 7. Zoning of LST from South to North for selected Landsat images 2011–2015

Land surface temperature by land cover type

A number of factors previously commented influence the model of surface temperature in the urban environment and the formation of UHI. However, the most significant influence is the land cover. In order to assess the surface temperature in this aspect, we performed a visual classification of the studied area according to the type of the surface, the height and the density of the buildings, and the presence of vegetation. Thus, a total of 16 types of land cover are allocated, see Fig. 8: "Center" characterised by massive construction characteristic of the city center, dense built-in, adjacent buildings forming continuity along the streets; "Dense built-up urban area" – mostly high-rise building with a small distance between buildings"; "City centre" with tall buildings with great free space between them; "Dense sub-urban" with densely built areas with predominantly low-rise and a "Low-rise" subdivision including industrial sites and greater distance from the previous class; "Industrial area" with mainly industrial sites and almost no vegetation; "Village" of a low built-up area with a significant presence of vegetation and gardens; "Park" with dense vegetation mixed with anthropogenic objects; "Village zone" similar to the class of a densely built suburb but outside the urban territory; "Barren land" are areas without construction and high vegetation, mainly tilled arable land; "Forest" with high forest species without free spaces; "Sparse vegetation" is high vegetation with free spaces; "Perennials" are plantations with perennial crops; "Water bodies", "Airport"; and "Streets".

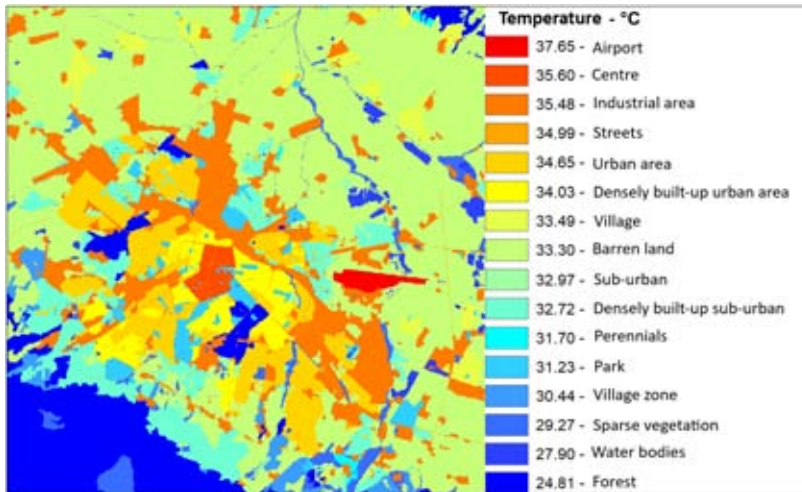


Fig. 8. LST based on visual classification on selected images for 2010–2012

Since the orthophoto images from 2011 were used for the visual land cover classification, images from the same year should be used for the analysis. Due to problems with Landsat 7 SLC, we can not only use a single 2011 image. For the purpose of better representation and consistency of the analysis, we used images from the previous and next year. This gives an LST image with averaged values for 2010, 2011, and 2012. The visual image classification and the resulting image were used to obtain the average temperature value for each class. From the above image, it can be seen that the city center is not the hottest point. This role is occupied by Sofia Airport, which can be considered as a separate site, as only the runways and the empty spaces between them are included in this class. This combination of predominantly impervious horizontal surfaces spaced from vertical objects forming shadows and voids, which also are significantly heated under dry conditions and prolonged exposure to direct sunlight, results in the formation of the highest temperature above 37.5 °C in the thus performed classification. In this line of thought, streets should demonstrate the same high values as they also form a class of impervious surfaces. Here, however, the temperature values are influenced by the high vegetation along some streets that lowers the temperature both through the shadows formed and by hiding them from the field of view of the Landsat sensor. Besides vegetation and neighboring buildings, they form shadows on the streets, which further reduce the temperature. The set of factors results in an average of 34.99 °C for class "Streets". The "Center" class shows a marked peak in the central city area. Here the vegetation is limited by the extremely dense and high-rise construction, which is almost continuous along the streets. Very close in temperature value is the "Industrial area" class. Both classes reported a value of

about 35.5 °C. However, some industrial zones or individual industrial sites may significantly exceed these values on Fig. 9 is shown a rooftop of large industrial object heated to > 50 °C.

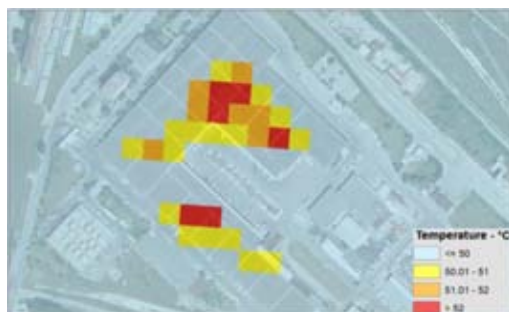


Fig. 9. A micro-UHI formed by a large industrial site which temperature exceeds 50 °C

Particularly interesting are the classes "Urban area" and "Densely built-up urban area". Despite the denser construction in the second class a lower temperature of about 0.6 °C is reported. It combines high and low-rise buildings, as well as the presence of more vegetation, which is typical for low-rise sites. Characteristic of the first class are the high-rise residential buildings with a greater distance occupied by empty spaces. The rise in temperature is due, on the one hand, to the large facades directly exposed to sunlight, and on the other to the characteristic very high heating of the empty areas, under certain conditions approaching impervious surfaces. The difference in temperature between the two described types of surface is even greater if we take into account only individual zones that are closest to the description of the class. A very characteristic area approximating to the description for class "Urban area" is *Lyulin* district. The same applies to the *Reduta* and *Geo Milev* districts as far as the "Dense built-up urban area" class is concerned. Only those areas are represented in Fig. 10, the data and methods of analysis used to be identical to the above.



Fig. 10. A comparison between characteristic areas for "Urban area" (A) and "Densely built-up urban area" (B)

The "Village" and "Densely built sub-urban" classes fall into one category with the difference that the first falls within urban territory. The reason the class "Village" to have a higher temperature of near 0.8 °C probably lies in the southern neighborhoods of the town located at the foot of the *Vitosha* Mountain. These areas are densely built with low-rise buildings, but also have a significant presence of high vegetation. Considering that these areas occupy a significant part of the whole class can be explained the relatively large difference in temperature ratio. Similar is the reason why the "Sub-urban" class, which is characterized by more dilute, often industrial buildings and bare areas, has a near 0.3 °C higher temperature compared to the "Dense sub-urban" class.

More specific is the "Barren land" class. It has been attributed to arable and uncultivated areas without anthropogenic sites and without high vegetation. Here are the most common fields occupied by grasses or areas sown with low crops. The bare terrain is characterized by high temperatures, especially during the summer months, with prolonged droughts and hot days. This is the reason sometimes such areas are difficult to distinguish from impervious surfaces. In addition, lower vegetation loses its water content more quickly, which is another factor for the high average temperature of the class of 33.3 °C. The following Fig. 11 demonstrate the heating of a barren land to about 38 °C.



Fig. 11. "Barren land" class surface temperature

The "Park" class is a territory occupied by high vegetation and anthropogenic sites such as alleys, low buildings, and other waterproof objects. For example, large parts of the *Borisova Garden* and *West Park* parks fall into the "Forest" class. Therefore, the "Park" class forms a temperature of 31.23 °C, which is 0.8 °C above the temperature of the "Village zone" class, which is characterized by sparsely built areas with low-height buildings and rich vegetation. For comparison, the "Forest" class records the lowest temperature in the classification – 24.81 °C, which is close to 6.5 °C lower than the "Park" class. It is actually interesting to note that "Water bodies" have a higher temperature to "Forest" class.

The "Water bodies" class shows 27.9 °C, which is > 3 °C above the "Forest" class, see Fig. 12. This is due to several reasons. In the classification, there are small objects such as urban pools and water bodies in parks that fail to compensate for the impact of the pixel portion of the image falling outside the water. In fact, this is also one of the possible applications of the thermal images. They can detect water bodies that are not highlighted at the time of acquisition, and can hardly be distinguished by an RGB image composite.



Fig. 12. "Water bodies" class surface temperature



Fig. 13. Display of a dry water object (left) on a thermal image (right)

The following Fig. 14 show the course of temperatures by classes. The red line represents an average value of selected images with the most similar acquisition conditions for the 2010–2012 period. The blue line contains averages for the same period but for all available images in the database. These two lines represent the same period, and it is seen that as the maximum temperatures increase, the impact of waterproof areas is increased. It is interesting to compare the 2010–2012 and the last five-year (2011–2016) averages, with all the available images taking part. The graph shows a definite increase in temperature, especially in classes with predominantly impervious areas. Earlier we mentioned that as the maximum temperatures increase, the impact of impermeable surfaces increases. To support this statement, a graph drawn from the temperature difference between the two

groups of images for the period 2010–2012 is shown in Fig. 14. The gradual reduction of the difference between the classes with mostly impermeable surfaces to the classes with increased vegetation influence is seen.

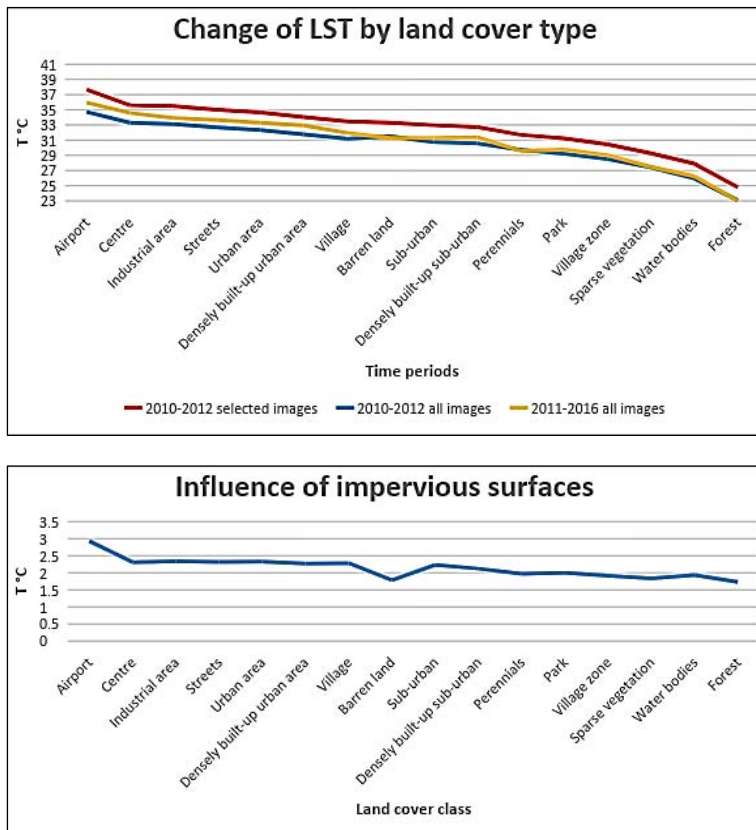


Fig. 14. Change of surface temperature by type of land cover (top). Influence of impervious surfaces on the surface temperature (bottom).

Estimation of the land cover change according to LST

As it has already become clear, waterproof (anthropogenic) surfaces are heated significantly more than the permeable (natural) surface. Considering the difference in heating of different surfaces, thermal imaging can be used to detect changes in the earth's surface. The Fig. 15 show the difference in temperature between images from 2001 to 2015. Blue zones mean that the temperature has fallen, and red zones suggest an increase in value.

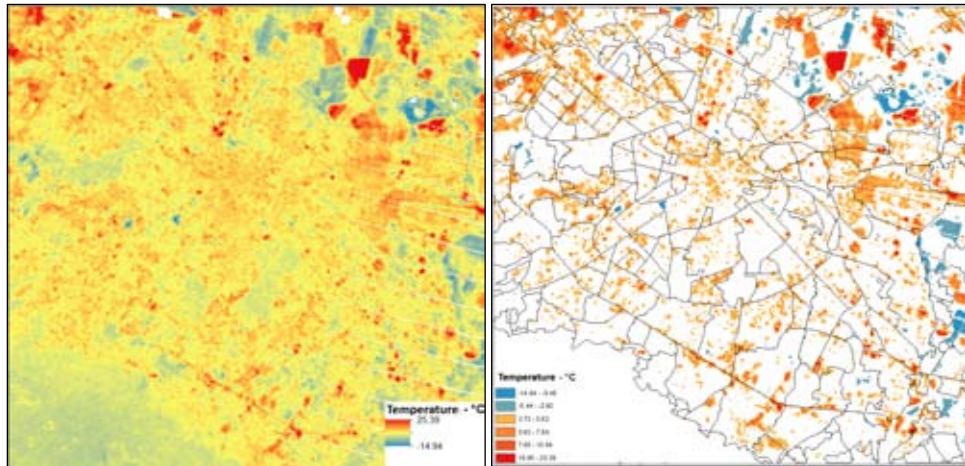


Fig. 15. Difference in the LST between 2001 and 2015 images (left), zones with significant difference in LST in 2001 and 2015 images (right)

The left image on Fig. 15 show warming in the city center and other parts of the city. In addition, there are some strong areas where objects are built or removed. The development of the so-called "Southern Ring Road".

Along this part of the ring road there are numerous industrial or office buildings that raise the temperature. The resulting image is further classified to remove the areas with a minimum difference in the values depicting the most significant changes. On the right image on Fig. 15 are clearly seen the areas with more significant changes. This result confirms the warming in the city center. In addition, larger areas with higher values are observed in the North in *Orlandovtsi*, in the West in the *Lyulin*, *Fakulteta*, *Ovcha Kupel*, Southeast along the Ring Road and *Simeonovo*, *Hladilnika* quarter between *South Park* and *Loven Park*, *Sofia Airport* and the *Levski* quarter. Areas with reduced temperatures are significantly less. Within the city, there are two such areas close to the city center, which are a result of the removal of large industrial sites. There are many zones with low temperatures in the East and North-East direction. However, only one of them is a consequence of a change in the land cover, namely the formation of a new water body. The rest are mostly arable land where it is important whether the land is plowed or sown. The red fields in the northeastern and northwestern suburbs are also due to the fields, as the bare earth surface is significantly more heated.

We will look at some of the more characteristic changes. Fig. 16 show some instances of development of new city parks, emergence of large industrial sites, removal of industrial sites, and appearance of new water bodies. Changes in the land cover were found by the above analysis of the surface temperature difference in 2001 and 2015.

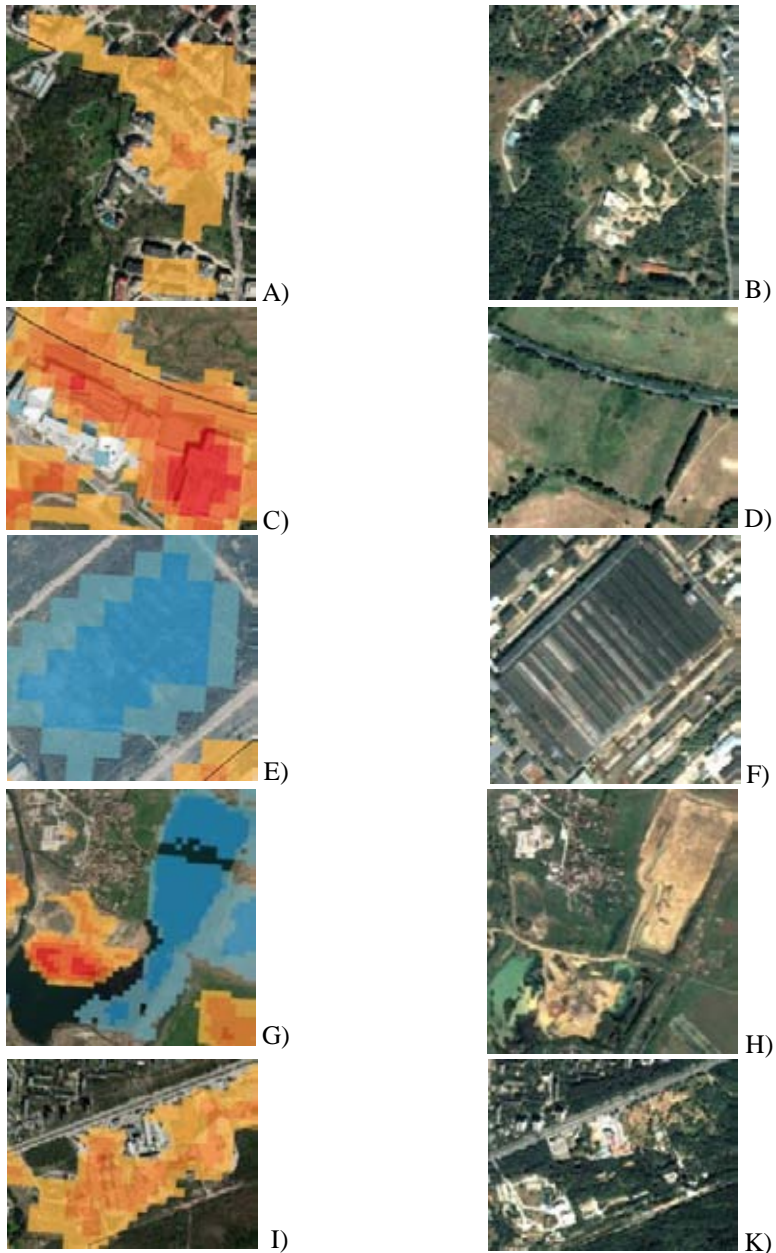


Fig. 16. Part of South Park: 2015 (A) and 2001 (B); construction of industrial sites along the Ring Road: 2015 (C) and 2001 (D); removal of industrial sites in "Krasna Polyana 3": 2015 (E) and 2001 (F); formation of a new water body and correction of an old one: 2015 (G) and 2001 (H); part of the Hunting Park: 2015 (I), and 2001 (K)

Despite the possibility of detecting changes in the land cover, an automatic classification and assessment of the changes would be quite difficult to implement. The reasons lie in the low SR of the thermal bands for such purposes, the specific emission of the different materials, and the acquisition conditions. In our case, daytime imagery is selected from the hottest and driest period of the year. Under such conditions, the terrain is heated almost like an impermeable surface, making it even more difficult to remove the impermeable areas, see Fig. 17.



Fig. 17. The difference in the arable LST between the two images is 16.6 °C (left). In the middle, the levels are close to the time of shooting in 2001 and to the right in 2015.

Since the factors influencing the temperature trend are too much there is no way to assign a specific value or range of temperature to a given type of land cover. At present, it is difficult to automatically classify the earth's surface automatically with thermal imaging, and from there to analyze the changes. However, the trend of surface temperature can be judged for the development and alteration of the surface as a whole.

Estimation of the LST dynamics for the investigated time period

As from the initial visual analysis of the processed images, we have seen that there is a tendency towards increasing saturation of the pixel values. If we compare two images of different years, the analysis will not be correct, as the temperature is quite variable. Therefore, working on average data, we have reason to make general conclusions about changes in the urban environment.

All images averaged with "Method 2" are used in Fig. 18. For each class of the earlier visual classification, we took the temperature values by a period. Over time, a gradual rise in temperature is evident, possibly due to the increase in waterproof surfaces at the expense of green areas. To confirm the rise in temperature values we will also use the boundaries of the earlier zoning from the South to the North. The bottom image on Fig. 18 confirm the temperature increase in all zones.

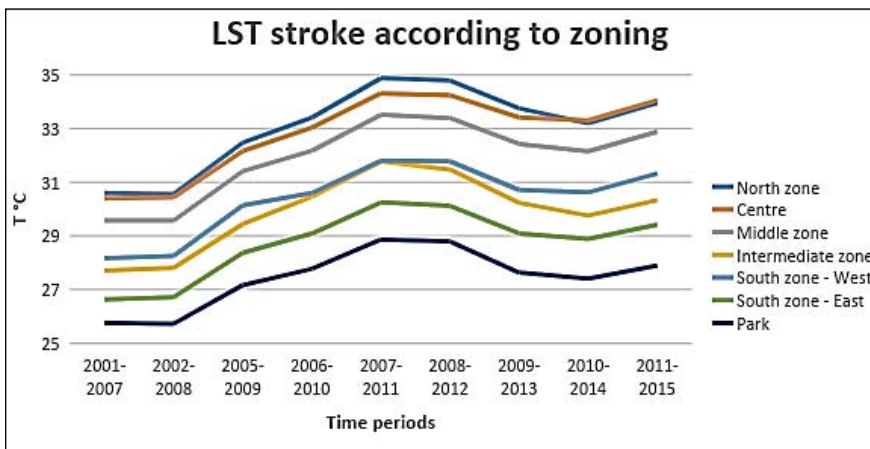
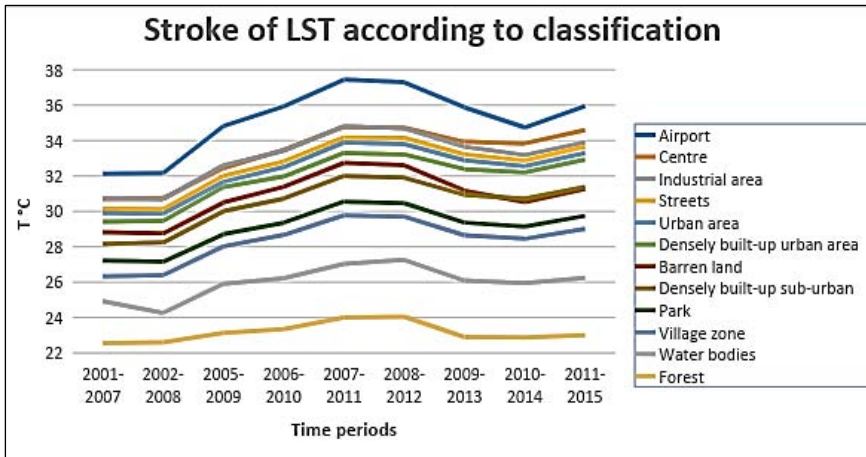


Fig. 18. LST course for different land cover classes by period (selected images, "Method 2") (top) and LST course for different zones by period (selected images, "Method 2") (bottom)

However, the absolute temperature difference between the first and the last period is different. From the figure, it appears that areas with less vegetation have increased the temperature more than those with more vegetation. The temperature in the *central city* area increases by > 3.5 °C for the whole period, the *Northern* and the *Middle zone* by ~ 3.3 °C, while in the *Intermediate zone* and the *South Zone – East* the value increases by about 2.7 °C. *Parks* show the lowest increase of 2.1 °C.

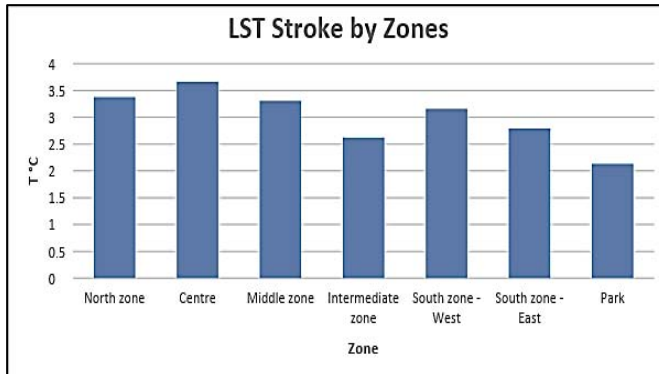


Fig. 19. LST Stroke in the Sofia city zones

However, we can not but notice the extremely similar temperature increase for all areas, despite the differences in the land cover. The same is true of the upper graph showing the course of temperature according to the earth cover class. By analyzing the temperature dynamics between all zones, we find that the correlation between the zones is too high. The lowest coefficient between two zones is 0.972.

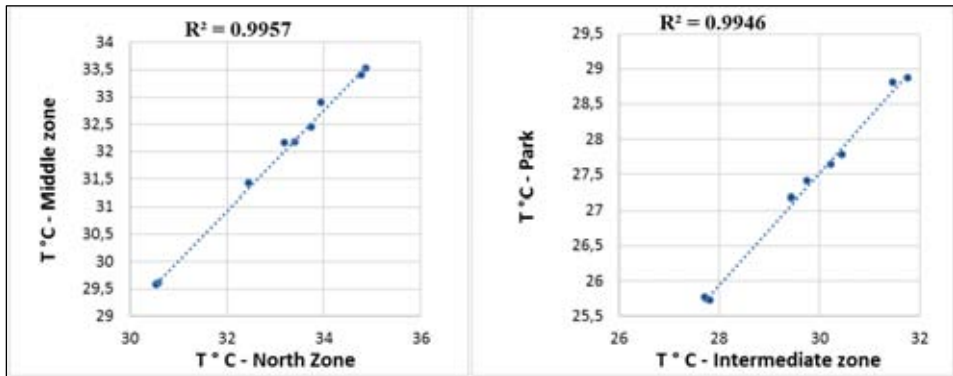


Fig. 20. Correlation between North Zone and Middle Zone (Left) and Park and Intermediate Zone (right)

From recent analyzes, we can assume that the increase in the temperature of the land cover on the data presented does not is due only to the change of the land cover and the increase of the impermeable surfaces at the expense of the vegetation. That is why we analyzed the air temperature trend as well. For the date of acquisition of each image taken in the above analyzes, we took the air temperature to 12 h according to the data provided by NIMH-BAS. For comparison Landsat images were taken around 12:00 h local time. For 2015 only, we took the

value from the wunderground.com website. The following graph, see Fig. 21, shows a comparison of the air temperature and LST dynamics with "Middle Zone" and on Fig. 21 (bottom) shows the intensity of the UHI in Sofia.

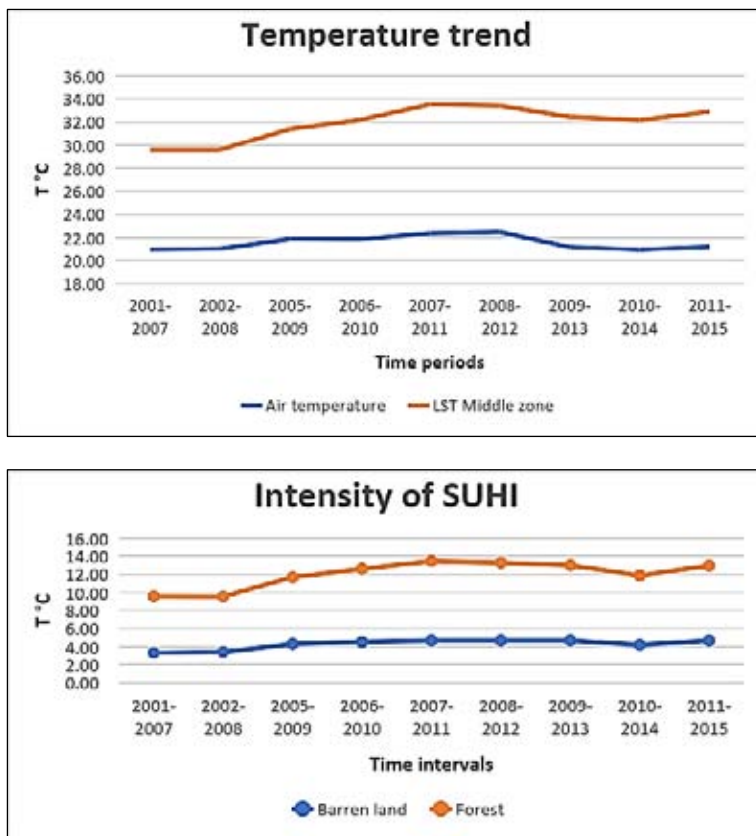


Fig. 21. Comparison of the air temperature at 12:00 h according to NIMH-BAS data and the surface temperature at about 12:00 h according to Landsat data (top). It is seen that the two lines follow a similar trend, as evidenced by the regression analysis. Intensity of the city UHI based on "Barren land" and "Forest" (bottom)

At first glance, the correlation dependence is not satisfactory, Fig. 22. If we analyze the situation more closely, we will see that, if we exclude the three points below the trend line, then the rest form a linear dependence. These separated points themselves appear to lie on one line. These are actually the last three groups.

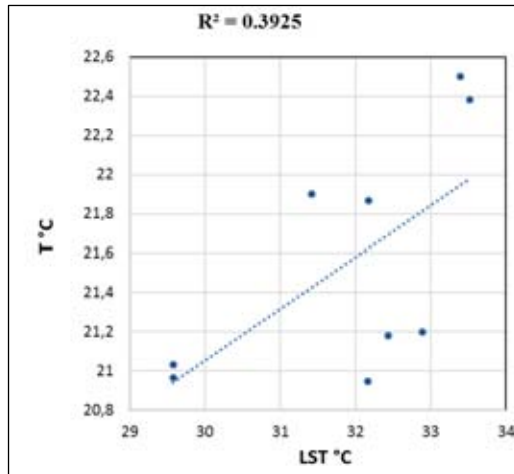


Fig. 22. Correlation between air temperature and land surface temperature

To try to estimate the temperature rise due to the human factor, we also analyze the intensity or magnitude of the the urban heat island. As we quoted earlier, this represents the difference between the warmest zone in the city and the base sub-urban temperature. In the case of base sub-urban temperature we will use two types of surface from the visual classification – "Barren land" and "Forest". As the warmest area of the previous analyzes, Sofia airport was outlined.

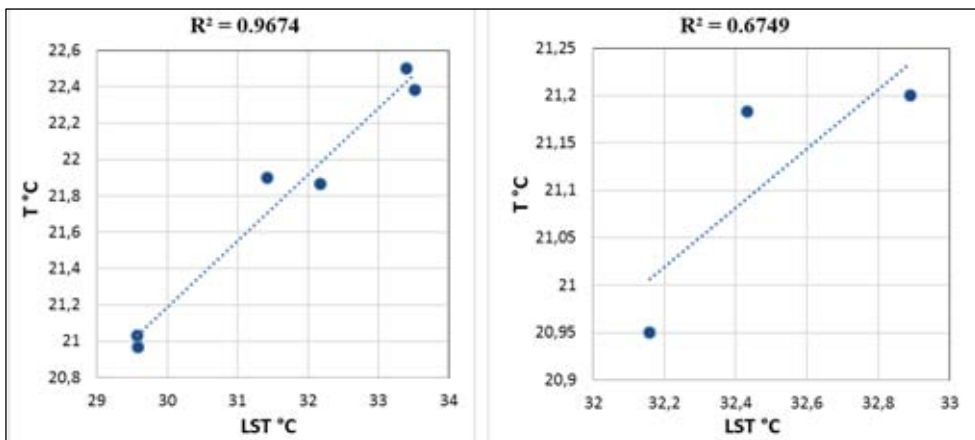


Fig. 23. Correlation between air temperature and LST: the first 6 periods (left) and the last three periods (right)

In average, the intensity of the UHI is around 8 °C. To complete the analysis we will estimate the percentage increase in temperature values using the

highest correlation periods. We will take the first two out of them, as they look rather anomalous in comparison with the others. In total, four periods are from 2005–2009 to 2008–2012. For this seven-year interval, the air temperature in the latter group is 2.74 % higher than the first group. By the same method, the thermal island intensity is higher at the end of the period by 8.79 % calculated on the "Barren land" class, 13.41 % calculated on the "Forest" class or 12.16 % higher on average.

Table 2. Air T° and LST in the "Middle Zone"

Time Period	Air temperature – T °C	LST Middle zone
2001–2007	20.97	29.58
2002–2008	21.03	29.57
2005–2009	21.90	31.42
2006–2010	21.87	32.17
2007–2011	22.38	33.52
2008–2012	22.50	33.40
2009–2013	21.18	32.43
2010–2014	20.95	32.16
2011–2015	21.20	32.89

Table 3. Intensity of the city UHI based on "Barren land" and "Forest" classes

Period	Intensity of UHI – T °C		
	Barren land	Forest	Average
2001–2007	3.31	9.58	6.44
2002–2008	3.41	9.56	6.48
2005–2009	4.31	11.68	8.00
2006–2010	4.54	12.57	8.56
2007–2011	4.70	13.43	9.07
2008–2012	4.69	13.25	8.97
2009–2013	4.71	12.97	8.84
2010–2014	4.22	11.86	8.04
2011–2015	4.68	12.94	8.81

If we subtract the microclimatic influence of the air temperature from the average we will get a 9.42 % increase in the urban surface temperature in the urban area for the period 2005–2012. This should be the rise in temperature due to the withdrawal of parts of construction parks, the emergence of new areas with built-

up blocks of flats, the emergence of new large industrial sites, the collapse of the housing stock, the replacement of old low-rise buildings with new larger buildings are likely to be affected by many other anthropogenic factors accompanying the undeniable growth of the city, such as the increase in road traffic, for example. At the same time, in the analysis of the changes in the land cover in the town we have found an insignificant number of areas with a decrease in temperature, which further supports the fact that the dynamics of the city's temperature is in the direction of constant increase.

Conclusion

Conclusion for the analysis of the processed images we can categorically confirm the formation of a city urban heat island on the surface of the studied territory. This fact is supported by both a visual evaluation and a subsequent in-depth analysis of the results. Two methods of averaging images are used. In "Method 1," we have three equal intervals, which include all the available images in the database evaluated as valid for inclusion in the analysis, while in "Method 2" we have 9 intervals based on selected images (one per year) with similar acquisition conditions.

The model of the UHI shows a marked increase in temperatures from South to North. The temperature profile shows a different manifestation in the West-East direction to the South-North direction. In general, the thermal island is characterized by heterogeneity, as well as the typical UHI cliffs, plateaus, microUHI and "cold" islands.

The influence of the type of land cover has been analyzed. For this purpose, a visual classification has been drawn up, whereby the surveyed territory is divided into 16 classes. Undoubtedly the influence of the so-called "Impervious surfaces" is on the rise in city temperature. A detailed analysis of the data over the entire survey period shows a gradual rise in the city's temperature due to the change in the urban environment. In average, the intensity of the UHI of Sofia is around 8 °C.

References

1. Rao, P.K. Remote sensing of urban "heat islands" from an environmental satellite. *Bulletin of the American meteorological society*, 1972, 53, 7, 647–48.
2. Gallo, K.P. et al. The Use of NOAA AVHRR Data for Assessment of the Urban Heat Island Effect, *Journal of Applied Meteorology*, 1993, 899–908. DOI: 10.1175/1520-0450(1993)032<0899:TUONAD>2.0.CO;2.
3. Carlson, T.N., J.A., Augustine, and F.E. Boland, Potential application of satellite temperature measurements in the analysis of land use over urban areas. *Bulletin of the American Meteorological Society*, 1977, 1301–03.
4. Matson, M., E.P., McClain, Jr, D.F., McGinnis and J.A. Pritchard, Satellite detection of urban heat islands. *Monthly Weather Review*, 1978, 106, 12, 1725–34.

5. Price, J.C. Assessment of the urban heat island effect through the use of satellite data. *Monthly Weather Review*, 1979, 107, 11, 1554–57.
6. Kidder, S.Q., and H.T. Wu, A multispectral study of the St. Louis area under snow-covered conditions using NOAA-7 AVHRR data. *Remote Sensing of Environment*, 1987, 22, 2, 159–72.
7. Roth, M., T.R., Oke, and W.J. Emery, Satellite-derived urban heat islands from three coastal cities and the utilization of such data in urban climatology. *International Journal of Remote Sensing*, 1989, 10, 11, 1699–1720.
8. Carnahan, W.H., and R.C. Larson, An analysis of an urban heat sink. *Remote sensing of Environment*, 1990, 33, 1, 65–71.
9. Leak, S.M., and G. Venugopal, Thematic Mapper thermal infrared data in discriminating selected urban features. *Int. J. Rem. Sens.*, 1990, 11, 5, 841–57.
10. Watanabe, H., H., Yoda, and T. Ojima, Urban environmental design of land use in Tokyo metropolitan area. *Energy and Buildings*, 1990, 15, 1–2, 133–37.
11. Gastelois, B.C., E.S., de Assis, M., Ar, & I.L. Gastelois-UFMG, Environmental climatic conditions in Belo Horizonte: an urban heat island investigated by remoted sensing, 1991.
12. Saito, I., O., Ishihara, and Katayama, T. Study of the effect of green areas on the thermal environment in an urban area. *Energy and Build.*, 1990, 15, 3–4, 493–98.
13. Quattrochi, D.A., and M.K. Ridd, Measurement and analysis of thermal energy responses from discrete urban surfaces using remote sensing data. *International Journal of Remote Sensing*, 1994, 15, 10, 1991–2022.
14. Aniello, C., K., Morgan, A., Busbey, and L. Newland, Mapping micro-urban heat islands using Landsat TM and a GIS. *Comput. & Geosci.*, 1995, 21, 8, 965–969.
15. EUROSTAT – City Statistics Illustrated, 2015. URL: <http://ec.europa.eu/eurostat/cache/RSI/#?vis=city.statistics> (21 December 2016).
16. Climate guide of People’s Republic of Bulgaria. Vol. 3: Air temperature, soil temperature, frost. Sofia, Bulgaria, 1983. (in Bulgarian)
17. National Statistical Institute (NSI). Population by districts, municipalities, settlements and age to 01.02.2011. <http://goo.gl/UXt2pf> (22 December 2017).
18. Jimenez-Munoz, J.-C. and J.A. Sobrino, Split-Window Coefficients for Land Surface Temperature Retrieval From Low-Resolution Thermal Infrared Sensors, *IEEE Geoscience and Remote Sensing Letters*, 2008, 5, 4, 806–09. DOI: 10.1109/LGRS.2008.2001636.

ОЦЕНКА НА ДИНАМИКАТА НА ТЕМПЕРАТУРАТА НА ЗЕМНАТА ПОВЪРХНОСТ НА ГРАД СОФИЯ С ИЗПОЛЗВАНЕ НА СПЪТНИКОВИ ДАННИ ОТ ЛАНДСАТ

Ив. Янев, Л. Филчев

Резюме

Статията представя първи опит за анализ на градския топлинен остров на град София, използвайки спътникови данни. За тази цел са използвани топлинните данни от сензорите ETM+ и TIRS на борда на Landsat. Направен е статистически анализ на резултатите, както и анализ на промените в температурата на повърхността за избрания времеви интервал на изследването – от 2000 до 2015 г. Анализирано е влиянието на вида земно покритие. За тази цел е съставена визуална класификация на земното покритие, при която анализираната територия е разделена на 16 класа. Подробният анализ на данните през целия период на проучването показва постепенно покачване на температурата в града поради промените в градската среда. Едно от заключенията на изследването е, че топлинните изображения могат успешно да се използват за откриване на промените в земното покритие посредством мултitemпорален анализ.

REVIEW OF SPECTRAL VEGETATION INDICES AND METHODS FOR ESTIMATION OF CROP BIOPHYSICAL VARIABLES

Ilina Kamenova, Lachezar Filchev, Iliana Ilieva

*Space Research and Technology Institute – Bulgarian Academy of Sciences
e-mail: ilina.kamenova@hotmail.com, lachezarhf@space.bas.bg*

Abstract

In present article a brief overview is presented on spectral vegetation indices and methods for estimation of crop main biophysical variables and their proxies. The main VIs used in estimation of nitrogen and chlorophyll, biomass, LAI and fAPAR, fCover, and photosynthesis are summarized.

Biophysical variables and vegetation indices

A number of techniques have evolved to derive the biophysical variables of vegetation using remote sensing data; these can be grouped into three broad categories: the inversion of radiative transfer models [39], machine learning (for example neural networks) [4] and the use of vegetation Indices. There are generally few ways of deriving the biophysical estimates using empirical or semi-empirical relationships: 1) single regression; 2) stepwise linear regression; 3) partial least squares (PLS) regression; 4) artificial neural networks [12]. Methods based on vegetation indices (VIs) have the benefit of being computationally simple while they are generally less site specific and more universally applicable than the other methods. The performance of the different indices and selected "optimal" wavebands depends on vegetation and land cover type, the variables to be retrieved, sun/view geometry to name but a few [12]. Satellite spectral data has the potential to measure the reflected radiation from many plants, thus making assessment of biophysical variables feasible on canopy level. The regression models relate *in situ* measurements and VIs. The VIs are mathematical transformations of the original spectral reflectance that are designed to reduce the additive and multiplicative errors associated with atmospheric effects, solar illumination, soil background effects, and sensor viewing geometry [29].

Nitrogen and chlorophyll estimation

Nitrogen is of particular interest in ecological and agricultural studies, because nitrogen availability can affect the rate of key ecosystem processes, including primary production [43]. Nitrogen has traditionally been considered one of the most important nutrients. It is an essential component of the proteins that build cell material and plant tissues. In addition, it is necessary for the function of other essential biochemical agents, including chlorophylls A and B; chloroplast enzymes of the Calvin cycle which are dominated by ribulose-1,5-bisphosphate carboxylase oxygenase (RuBisCO); high energetic compounds such as ATP and NADPH [15]; and the nucleic acids DNA and RNA. Nitrogen is often the most important determinant of plant growths and crop yield.

The productivity and dynamics of unmanaged terrestrial, most agricultural and forestry ecosystems are limited by the supply of biologically available nitrogen [43]. Although an artificial supply of nitrogen to crops is fundamental to optimize crop yields, mismanagement of N and its excessive application, causes many negative effects which have dramatically altered the global nitrogen cycle [32]. The effect of anthropogenic activities on the N cycle has been addressed to some extent. Europe has had some success using rules and fines to modify the fertilizer and animal farm waste. Educational programs need to be further developed to modify human behavior including the way farmers manage N fertilizers in their farms [42]. This challenge requires knowledge about the crop status.

On the other hand, chlorophyll content can directly determine the photosynthetic potential and primary production [16]. Chlorophylls can give an indirect estimation of the nutrient status, because part of the leaf nitrogen is incorporated in chlorophyll. Despite the relatively low N content of chlorophyll (4 mol /mol-1), strong correlations are found between chlorophylls and nitrogen in green leaves, because of the large amount of protein that complexes the photosynthetic pigment [15]. Furthermore, leaf chlorophyll content is indicative for health status evaluation and is closely related to plant stress [33].

Vegetation indices for chlorophyll and nitrogen estimation

A large number of spectral indices have been developed to measure chlorophyll content and nitrogen content. They were considered as a good estimator of these properties. The two variables are highly correlated; thus, they will be accessed with the same set of VIs. Still there are indices which better correlate with nitrogen and as well indices that better correlate with chlorophyll concentrations. The chlorophyll indices are utilizing the bands in the red-edge position which was proved by previous research [6–10, 28] to be particularly suitable for chlorophyll estimation. Because of the strong correlation between chlorophyll and nitrogen these indices are suitable for nitrogen as well.

The SWIR bands are often mentioned in scientific literature as sensitive directly to nitrogen concentration. One of the Sentinel-2 main improvements over sensors as for instance Landsat TM, SPOT etc., are the bands centered on the Red Edge position. There are two Red Edge bands which are centered at 705 nm and 740 nm with band width of 15 nm. These wavelengths are essential for estimating biochemical quantities [9]. Most of the indices mentioned in the literature are developed initially as hyperspectral indices and cannot be calculated with the exact wavelengths as mentioned in the literature, as they require very specific bands, most of the cases not available by the Sentinel-2 MSI sensor bands. However, approximately close wavebands could be used to calculate indices.

Numerous VIs have been proposed for estimating canopy chlorophyll or nitrogen content [7]. Specifically, the red-edge region has been often used for estimating chlorophyll and nitrogen content. Vegetation indices often combine a near-infrared spectral band, representing scattering of radiation by a canopy, with a visible spectral band, representing absorption by chlorophyll. Problem with using the red spectral bands is the strong absorption by chlorophyll resulting into less sensitivity of such indices. Due to lower absorption by chlorophyll in the red-edge region, the use of such a band reduces the saturation effect, and the reflectance still remains sensitive to chlorophyll absorption at its moderate-to-high values [20]. For detecting plant stress the position of the red-edge inflection point is of very high significance [28]. The red-edge position has often been used as an estimate for chlorophyll content. With the number of red-edge bands of Sentinel-2 bands, the red-edge position can be derived by applying a simple linear model to the red-infrared slope [23].

Another type of index based on the MERIS red-edge bands is the MERIS terrestrial chlorophyll index, MTCI [9, 10]. This index has been applied successfully for many applications. It has been shown in various studies that ratio indices and/or normalized difference indices using red-edge bands perform very well in estimating chlorophyll or nitrogen content. Authors such as A. Gitelson [22] presented a ratio index based on a NIR band (e.g., at 800 nm) and a red-edge band (e.g., at 710 nm) for estimating chlorophyll content: the so-called red-edge chlorophyll index

($CI_{red-edge} = R_{800}/R_{710} - 1$). Similarly, a so-called green chlorophyll index ($CI_{green} = R_{800}/R_{550} - 1$) has been proposed. Major advantages are their linearity with chlorophyll content and absence of the saturation effect. In literature, various ratio indices can be found with slightly different band settings, often depending on the available sensor. The indices most often mentioned in the literature with significant results and suitable for calculation on Sentinel-2 bands are listed in Table 1.

Table 1. Vegetation indices for chlorophyll and nitrogen estimation, suitable for calculation with Sentinel-2 bands

Index	Formulae	References
REP	$((R_{670} + R_{780})/2 - R_{700}) / (R_{740} - R_{700}) * 40 + R_{700}$	[6, 7, 23, 44, 45]
MTCI	$(R_{754} - R_{709}) / (R_{709} - R_{681})$	[6, 7, 9, 10, 44]
CI red edge	$(R_{780}/R_{709}) - 1$	[6, 14, 18, 22, 44]
CI green	$(R_{780}/R_{550}) - 1$	[6, 7, 20]
NDRE	$(R_{740} - R_{705}) / (R_{740} + R_{705})$	[20, 41]
NDRE1	$(R_{780} - R_{705}) / (R_{780} + R_{705})$	[20, 41]
CCCI	$((R_{790} - R_{720}) / (R_{790} + R_{720})) / ((R_{800} - R_{670}) / (R_{800} + R_{670}))$	[2]

Biomass estimation

Measurement of various crop canopy variables during the growing season provides an opportunity for improving grain yields and quality by site-specific application of fertilizers and pesticides. Important variables in this context are the leaf area and total aboveground biomass because they are clear indicator of vegetation development and health [14, 31, 36, and 38]. The biophysical and biochemical parameters of plants are at the focus of many applications based on remote sensing techniques. Maps of those parameters are of particular interest to assist in the decision-making process in the context of agriculture. The biomass is one of the most important biophysical surface parameter attracting interest in wider researches concerned with earth observation data. The remote sensing techniques could provide repeated measures from a field without destructive sampling of the crop, which can provide valuable information for agricultural activities [27]. The repeated and consistent measurements result in the availability of time series data for a longer period of time. The availability of time series data for longer periods from different sensors helps the modern farmer to get current view on how a parcel performs over the growing season.

Spectral VIs derived from spectral reflectance have been shown to be useful for indirectly obtaining crop information such as biomass, photosynthetic efficiency, productivity potential, leaf chlorophyll content and N concentration [40]. Recent studies by [5, 11] have demonstrated the usefulness of optical indices from remote sensing in the assessment of vegetation biophysical and biochemical variables, including above ground biomass. In order to investigate the physical and biochemical parameters of a crop should be used VIs which are sensitive to the target characteristics of the crop parameters. Big challenge is also to evaluate the seasonal patterns of the VI and to determine which VIs are the most robust for detecting the biomass of the crop within a field over the growing season.

Vegetation indices for biomass estimation

Remote sensing data and techniques have already proven to be used as a relevant tool for crop inventory and monitoring purposes [24, 25]. Among the different issues, determining the crop status, condition and biomass are some of the important issues in which remote sensing applications have been used [27]. Besides, crop parameters, such as leaf area index (LAI), leaf chlorophyll content, leaf water content, and canopy cover have been successfully measured using remote sensing technology, especially using spectral VIs [25, 26, and 29].

The simple ratio (SR) and the superior normalized difference vegetation index (NDVI), both calculated from measurements of the reflected light from the red and near infrared bands, have long been used as indirect measurement of biomass and crop yield, including that of wheat [14, 26, 27, and 38]. NDVI combining a near-infrared spectral band, representing scattering of radiation by a canopy, with a red spectral band, representing absorption by chlorophyll, saturates with higher LAI. This problem occurs because the red spectral band has very strong absorption by chlorophyll and that results into less sensitivity after certain value of LAI of such indices. Due to lower absorption by chlorophyll in the red-edge region, the use of such a band reduces the saturation effect, and the reflectance still remains sensitive to chlorophyll absorption at its moderate-to-high values. Therefore, the red edge inflection point [18] and several NIR/NIR indices have been proven to offer more reliable signals in high biomass-producing areas like Europe. However, some indices concentrate on the visible range of the reflection spectrum. Because they are primarily influenced by the absorbance capacity of chlorophyll, VIS-based indices are presumed to identify green vegetation over soil, [17, 34].

NDVI have during the past decades been based on either broad wavebands (50–100 nm scale) from, e.g. the satellite-based Landsat Thematic Mapper using the TM-spectrometer (TM), or short wavebands (10 nm scale) from field-based spectroradiometers like FieldSpec (ASD Inc, PANalytical), CropScan MSR87 and MSR16 (CropScan, USA). The broadband VIs use, in principle, average spectral information over a wide range resulting in loss of critical spectral information available in specific narrow bands. To bridge that gap ESA's upcoming satellite Sentinel-2 (S2) aims to replace and improve the old generation of high resolution satellite sensors Landsat and SPOT, but with improved spectral capabilities. Of specific interest for remote sensing applications for agriculture monitoring are two new bands in the red edge (B5 at 705 nm and B6 at 740 nm) [11]. The indices most often mentioned in the literature with significant results and suitable for calculation on Sentinel-2 bands are listed in Table 2.

Table 2. VIs for biomass estimation, suitable for calculation with Sentinel-2 bands

Index	Formulae	References
NDVI	$(R_{780} - R_{670}) / (R_{780} + R_{670})$	[26, 37, 38]
NDVI1	$(R_{740} - R_{705}) / (R_{740} + R_{705})$	[26]
NDVI2	$(R_{780} - R_{705}) / (R_{780} + R_{705})$	[26]
SR	R_{740} / R_{665}	[14]
	R_{783} / R_{665}	
	R_{783} / R_{740}	
	R_{783} / R_{705}	
	R_{945} / R_{865}	
REP	$700 + 40 * ((R_{670} + R_{780}) / 2 - R_{700}) / (R_{740} - R_{700})$	[6, 7, 23, 44, 45]
VARI	$(R_{550} - R_{650}) / (R_{550} + R_{650} - R_{470})$	[14]

LAI and fAPAR estimation

With the advancement of RS technologies more scientific teams has started exploring satellite data to derive biophysical estimates for cereals and more specifically – winter wheat. Although many scientists have tried to transform their VIs in such a way that a linear relationship can be established between VI and the variable of interest, an exponential function still appears to be the best approximation [12]. The classical broadband vegetation indices typically use a spectral band in the red and one in the NIR. As both red and NIR reflectance saturate when LAI increases, the VIs become insensitive for dense canopies [25].

The Normalised Difference Vegetation Index (NDVI) [36] which is currently the most widely used VI as a measure for many variables. Although VIs such as the NDVI were primarily developed for the purpose of LAI retrieval they have also been argued to be capable of canopy chlorophyll content estimations [30]. Some authors have focused their efforts to linearize the relationship between the VIs in question and LAI [13]. On test-fields of winter wheat and rapeseed the DSIR760–R739 appeared to be the best estimate of LAI above 1.5 in terms of sensitivity compared to few other VIs.

Fraction of vegetation cover (fCover) estimation

Fraction of vegetation cover (fCover), or the percentage of soil surface covered by plant foliage (usually assessed vertically), is an important measurement of crop establishment and early vigor [35]. This variable can be related with the interception of solar radiation from crop canopies and thus with their production potential. Some times in the agronomic practice vegetation fraction as assessment from different view angle may be of interest. For example [3] suggest that an estimation of solar radiation interception at a 45° view is more appropriate because

it better represents an average sun angle. For wheat, however, the percent interception of total radiation changes little with time of day (sun angle) [3].

Typical approaches to measure fCover in the field are point quadrat techniques, visual assessment and digital analysis of photographs. These methods however do not have sufficient resolution or are laborious and time consuming. Thus, remote estimation through spectral vegetation indices is useful alternative. NDVI has long been regarded as a measure of the quantity of green vegetation covering the soil. [21] showed that NDVI is insensitive of fCover change in wheat when fCover > 60 %. Based on simulated MODIS bands these authors propose a simple index for estimation of wheat fCover – the Vegetation Index green (VI green). The relationship of this index with fCover is linear and $r^2 > 0.91$. Even better results are achieved with Visible Atmospherically Resistant Index green (VARI green) where blue band is used to reduce atmospheric effects. Modifications of NDVI have also been proposed. For example Wide Dynamic Range Vegetation Index (WDRVI) [19] outperforms VARI green in maize and soybean crops. Vegetation indices incorporating correction for soil reflectance also proved to be useful for wheat fCover estimation.

Table 3. Vegetation indices for chlorophyll and nitrogen estimation, suitable for calculation with Sentinel-2 bands

Index	Formulae	References
Red edge NDVI	$(R_{NIR} - R_{red\ edge}) / (R_{NIR} + R_{red\ edge})$	[19]
WDRVI	$(0.3 * R_{NIR} - R_{red}) / (0.3 * R_{NIR} + R_{red})$	[19]
VARI green	$(R_{green} - R_{red}) / (R_{green} + R_{red} - R_{blue})$	[21]
VI green	$(R_{green} - R_{red}) / (R_{green} + R_{red})$	[21]

Photosynthesis estimates

Photosynthesis is the most important process in plants, but its measurement by gas exchange method (most accurate for now) is time consuming and requires specialized equipment. Vegetation products derived from terrestrial, airborne or satellite data for reflective characteristics of plants are more often used in agricultural practices to assess plant status and take the appropriate cultivation action.

The Photochemical Reflectance Index (PRI) (Table 4), calculated as $(R_{531} - R_{570}) / (R_{531} + R_{570})$ measures the activity of the xanthophyll cycle in plants – a process competitive of the electron transport in Photosystem II and thus closely correlated to the photosynthesis.

Articles that reported relationships between remotely sensed PRI and the following plant physiological variables – Light Use Efficiency (LUE) / Radiation Use Efficiency (RUE), CO₂ uptake (Photosynthesis), actual photochemical

efficiency of Photosystem II – $\Phi\text{PSII} = \Delta\text{F}/\text{Fm}'$ and Non photochemical quenching (NPQ) were reviewed. For each article we registered the main features of the study, and also the correlation coefficient (Pearson's r) and the coefficient of determination (R^2) as indicators of the strength of each presented relationship.

Plants were grown at fields or in greenhouses and were exposed to different stresses (water deficit, nitrogen deficiency, cadmium pollution, etc.). Observations were organized on diurnal or through the whole vegetation cycle bases. Measurements were made on different plant organization levels—leaf, canopy or ecosystem ("canopy" refers to either a single plant or a monospecific stand, and "ecosystem" refers to a mixed-species stand). The index PRI isn't suitable for calculation using Sentinel-2 imagery and bands combinations aren't possible. On this stage no modeling of photosynthesis parameters is planned. For future research we see the exploration of those parameters and the vegetation fluorescence as a very promising initiative, especially in line with the Sentinel-3 mission and the development of FLuorescence EXplorer (FLEX) from ESA.

Table 4. Vegetation indices for photosynthesis parameters estimation, suitable for calculation with Sentinel-2 bands

Index	Formulae	References
PRI	$(R_{531} - R_{570}) / (R_{531} + R_{570})$	wheat (Magney et al., 2014); barley (Filella et al., 1996 and Sun et al., 2013); rice (Inoue et al., 2008); maize (Cheng et al., 2013, Panigada et al., 2014, Rossini et al., 2013, Rossini et al., 2015); soybean (Inamullah and Isoda, 2005, Xue et al., 2014); sunflower (Magney et al., 2014, Peñuelas et al., 1994); grass (Rossini et al., 2012) and different species including herbaceous annuals, deciduous perennials and evergreen perennials (Gamon et al., 1997)

Acknowledgements

Present study is implemented within contract *Testing Sentinel-2 vegetation indices for the assessment of the state of winter crops in Bulgaria* (TS2AgroBg). The Project is funded by the Government of Bulgaria through an ESA Contract (4000117474/16/NL/NDe) under the PECS (Plan for European Cooperating States). The view expressed herein can in no way be taken to reflect the official opinion of the European Space Agency.

References

1. Aschbacher, J., and M. P. Milagro-Pérez. The European Earth Monitoring (GMES) Programme: Status and Perspectives. 2012, 120, 3–8.

2. Barnes, E. M., et al. Coincident detection of crop water stress, nitrogen status and canopy density using ground based multispectral data. Proceedings of the 5th Inter. Conf. on Precision Agri., Bloomington, MN, USA. 2000, 1619.
3. Bell, M. A., and R. A. Fischer, Using yield prediction models to assess yield gains: A case study for wheat. *Field Crops Research*, 1994, 36, 2, 161–66.
4. Carpenter, G. A., et al. A neural network method for efficient vegetation mapping." *Remote Sensing of Environment*, 1999, 70, 3, 326–338.
5. Chen, P. et al. New Spectral Indicator Assessing the Efficiency of Crop Nitrogen Treatment in Corn and Wheat. *Rem. Sens. of Env.*, 2010, 114, 9, 1987–97.
6. Clevers, J. G. P. W., and A. A. Gitelson. Remote Estimation of Crop and Grass Chlorophyll and Nitrogen Content Using Red-Edge Bands on Sentinel-2 and -3. *Inter. J Applied Earth Observation and Geoinformation*, 2013, 23, 344–51.
7. Clevers, J. G.P.W., and L. Kooistra. Using Hyperspectral Remote Sensing Data for Retrieving Canopy Chlorophyll and Nitrogen Content, 2012, 5, 2, 574–83.
8. Curran, P. J., W. R. Windham, and H.L. Gholz, Exploring the Relationship between Reflectance Red Edge and Chlorophyll Concentration in Slash Pine Leaves. *Tree physiology*, 1995, 15, 3, 203–6.
9. Dash, J., and P. J. Curran, The MERIS Terrestrial Chlorophyll Index. *Int. J. Rem. Sens.*, 2004, 25, 23, 5403–13. DOI: 10.1080/0143116042000274015
10. Dash, J., and P.J. Curran, Evaluation of the MERIS Terrestrial Chlorophyll Index (MTCI). *Advances in Space Research*, 2007, 39, 1, 100–04.
11. Delegido, J., J. Verrelst, L. Alonso, and J. Moreno. Evaluation of Sentinel-2 Red-Edge Bands for Empirical Estimation of Green LAI and Chlorophyll Content. *Sensors*, 2011, 11, 7, 7063–81.
12. Dorigo, W. A. et al. A Review on Reflective Remote Sensing and Data Assimilation Techniques for Enhanced Agroecosystem Modeling. *International Journal of Applied Earth Observation and Geoinformation*, 2007, 9, 2, 165–93.
13. Elvidge, C. D., and Chen, Z. Comparison of broad-band and narrow-band red and near-infrared vegetation indices. *Rem. sens. of envir.*, 1995, 54, 1, 38–48.
14. Erdle, K., B. Mistele, and U. Schmidhalter, Comparison of Active and Passive Spectral Sensors in Discriminating Biomass Parameters and Nitrogen Status in Wheat Cultivars. *Field Crops Research*, 2011, 124, 1, 74–84. DOI: 10.1016/j.fcr.2011.06.007
15. Evans, J. R. Photosynthesis and Nitrogen Relationships in Leaves of C3 Plants. *Oecologia*, 1989, 78, 1, 9–19. DOI: 10.1007/BF00377192
16. Filella, I., L. Serrano, J. Serra, and J. Peñuelas. Evaluating Wheat Nitrogen Status with Canopy Reflectance Indices and Discriminant Analysis. *Crop Science*, 1995, 35, 5, 1400.
17. Gamon, JAm, L. Serrano, and J. S. Surfus. The photochemical reflectance index: an optical indicator of photosynthetic radiation use efficiency across species, functional types, and nutrient levels. *Oecologia*, 1997, 112, 4, 1997, 492–501.
18. Gitelson, A. A. et al. Remote Estimation of Canopy Chlorophyll Content in Crops. *Geophysical Research Letters*, 2005, 32, 8, 1–4. DOI: 10.1029/2005GL022688
19. Gitelson, A. A. Remote estimation of crop fractional vegetation cover: the use of noise equivalent as an indicator of performance of vegetation indices. *International journal of remote sensing*, 2013, 34, 17, 6054–66.

20. Gitelson, A. A., Y. J. Kaufman, and M.N. Merzlyak. Use of a Green Channel in Remote Sensing of Global Vegetation from EOS-MODIS. *Remote Sensing of Environment*, 1996, 58, 3, 289–98.
21. Gitelson, A. A., Y. J., Kaufman, R., Stark, and D. Rundquist, Novel algorithms for remote estimation of vegetation fraction. *Remote sensing of Environment*, 2002, 80, 1, 76–87.
22. Gitelson, A. A., G. P. Keydan, and M.N. Merzlyak. Three-Band Model for Noninvasive Estimation of Chlorophyll, Carotenoids, and Anthocyanin Contents in Higher Plant Leaves. *Geophysical Research Letters*, 2006, 33, 11, L11402. DOI: 10.1029/2006GL026457
23. Guyot, G., and F. Baret. Utilisation de La Haute Resolution Spectrale Pour Suivre L'état Des Couverts Vegetaux. 1988, 287, 279.
24. Haboudane, D. et al. Integrated Narrow-Band Vegetation Indices for Prediction of Crop Chlorophyll Content for Application to Precision Agriculture. *Rem. Sens. of Envir.*, 2002, 81, 2–3, 416–26. DOI: 10.1016/S0034-4257(02)00018-4
25. Haboudane, D. et al. Hyperspectral Vegetation Indices and Novel Algorithms for Predicting Green LAI of Crop Canopies: Modeling and Validation in the Context of Precision Agriculture. *Rem. Sens. of Env.*, 2004, 90, 337–52.
26. Hansen, P. M., and J. K. Schjoerring. 2003. Reflectance Measurement of Canopy Biomass and Nitrogen Satus in Wheat Crops Using Normalized Difference vegetation indices and Partial Least Squares Regression. *Rem. Sens. of Envir.*, 86, 4, 542–53. DOI: 10.1016/S0034-4257(03)00131-7
27. Hatfield, J. L., and J. H. Prueger. 2010. Value of Using Different Vegetative Indices to Quantify Agricultural Crop Characteristics at Different Growth Stages under Varying Management Practices. *2, 2, 562–78.*
28. Horler, D. N. H., M. Dockray, and J. Barber. The Red Edge of Plant Leaf Reflectance. *Int. J. Rem. Sens.*, 1983, 4, 2, 273–88. DOI: 10.1080/01431168308948546
29. Huete, A. et al. Overview of the Radiometric and Biophysical Performance of the MODIS Vegetation Indices. *Rem. Sens. of Envir.*, 2002, 83, 1, 195–213. DOI: 10.1016/S0034-4257(02)00096-2
30. Huete, A. R. A Soil-Adjusted Vegetation Index (SAVI). *Rem. Sens. of Envir.*, 1988, 25, 3, 295–309. DOI: 10.1016/0034-4257(88)90106-X
31. Jamieson, P.D., M.A. Semenov, I.R. Brooking, and G.S. Francis. Sirius: A Mechanistic Model of Wheat Response to Environmental Variation. *Europ. J. Agro.*, 1998, 8, 161–79. DOI: 10.1016/S1161-0301(98)00020-3
32. Keeney, D. R., and J. L. Hatfield. The Nitrogen Cycle, Historical Perspective, and Current and Potential Future Concerns. In Elsevier Inc., 2008, 1–18.
33. Merzlyak, M. N., A. A. Gitelson, O. B. Chivkunova, and V. YU. Rakitin. Non-Destructive Optical Detection of Pigment Changes during Leaf Senescence and Fruit Ripening. *Physiologia Plantarum*, 1999, 106, 1, 135–41. DOI: 10.1034/j.1399-3054.1999.106119.x
34. Peñuelas, J., J. A. Gamon, A. L. Fredeen, J. Merino, & C. B. Field, Reflectance indices associated with physiological changes in nitrogen-and water-limited sunflower leaves. *Rem. sens. of Envir.*, 1994, 48, 2, 135–146.
35. Pask, A. J. D., Pietragalla, J., Mullan, D. M., and M.P. Reynolds, Physiological breeding II: a field guide to wheat phenotyping. 2012, Cimmyt.

36. Pimstein, A. et al. A Spectral Index to Monitor the Head-Emergence of Wheat in Semi-Arid Conditions. *Field Crops Research*, 2009, 111, 3, 218–25.
37. Rouse Jr, J., Haas, R. H., Schell, J. A., and Deering, D. W. (1974). Monitoring vegetation systems in the Great Plains with ERTS.
38. Serrano, L., I. Filella, J. Peñuelas. Remote Sensing of Biomass and Yield of Winter Wheat under Different Nitrogen Supplies. *Crop Sci.*, 2000, 40, 3, 723. DOI: 10.2135/cropsci2000.403723x
39. Shultis, J. K., and R. B. Myneni. Radiative transfer in vegetation canopies with anisotropic scattering. *J Quant. Spectro. and Radiat. Transf.*, 1988, 39, 2, 115–29. DOI: 10.1016/0022-4073(88)90079-9
40. Thenkabail, P. S, R. B. Smith, E. De Pauw, Hyperspectral Vegetation Indices and Their Relationships with Agricultural Crop Characteristics. *Rem. Sens. of Envir.*, 2000, 71, 2, 158–82. DOI: 10.1016/S0034-4257(99)00067-X
41. Tilling, A. K., et al. Remote sensing of nitrogen and water stress in wheat. *Field Crops Res.*, 2007, 104, 1–3, 77–85. DOI: 10.1016/j.fcr.2007.03.023
42. Tilman, D. et al. 2002. Agricultural Sustainability and Intensive Production Practices. *Nature*, 418, 6898, 671–77. DOI: 10.1038/nature01014
43. Vitousek, P. M., and R. W. Howarth. Nitrogen Limitation on Land and in the Sea: How Can It Occur? *Biogeochem*, 1991, 13, 2. DOI: 10.1007/BF00002772
44. Wu, C., et al. Remote estimation of gross primary production in wheat using chlorophyll-related vegetation indices. *Agri. and Forest Meteorol.*, 2009, 149, 6–7, 1015–21. DOI: 10.1016/j.agrformet.2008.12.007
45. Wu, C., et al. Estimating chlorophyll content from hyperspectral vegetation indices: Modeling and validation. *Agricultural and forest meteorology*, 2008, 148, 8–9, 1230–41. DOI: 10.1016/j.agrformet.2008.03.005

ОБЗОР НА ИНДЕКСИТЕ И МЕТОДИТЕ ЗА ИЗСЛЕДВАНЕ НА БИОФИЗИЧНИ ПРОМЕНЛИВИ НА ЗЕМЕДЕЛСКИ КУЛТУРИ

И. Каменова, Л. Филчев, И. Илиева

Резюме

В настоящата статия е представен кратък обзор на вегетационните индекси и методите за оценка на основните биофизични променливи на земеделски култури. Направена е характеристика на основните вегетационни индекси, използвани при оценката на азот и хлорофил, биомаса, листов индекс и fAPAR, fCover и фотосинтеза.

SPACE TECHNOLOGIES FOR STUDYING AND MONITORING OF SEISMOGENIC ZONES

Dimitar Dimitrov

*National Institute of Geophysics, Geodesy and Geography – Bulgarian Academy
of Sciences
e-mail: clgdimi@bas.bg*

Abstract

In the present article are produced the results of studies, carried out by the author or by teams under his direction and participation, in different seismogenic zones in Bulgaria and abroad. The submitted cases of the application of space technologies GNSS and InSAR for investigation and monitoring of seismogenic zones manifest the significance and the advantages of these methods in a determination of the regularities in the development of the tectonic processes of accumulation and release of tensions in the seismogenic zones, related to the assessment of the seismic hazard and medium-term forecast of strong earthquakes.

1. Introduction

The Global Earth Observation System of Systems (GEOSS) and the Copernicus Programme (formerly Global Monitoring for Environment and Security – GMES) have as a priority in the preservation of the environment and the sustainable development of the society – instruments for assessment, as well as methods for monitoring and prognosis.

The seismogenic zones are the region genetically connected to historical and instrumental seismicity, a potential seismic hazard of strong earthquakes and are identified by seismologic, geophysical and geological data. Bulgaria is situated in an active seismogenic zone from which results a main task for the science to study the processes occurring in these zones which lead to strong earthquakes and to undertake appropriate measures for effective counteraction.

This problem is characterized with special topical degree in a national and planetary scale and puts it in the category of the priority research trends in the field of Earth sciences.

The application of space technologies in the Global Navigation Satellite System (GNSS) and the radar Interferometry InSAR (Interferometric Synthetic Aperture Radar) allow to study the seismogenic zones and the physical processes causing the strong earthquakes. The permanent and periodic high precision

measurement with GNSS and the application of the radar interferometry InSAR are the most effective space technics for monitoring and study of seismogenic zones.

Here below are represented the results of the studies carried out during the last 20 years by the author and groups under his guidance or with his participation in different seismogenic zones in Bulgaria and all over the world [12].

2. Monitoring of the seismogenic zone in the region of Sofia city

The region in south of Sofia city is revealed in structure-geomorphologic, tectonic and seismic approach seismogenic zone where could be expected strong earthquakes [1]. This zone is connected to the so-called *Vitosha* fault dividing *Vitosha* morphoblock from the absorbed under neogenic sediments complex broke up Sofia graben. The surface manifestations of *Vitosha* and *Lozen* faults are presented on the remotely-sensed image, by appointed with InSAR method, relatively vertical deformations and the network for GNSS monitoring (Fig. 1).

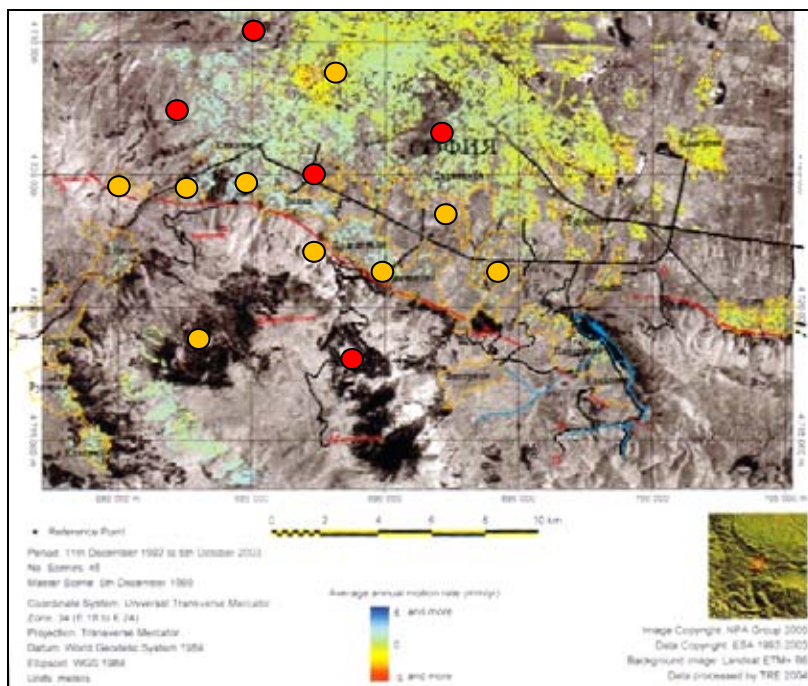


Fig. 1. Network for GNSS monitoring of the Vitosha fault on the remote sensing image and the result of the In SAR study of the zone. The permanent GNSS stations are presented with red and the periodic measurements with orange circles.

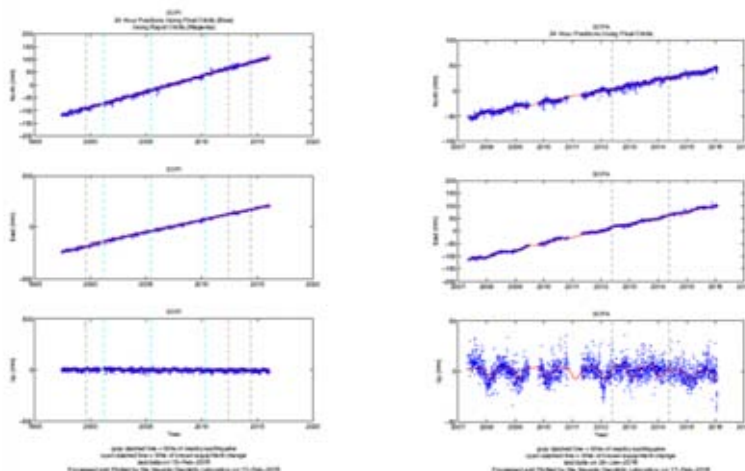


Fig. 2. Components of the absolute velocities from the permanent stations of SOFI and SOFA, on both sides of the Vitosha fault

The obtained from the monitoring identical velocities of displacements of the permanent and periodic measurement GPS stations (Fig. 2) of the order of $1\div 2$ mm/year do not testify for accumulating of considerable tectonic tensions on Vitosha fault. The data from the permanent and periodic re-measurement GPS stations in the regions provide a high-precision monitoring of the movements in this seismogenic zone in connection with the study of tectonic tensions and seismic hazard [2].

3. Studies and monitoring of the seismogenic zone Chirpan–Plovdiv

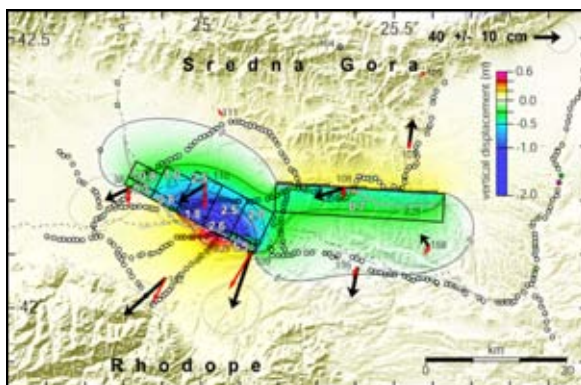


Fig. 3. Main faults activated during the earthquakes on 14 and 18 April 1928, obtained from modeling of the co-seismic displacements determined by data from GNSS measurements (black arrows)

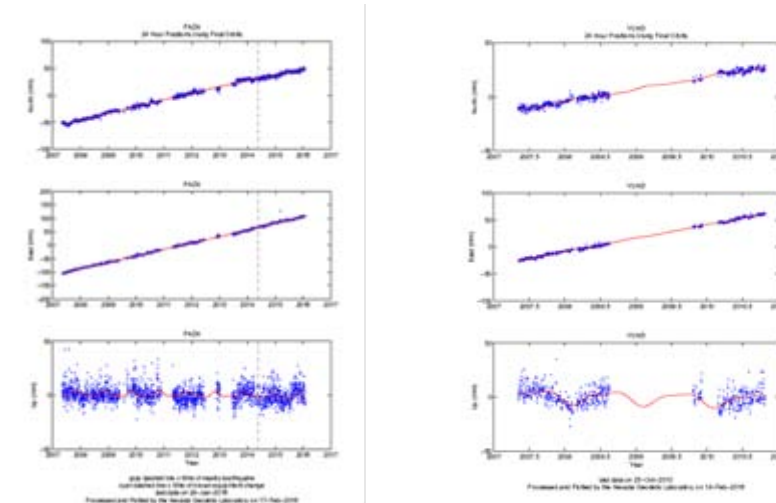


Fig. 4. On the right is a permanent GNSS station in the city of PAZA and YUND the components of its temporary series

The application of the space technology GNSS for assessment of the velocities of shifting of geodetic benchmarks in the region allow to study the zone and to determine the geodetic parameters of the main faults, activated in 1928 [3] (Fig. 3). The monitoring of the zone with periodic GNSS measurements (Fig. 4) provides an assessment of the tectonic tensions and along with paleoseismic studies allows for determination of the seismic cycle of strong earthquakes in the region [4].

4. Studies and monitoring of the seismic zone of South-West Bulgaria

The region of South-West Bulgaria is known with one of the strongest earthquakes which struck Europe on 4 April 1904 with magnitude (M) 7.3 and 7.8 [1].

The continuous monitoring of the zone with permanent GNSS stations and periodic measurements of the local geodynamic network around *Krupnik* fault allow to assess the regional tectonic movements and local tensions around *Krupnik* fault (Fig.5). According to the data obtained and together with the results from the paleoseimologic studies was determined the seismic cycle of the *Krupnik* fault [5].

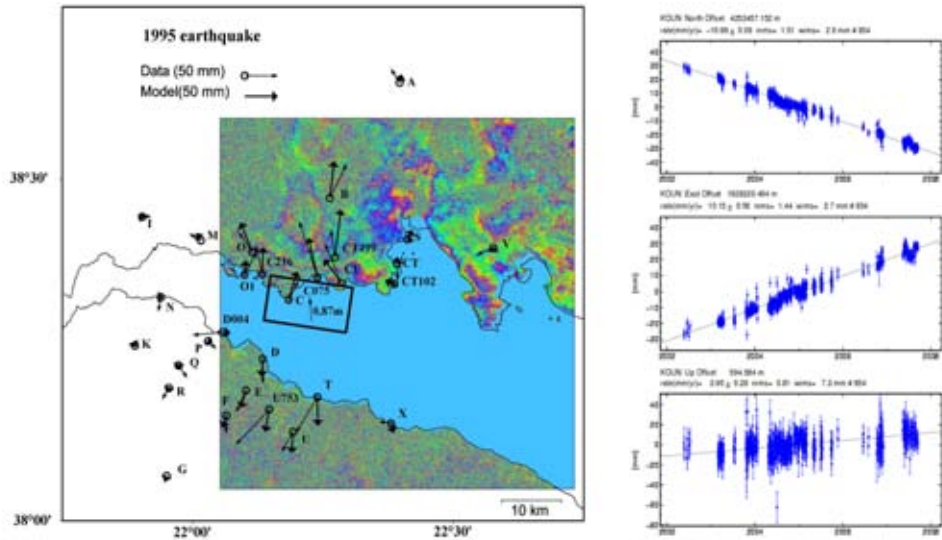


Fig. 6. The region of the earthquake on 15.06.1995 with determined co-seismic deformations by GNSS and InSAR methods. The assessed and modelled displacements are presented respectively by thin and thick arrows. On the right is presented a comparison between permanent stations on the two coasts of Corinth Bay. The space vectors between the stations on the two coasts of the bay has been struck.

5.2. In the study of the earthquake on 26.07.1996 in Konitsa $M=5.3$ in Northern Greece was confirmed the possibilities of the method InSAR for the study of the physical mechanisms of medium-strong earthquakes with (Fig. 7).

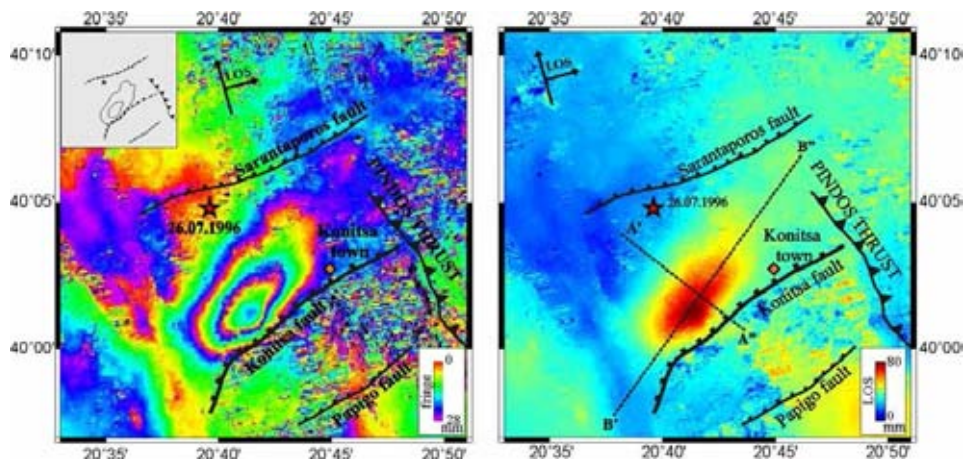


Fig. 7. Seismogenic zone of town of Konitsa with the assessed by the method InSAR co-seismic deformations of the earthquake in 1996 and the faults activated

5.3. The study of the earthquake of 2003 in *Lefkada* M=6.3 by InSAR method and modeling of co-seismic deformations (Fig. 8) shows the possibilities of this method for assessment of the place and the seismotectonic parameters of the activated sea faults [6].

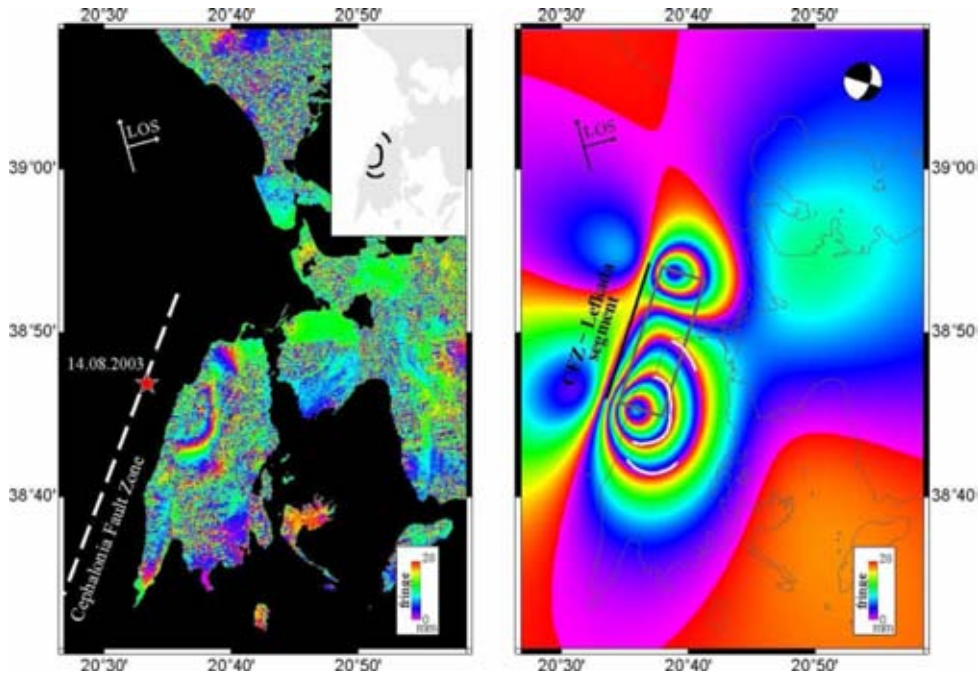


Fig. 8. Isle Lefkada with the assessed by the method InSAR coseismic deformations and the fault, activated during the shock of 2003. On the right – the model of coseismic deformations.

6. Study of the zone of the earthquake of 1835 in Central Chile

The seashore line of Chile is one of the most seismogenic zones in the world. Here approximately at every ten years occur strong earthquakes with magnitude $M > 8$. The region is situated between 35° and 37° S and is known with a very strong earthquake of February 1835 [7] with $M=8,5$ [8] (Fig. 9).

In this region was stabilized and assessed in 1996, 1999 and 2002, with a GNSS network of 41 observation points, which allow considerable displacements of monitoring stations reflected by the accumulation of the inter-seismic tensions caused by plate subduction.

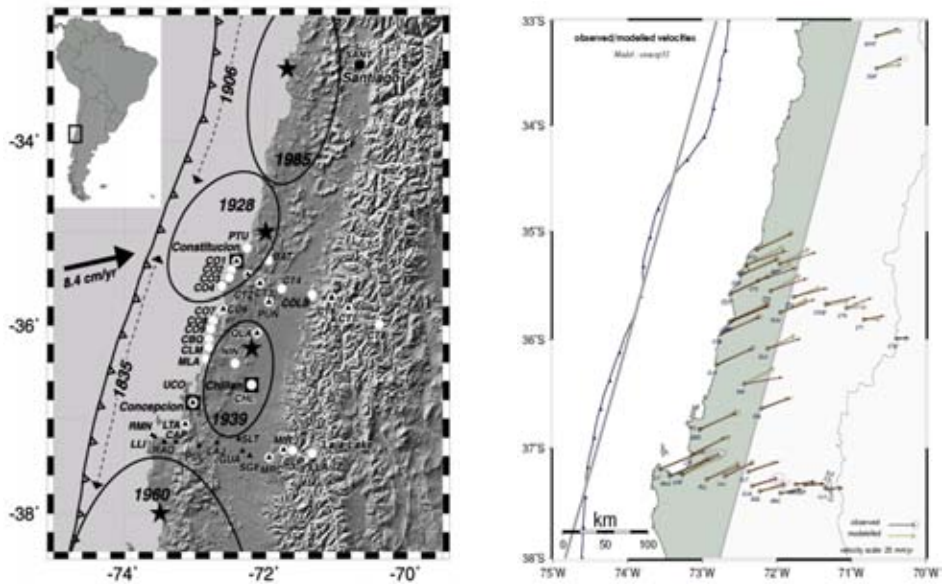


Fig. 9. Geodynamic GNSS network of 41 observation points in the seismogenic zone of central Chile with the results of monitoring 1996, 1999 and 2002. On the right (in greyscale) – the zone of collision of the Pacific Nazca Plate with this of South America –obtained from the modeling of interseismic displacements.

The analysis of the results from three cycles of measurements determines considerable inter-seismic movements with velocity from 34 to 45 mm/year on coastline and from 10 to 20 mm/year on the mountain range of Andes in comparison with the stable part of the South American continental Plate (Fig. 9). Namely, the considerable difference between velocities of movement of the benchmarks stabilized on the coastline and those on the mighty mountain range of Andes is the reason for the accumulation of the seismogenic tensions in the area up to the contact zone. The data obtained allows assessing exactly the place and parameters of insertion: Azimuth N 19°; gradient 16°; sliding 67 mm/year and depth of shock 55 km. The results show that the earthquakes in this zone are not simply a kind of subduction and between the subduction zone and the mighty mountain range of Andes are accumulating tensions, increasing the danger of a new strong earthquake [9].

According to the parameters obtained has been calculated the accumulated tectonic tension in the region of the last strong earthquake in 1835 with $M = 8.5$. On its basis was made a forecast for an expected strong earthquake in the zone with $M > 8.5$ [9]. The forecast, of the occurring in the study zone earthquake in March 2010 with $M = 8.8$, was cited in [10] as “a good example and successful forecast of strong earthquakes on the basis of scientific data and methodology“.

7. Monitoring and study of East-Mediterranean area

For present-day kinematics of central and East-Mediterranean area, implications of the space technologies such as GPS, shows the importance and advantages in establishing of crustal dynamics and mantle flow [11]. Fig. 10 depicts the continuous velocities and strain-rate fields by interpolating geodetic velocities from the 30-years of GPS monitoring in the region, including recent data in the *Balkans*.

Relative motion between stable Eurasia and the western Aegean Sea is gradually accommodated by distributed N-S extension from Southern *Balkans* to the Eastern *Corinth* Gulf. The westward propagation of the North Anatolian Fault (NAF) terminates in the north Aegean and that N-S extension localized in the *Corinth* Gulf and distributed in Southern *Balkans* is due to the retreat of the *Hellenic* slab.

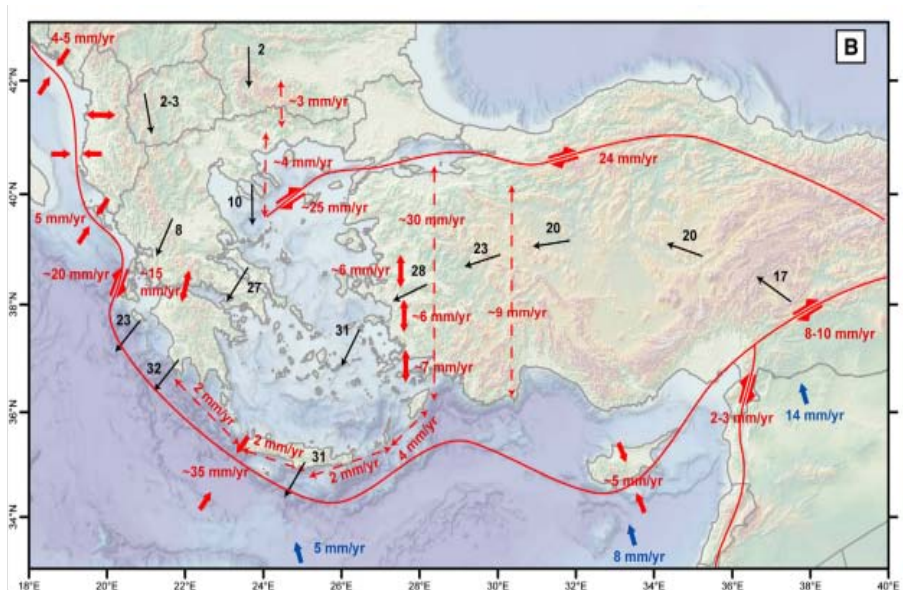


Fig. 10. Velocities and strain from the 30 years GPS monitoring of Central and Eastern Mediterranean region

Present-day kinematics and tectonic map, encompassing the Central and eastern Mediterranean, summarizing the main results and interpretation is presenting on Fig. 11. Kinematic model includes rigid-block motions as well as localized and distributed strain.

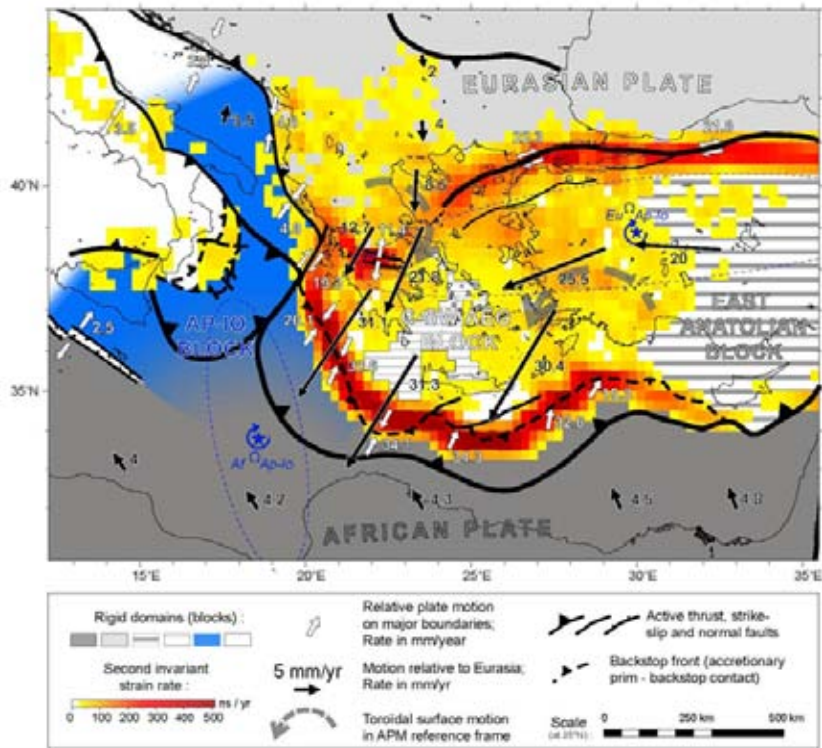


Fig. 11. Present-day kinematics and tectonic map encompassing the Central and Eastern Mediterranean, summarizing main results and interpretation

8. Conclusion

The examples presented of the application of the space-enabled technologies such as GNSS and InSAR, for study and monitoring of seismogenic zones, show their importance and advantages in establishing of regularities in the development of slow and fast motions in the seismogenic zones, in revealing the developing tectonic processes and namely the accumulation and delivering of tectonic tensions, related to the assessment of seismic hazard and the forecasting of strong earthquakes.

References

1. Hristoskov, L. Seismology, 2005; 2007 (in Bulgarian).
2. Dimitrov, D. St. Geodetic studies in the seismogenic zones. D.Sc. thesis, 2009.
3. Dimitrov, D. S., J. B. DeChabaliere, J.-C. Ruegg, R. Armijo, B. Meyer, and E. Botev, "The 1928 Plovdiv sequence (Bulgaria): fault model constrained from geodetic data and surface breaks", *Geophys. J. Int.*, 2017 (in press).

4. Vanneste, K., A. Radulov, P. DeMartini., G. Nikolov, T. Petermans, K. Verbeeck, D. Pantosti, T. Camelbeeck, D. Dimitrov, and S. Shanov, Paleoseismologic investigation of the fault that ruptured in the April 14, 1928, Chirpan earthquake (M=6.8), Southern Bulgaria, *Journal of Geophysical Research*, 2006, 111, B01303.
5. Meyer, B., M. Sebrier, and D. Dimitrov, Rare destructive earthquakes in Europe: The 1904 Bulgaria event case”, *Earth and Planet. Sci. Lett.*, 2007, 253, 3–4, 485–496.
6. Ilieva, M., P. Briole, A. Ganas, D. Dimitrov, P. Elias, A. Mouratidis, and R. Charara, InSAR investigation and fault plane modelling of 14th of August 2003 Lefkada Island (Greece) earthquake, *Tectonophysics*, 2016, 693, A, 47–65.
7. Darwin, C., *Geological observation on coral reefs, volcanic island and on South America*, Londres, 1851, 768 p.
8. Lomnitz, C., *Grandes terremotos y tsunamis en Chile durante el periodo 1535–1955*, *Geofis. Panamericana*, 1971, 1, 151–178.
9. Ruegg, J. C., A. Rudloff, C. Vigny, R. Madariaga, J. B. de Chabaliere, J. Campos, E. Kausel, S. Barrientos, and D. Dimitrov, Interseismic strain accumulation measured by GPS in the seismic gap between Constitución and Concepcion in Chile, *PEPI*, 2009, 5140, 78–85.
10. Kanamori, H., *Earthquake Hazard Mitigation and Real-Time Warnings of Tsunamis and Earthquakes*, *Pure and Applied Geophysics*, 2015, 172, 2335–41.
11. Pérouse, E., N. Chamot-Rooke, A. Rabaute, P. Briole, F. Jouanne, I. Georgiev, and D. Dimitrov, Bridging onshore and offshore present-day kinematics of central and eastern Mediterranean: Implications for crustal dynamics and mantle flow, *Geochemistry, Geophysics, Geosystems (G3)*, 2012, 13, Q09013, 25.
12. Dimitrov, D. Application of space technologies for studies and monitoring of seismogenic zones, *Aerospace Research in Bulgaria*. 2016, 28, 67–76.

КОСМИЧЕСКИ ТЕХНОЛОГИИ ПРИ ИЗСЛЕДВАНЕ И МОНИТОРИНГ НА СЕИЗМОГЕННИ ЗОНИ

Д. Димитров

Резюме

В настоящата статия са представени резултатите от изследвания, осъществени от автора или от колективи под негово ръководство или с негово участие, в различни сеизмогенни зони у нас и по света. Представените примери от приложението на космическите технологии GNSS (Global Navigation Satellite System) и InSAR (Interferometry Synthetic Aperture Radar) за изследване и мониторинг на сеизмогенни зони показват значението и предимствата на тези методи при установяване на закономерности в развитието на тектонските процеси на натрупване и освобождаване на напрежения в сеизмогенните зони, свързани с оценката на сеизмичният риск и средносрочното прогнозиране на силни земетресения.

AN UNMANNED AERIAL SURVEILLANCE SYSTEM IN URBAN ENVIRONMENTS

*Petar Getsov^{1,2}, Wang Bo¹, Dimo Zafirov², Georgi Sotirov²,
Stanimir Nachev², Ruslan Yanev², Pavlin Gramatikov², Valentin Atanassov²,
Hristo Lukarski², Svetoslav Zabunov²*

¹*Ningbo University of Technology - China*

²*Space Research and Technology Institute - Bulgarian Academy of Sciences*

Abstract

Proposed is a concept for a network of unmanned aerial systems for information acquisition in an urban environment. Different possibilities are evaluated using different types of aircraft, sensors and systems for obtaining the required objective, instrumental real-time information to support the making of adequate and reasoned management decisions, which will greatly contribute to the improvement of the quality of life of the population. The system can be applied for the detection of low flying objects, for monitoring, management and security of urban intersections, underground stations, public and private buildings, and to determine the state of the atmosphere and water areas. It will provide the opportunity to forecast and manage crises that may arise in the context of the critical urban infrastructure.

Introduction

Prognoses have been made that in 2050 up to 66 % (more than 6 billion people) of the earth's population will be living in cities and the number of cities with multi-million population will be constantly increasing. At the same time, the requirements of society for providing high quality of life and reducing of the influence of urban development upon the biosphere are ever increasing. This tendency makes us looking for possibilities to create systems that utilize the latest technical and technological developments which will allow the attainment of these requirements.

This data is being analyzed, structured and archived and is made available to people and organizations involved with the functioning and development of the smart city.

At this moment there is no universally acknowledged definition of a smart city. For the purpose of this work the authors have accepted that smart cities are those utilizing the most advanced knowledge, technology and other means for the constant improvement of the quality of life for its citizens and the environment as a whole.

For the adequate governing of a smart city a large amount of data is needed (both real time and from archives) provided by a system of sensors. This data is being analyzed, structured and archived and is made available to people and organizations involved with the functioning and development of the smart city. The system of sensors consists of devices mounted on space, aerial, land and water (stationary or mobile) carriers that gather information in real time and transmit it to other systems.

This system can be applied for the management and security provision for critical urban infrastructure, intersections, underground stations, public and private buildings for timely and adequate management of the intelligent city.

Aeronautical systems make it possible to receive and deliver information in real time with very high accuracy. Particularly promising are unmanned aerial vehicles (UAV), with which the cost of the received information is lower than with the use of satellites and manned aircraft. It is expected that by the year 2022 the total volume of the market for UAV systems will reach \$21.3 billion with an average annual growth rate of 20 %. There are estimates that this tendency is to deepen in favour of small UAV weighing up to 150 kg.

Now nearly 98 % of the worlds UAVs are heavier than air, 68 percent are of fixed wing type and rotary wing – 27 %. The proportion of the lighter than air aircraft is negligible – less than 1 %.

Unmanned aerial vehicles are becoming more efficient and more widely used, both for civil and military purposes and they themselves are starting to threaten the security of the population and air traffic, especially in the context of the urban environment. Taking into account the dangers that they can pose when they are not in the zone of direct visibility in urban areas and are under the altitude covered by conventional systems for air traffic management, there are needed activities, technical means and precautions that need to be taken to avoid unwanted actions and related consequences.

In addition, unlike traditional air targets, they are of small mass (25 kg), flying at low altitudes (< 150 m) and are moving with velocity (< 90 km/h), which makes them difficult and almost impossible to detect against the background of the joint urban terrain, characterized with tall buildings, moving people and vehicles, as well as the presence of other sources of electromagnetic, thermal, and other emissions. At the same time, the existing well-developed system for the management and air traffic control cannot be used, since the probability of detecting the unmanned aerial vehicles under specified conditions is very small.

All this leads to the development and use of special systems and sensors for the detection of low flying objects based on the different physical nature of the processes and the phenomena characterizing the functioning of UAV in real time. The concept of the monitoring system for urban environment is based on setting up a network for the surveillance of individual UAV platforms with the required scope and duration of flight, which will cover a city and its adjacent urban areas and was

designed according to the requirements established by DARPA (Defense Advanced Research Projects Agency) in the document DARPA-BAA-16-55 (Fig. 1) [2]. The Aerial Dragnet concept is based on multilevel communication, analyzing and control technology, using UAVs as tool for defense of the airspace in urban areas when intruding drones compromise the protected area.

In addition, the system carries out the classification and tracking of all small UAVs and provides a continuous updated common operational picture for the airspace under 300 m, which contains the geo refined trajectories of UAVs labeled as friend or foe in the defined area of responsibility. The dissemination of information is related to accredited users depending on the interfaces of existing security requirements of civil or military lines.

Individual system platforms are connected to a network, which allows more extensive and better coverage of the urban territory, depending on the height of the individual units. The cost of the system is relatively low, as it uses already existing and developed platforms, components and software, and the signal processors are conventional. At the same time, this provides a possibility for rapid replacement. To ensure the optimum system structure, taking into account the ratio of price for unit density of covered area [2] the network consists of 9 single local drones, each covering about 20 km^2 of the urban area of a total of 180 km^2 .

The system requires the development and integration of four key components:

- multi-platform network system including unmanned aerial platforms 9 single local unmanned platforms (UAVs Neighborhood) and one central platform (City UAV);

- sensor subsystem of small size, weight and power consumption suitable for the installation on air platforms that allows the complete monitoring of the urban environment and low-flying small moving objects;

- algorithms and software for the implementation of detection, classification and tracking of small UAV located within the area of responsibility of the system;

- center for management, maintenance and processing of the information.

The Central aircraft (City UAV) detects small flying moving objects and provides a complete surveillance of the area of responsibility, which is 180 km^2 [2]. The radar detects UAV and transmits to the Centre for management and information processing its characteristics and affiliations. It establishes whether there are open applications and UAV flight plans in the management of air traffic, and then if everything is according to the rules, it ceases to be of interest to the network aerial system. However, if the flying object has no transponder and does not meet the requirements, the City UAV immediately directs the closest local drone (UAVs Neighborhood), which collects the additional required information (20 km^2) that characterizes it (dimensions, type, destination, speed, altitude) and transmits them to the command center for making necessary decisions (Fig. 1).

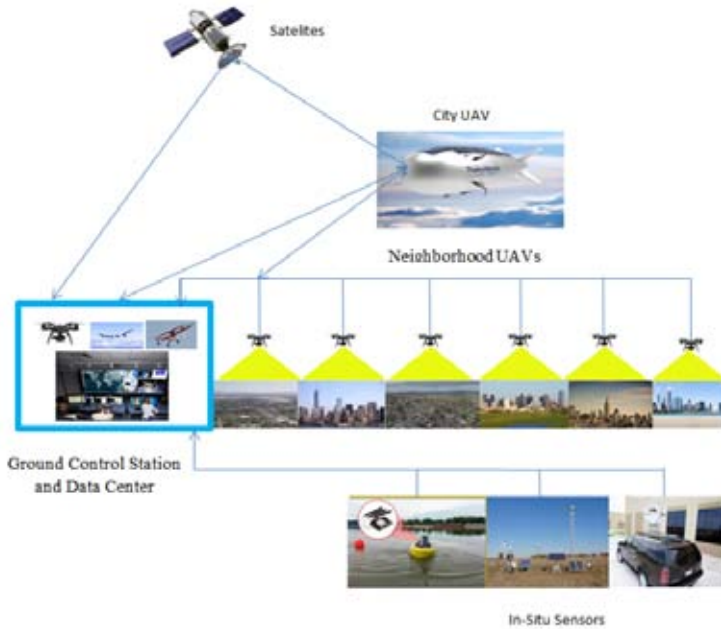


Fig. 1

The information flow could be described by the following data types: Correction data – correction signal for the highest rate positioning accuracy (NTRIP data); information data – the information data from the Neighborhood UAVs and the City UAV on the Fig. 1; sense and avoid data – data for the position, altitude, heading and speed transmitted to all of the Neighborhood UAVs and the Data and control center (Ground Control Station and Data Center).

The Neighborhood UAVs will be able to communicate to each other via encrypted and secured direct MAV radio link, which will provide at least 2–5 km of reliable radio connection in the urban area. The entire information is then transmitted via direct UAV radio link to the City UAV. Due to the long distance between the communicating Neighborhood UAVs, a cell tower from a mobile operator should be used. Using the data from the GCS for the positioning (NTRIP), the correction signal is transmitted to each of the Neighborhood UAVs and processed. As a result each video frame recorded and picture taken on the UAVs will be geotagged with the highest positioning accuracy and precision. The result is fast and accurate locating of any intruder in the sky. Additionally, the highest accuracy of positioning would deliver accurate and safe control of the Neighborhood UAVs in the urban area, lower power consumption and longer flight endurance compared to standard GPS positioning.

The use of cell towers of mobile operators to transmit the data will increase the range of the transmission within the coverage of the mobile operator network, which in urban areas would be practically unlimited. Using this method for data transmission will provide fast, accurate and full integration, and will reduce the weight of the additional equipment, used on the City UAVs and Neighborhood UAVs that will consist of a single SIM modem, which will make the following activities possible:

- Transmission of the data from the sensors – video frames, pictures, LIDAR images; RGB/NDVI/NIR images and etc.
- Accuracy correction, positioning and control – NTRIP positioning with 2.5 cm absolute accuracy, geotagging of images and frames.
- Transmission of the Sense & Avoid Data – this data will provide full information for the position of all UAVs used by the Dragnet Network, will increase the safety and will optimize the control of each particular UAV.

The possibilities for high grade accuracy positioning of UAVs are quite limited. The reason for that is the cost for developing pin-point accuracy service and the limitation of the maximum take-off weight (TOW) of the UAVs.

In present days (Q3 2017) there are not many known solutions, provided specially for UAVs. Some of the most spread and commonly used solutions are:

- Piksi RTK (provided by Swift Nav) – Swift Nav has developed some of the cheapest RTK solution for UAVs. Their electronic modules are based on the usage of RTK direct radio link with single base station. That solution provides the flexibility for the user to establish the RTK base station practically anywhere, within the direct line of sight, providing high grade accuracy and at the same time having the stand-alone integrity and autonomy for the positioning.

- Here+ RTK (provided by Hex Aero) [3] – Here+ RTK solution was specially developed for Pixhawk autopilot, which integrates open source hardware and software. It is also based on the single RTK base station and direct radio link. The main advantage of this solution is the usage of open source software, which makes it easily configurable for multiple autopilots and flight controllers, available on the market and its low price, compared to the quality.

- DJI D-RTK solution [4] – the solution for RTK from DJI is quite the same as the ones listed above. The main difference between the solutions, provided by Here+ and Piksi from one side and the solution from DJI on the other side is the fully integrated firmware and extremely friendly user interface for the setup and configuration of DJI products, which makes them very reliable and easy to use and they are very well known among the hobbyist and professionals worldwide.

These are just a few of the examples for high grade accuracy solutions for UAVs available in present days worldwide. The disadvantages of all of them however are quite the same and are present to all those products. Those disadvantages are the very small area of the coverage of the signal (up to 10 km), low reliability (because of the radio link) and they are not suitable for urbanized

areas and low-altitude applications on distances over 2÷3 km away from the base station.

Neighborhood UAVs can be multicopter platforms with electric propulsion – MCP_{ep}. Their flying and technical characteristics meet the requirements in the best way.

The high flying performances of this type of aircraft are due to the use of brushless electric motors with high specific power and efficiency. They are powered by lithium-polymer and other batteries with high specific energy and high energy density. Their control is precise, through lightweight, high speed controllers. Nowadays on the market there are MCP_{ep} with lifting characteristics, maneuverability, controllability, automation and robotics capabilities that are unthinkable in fixed-wing aircraft. The development of this type of aircraft has wide perspective. According to the latest data, in the small class UAV, consumer preferences are: 94 % for multicopters, versus 6 % for airplanes.

The MCP_{ep} require high thrust-to-weight ratio. When hovering and maneuvering in calm air they need a thrust that exceeds 1.2÷1.4 times the total weight of the vehicle. In dynamic air environment the thrust-to-weight ratio reaches 1.8÷2.0. To achieve these parameters, MCP_{ep} must carry batteries of high capacity and weight on board.

The main problem with the use of MCP_{ep} is the limited flight duration which is due to the high weight of the batteries. Currently electric propulsion of MCP_{ep} mainly uses lithium-polymer batteries. Their characteristics: specific energy C_pE_c (Wh/kg), energy density C_pP_w (W/kg), number of charge – discharge cycles, existence of "memory effect", etc. are superior to competing batteries: lead acid, nickel cadmium (NiCd), nickel metal hydride (Ni-Mh), sodium chloride (NaCl).

From a study of the commercially available batteries, it was found that the C_pE_c of lithium-polymer batteries did not exceed 300 Wh/kg. Their theoretical maximum is 400 Wh/kg. The next generations in the development of lithium batteries are lithium-sulphide and lithium-air batteries. It is expected their C_pE_c to reach (600–1000) Wh/kg. Now Li-S batteries with C_pE_c – 380 Wh/kg are available on the market. However, they quickly lose their capacity and still have a very limited number of charge-discharge cycles. This makes it difficult to use them for the propulsion of MCP_{ep}.

The use of modern composites and other materials with high strength characteristics and low relative weight, coupled with the realization of effective constructive solutions allows the empty weight of the MCP_{ep} (with engines and propellers, without batteries and payload) to be reduced to 30 %, and the payload to reach 20 % of the total weight of the vehicle.

The time for hovering of the multicopter will be:

$$(1) \quad t_h = \frac{E_h}{P_h} = \frac{\bar{E} m_b}{P_h \frac{m_h g}{m_h g}} = \frac{\bar{E} \bar{m}_b \bar{F}_h}{g} \quad [h]$$

where: m_h [kg] – the mass of the multicopter in hovering; g [m/s²] – ground acceleration; $F_h = m_h g$ [N] – needed thrust for hovering; U_b [V] – average voltage for hovering; A_h [A] – needed current for hovering; $P_h = U_b I_h$ [W] – needed power for hovering; $E_h = P_h t_h$ [kWh] – needed energy for hovering; $\bar{E} = E / m_b$ [Wh/kg] – specific energy of the batteries; $\bar{m}_b = m_b / m_h$ – specific mass of batteries; $\bar{F}_h = F_h / P_h = m_h g / P_h$ [N/W] – specific thrust for hovering;

If we take:

$$m_p = 5 \text{ [kg] mass of the payload,}$$

$$\bar{m}_p = m_p / m_h = 0,2 \text{ – specific mass of the payload}$$

$$\bar{E} = 300 \text{ [Wh/kg] – specific energy of the batteries; } t_h = 1 \text{ h.}$$

Then: $m_h = 5 / 0,2 = 25$ [kg] – the mass of the multicopter in hovering,

$$\bar{m}_b = t_h / \bar{E} \bar{F}_h g = 1,9,81 / 300,0,11 = 0,3 \text{ [kg],}$$

$$m_b = \bar{m}_b m_h = 0,3 \cdot 25 = 7,5 \text{ [kg].}$$

In our opinion, a solution of the above problems is the propulsion of MCP_{ep} by an on-board hybrid power plant (OBHPP). It should include: an internal combustion engine (ICE), an electric power generator, a controller for its control and a buffer battery to provide emergency landing or, if necessary, a low noise and vibration flight.

The OBHPP can provide a thrust-to-weight ratio exceeding 2.0 times the total weight of the MCP_{ep}, long time of hovering in one position in a turbulent air environment, high horizontal speed and precise control when changing location, powering all consumers at different payloads and flight duration of more than 2 hours.

There is information about the following hybrid propulsion versions of MCP_{ep}:

- by using fuel cells, fed by hydrogen from a tank that the multicopter carries on board;

- a combined drive by co-located ICE and an electric motor with propellers, mounted at the end of each of the multicopter arms, the ICE generates the main thrust, control is done with the electric motors;

- an ICE with a fan that generates the main thrust is located centrally in the MCP_{ep} fuselage, the stabilization and flight control are realized with electric motors located on the arms.

We believe that ICE is most suitable for OBHPP. Using liquid hydrocarbon fuels of high calorific value, they outperform all existing batteries and fuel cells. For MCP_{ep} , depending on their size, the required power is in the range 1.0÷10.0 kW. For this power range, the efficiency of existing internal combustion engines is 5÷28 %. The highest value is for four-stroke engines – with reciprocating piston movement and rotary ones (Wankel). For those with spark ignition (operating on the Otto cycle), the efficiency is up to 25 % and for with compression ignition (Diesel) – up to 28%. For two-stroke engines the efficiency is 5÷10 % lower. However, they are preferable for use in a hybrid drive of MCP_{ep} . Their advantages are: a simple design, low weight and price, high specific power (up to 1.8 times greater than that of a four-stroke ICE with the same displacement), high reliability and repairability [27–30].

Characteristics of currently available two-stroke gasoline ICE for use mainly in fixed-wing UAV that can be used for OBHPP are presented in Table 1.

When an OBHPP is powered by a gasoline two-stroke engine with 20 % efficiency, the specific energy of the hybrid power plant would be more than 2000 Wh/kg.

In the engines listed in Table 1, the latest achievements in the design, materials, organization and control of the combustion process in two-stroke ICE have not been implemented. This allows the creation of engines with up to 25 % efficiency improvement. An OBHPP, powered by such an engine, will have $C_p E_c$ above 3000 Wh/kg.

It should be noted that there is still no suitable generator with features that allow it to be optimally built in OBHPP. So far brushless generators with permanent magnets are available, but with much lower power and higher specific gravity than necessary. This requires the implementation of innovative technical solutions for electric generators of OBHPP. They consist of the following: the use of new generation permanent magnet, ceramic bearings, structural material, a common housing with Internal Combustion Engines and reduction gear, the opportunity to work in a starter and generator regime, a unique original design, high efficiency and other performance data.

Table 1

Engine type Characteristics	Desert Air DA - 150	Evolution Engines 116 Gx2	Graupner G 58	Modellmotoren 3W-157XIB2
Displacement – cm ³ /no. of cylinders	150/2	116/2	58/1	157/2
Produced power – kW/rpm	12.3/6000	6.3/6950	6.3/6950	14.3/8500
Weight – kg	3.61	1.82	1.63	4.14
Specific power – kW/kg	3.40	3.48	3.88	3.48
Efficiency – %	18	20	21	14

The innovative UAV_{mt} scheme for generating electricity on board requires the creation of entirely new automated system for the production, management, storage and distribution of electric power on board, based on new methods of design and use of new technologies and the most modern existing components, processors and semiconductor components.

The motor-generator group will be zero-reactive point, which is extremely important for the stability and manageability of multicopter systems. The moment of an OBHPP jet engine with AWD system electric generator, will be fully compensated.

When approximate estimates for the hybrid propulsion UAV_{mt} are made, analogous to the power take-off with AMO with electric batteries, it is established that, with take-off mass of 50 kg, payload – 5 kg and thrust to weight ratio of 1.8, the flight duration in troubled air is between 2 and 3 hours, which is many times greater than the one only with batteries.

We believe that an OBHPP will be of interest to the European and world market and it can be realized in UAV_{mt} and other unmanned aerial vehicles. It can find application in the terrestrial surface and remotely operated equipment with civilian and military use as well as for emergency power supply in manned light aircraft, fixed telecommunication facilities, observation posts, etc., everywhere low weight and dimensions are required.

If this hybrid power plant is mounted on a fixed-wing UAV with the same total weight of 50 kg, speed – 150 km/h and quality – 10, the endurance of this aircraft will be significantly greater (about 7 hours) which can be explained by the much lower power needed due to the higher aerodynamic quality. Taking this into account, it is suggested to use a fixed-wing UAV with a hybrid on-board power plant for the central control system.

To a large extent, the characteristics of the selected types of platforms and the safety of the system is determined by the weight and dimensions of the sensor subsystem used for the monitoring of the area of responsibility. Existing sensors for detecting, classifying and tracking urban UAVs are cameras and systems operating in the visible and infrared spectrums, radars operating on different physical principles to explore systems of type a-alien, "sonar" systems, etc.

To detect small targets in urban conditions, portable radars are used to survey the monitored area. Continuous Wave (CW) radars are used for this purpose, which involve Frequency Modulated Continues Wave (FMCW) radars and Doppler radars. In the first group, periodic variations in the frequency are used to determine the range to the target, while the second uses the Doppler Effect. Modern miniature radars combine both modes of operation. Practically, systems usually work in Doppler mode until target is detected, and once the target is detected, the FMCW mode is activated to determine distance-to-target information. In this case, a relatively low level of false alarms is maintained by reacting only to the targets with some radial velocity relative to the radar. Furthermore, the overall reaction time is decreased by the use of Doppler mode since a target's presence and velocity can be acquired from a single sample window, whereas FMCW must use multiple sample windows to determine the velocity based on the differentiated ranges [12–14].

Since most aircraft, while on the move contain rotating components moving in a periodic sequence, there is a unique Doppler signature for most devices. Prior knowledge of this "signature" can be used to determine in real time the presence of a known target within the currently depicted scene. There are numerous ways to define the signature of targets, but most commonly the identification methods include the use of a parametric target model [12–14].

This approach is appropriate for certain groups of aircraft because of the smaller number of types and variants of the group of vehicles. However, for a certain group of miniature UAVs (with a mass < 25kg), the number of possible variants is considerably higher. From a practical point of view, this implies that nonparametric patterns are preferred when manual generation of a parametric model for each UAV option is not applicable [12–14, 17].

In Table 2 are given parameters of on-board radars used in UAV [14–16].

Table 2

Company	Transponder	Size/Weight	Input Power
uAvionix Corporation	Ping200Si ADS-B	91 × 57 × 19mm/80 g	11–33 VDC, 2W
Sagetech	XPC-TR Mode C	89 × 46 × 18 mm/100 g	10–32 VDC
Sagetech	XPS-TR Mode S with ADS-B	89 × 46 × 18 mm/100 g	10–32 VDC
Sagetech	XPG-TR Mode S Transponder with ADS-B Out and GPS	102 × 47 × 26 mm/147 g	10–32 VDC

A great deal of attention is paid to the development and use of on-board radars for UAV for issues regarding the identification of detected in open air and on the ground targets. At present, a lot of companies are producing high-tech and reliable S-mode transponders. They provide the information needed to identify UAVs by the air traffic management and the UAV Control and Management Center.

In Table 3 are given the parameters of transponders used in UAV [18, 19]. After the detection and identification of an object, surveillance systems further recognize it, and then, if necessary, follow the object's trajectory.

A major component of the surveillance systems are surveillance cameras in the visible and infrared spectrum. They are located on stabilized platforms with the ability to direct the cameras to three coordinates in space.

Table 3

Company	Radar	Transmitted frequency/ Transmitted Power	Range /Field of view	Size/Weight	Input Power
	FMCW/ Doppler	10.5 GHz / 10 mW		155×100×90 mm/230 g	10–42 V DC
Echodyne	Metamaterials Electronically Scanning Array		3 km/120×80°	180×100×10 mm/750 g	
Unmanned Systems Research Institute	Phased-array radar		100 m	350 g	
InSAR	NanoSAR/ Synthetic Aperture Radar	X band	1 km/1 m	158×190×114 mm/900 g	
Brigham Young University	MicroSAR	X band (9.75 GHz)		120×800×400 mm/2.8 kg	12–18 V DC

Surveillance cameras supporting Ultra High Definition TV (3840×2160) 4K standard with maximum resolution 8M pixels and surveillance cameras supporting HDTV standard (1920×1080) with maximum resolution 2M pixels are used in the visible area.

For the first type of cameras, when the simultaneous observation of the entire area of 20 km^2 is performed, the size of 1 pixel in the observed scene is 2.4 m^2 or $1.6 \times 1.6 \text{ m}$. In order to recognize objects measuring $0.5 \times 0.5 \text{ m}$ in the observed scene, a resolution of at least 8×8 or 10×10 pixels is necessary, i.e. the pixel size should be $7 \times 7 \text{ cm}$ or $5 \times 5 \text{ cm}$. This resolution can be achieved by reducing the viewed area and using variable focus lenses (zoom lenses).

When using a lens with a fixed focal length, it may cover an instantly observed area of 20 736 m^2 ($144 \times 144 \text{ m}$) with a resolution of $5 \times 5 \text{ cm}$.

When using a $\times 10$ zoom lens, a viewing area of 0.2 km^2 ($455 \times 455 \text{ m}$) can be observed at any given time and further focused on with a zoom lens for a $5 \times 5 \text{ cm}$ resolution for the purpose of object recognition.

For the second type of cameras (with a lower price) when using a $\times 10$ zoom lens and HDTV camera can be captured an area of 0.05 km^2 ($227 \times 227 \text{ m}$) with a $15 \times 15 \text{ cm}$ resolution and further focused with the help of a zoom lens for a $5 \times 5 \text{ cm}$ resolution for the purpose of object recognition.

In the infrared or thermal spectra, the surveillance cameras support a significantly lower resolution, with good samples reaching a resolution of 640×480 pixels. They are used for observation in bad weather or other conditions and at night. They are commonly used with surveillance cameras in the visible area, with the two images being able to be mixed. Analyzes are presented in Table 4.

In the recent years due to the strong demand for drone detection, identification and tracking systems, a new major technological approach has been established – the acoustic method. A few companies are offering detection, identification and tracking systems involving the acoustic approach. Such a system is SafeSky Drone Detection and Neutralization System [20] by Advanced Protection Systems. Their acoustic array detects drones from up to several hundred meters. Furthermore, this system is a combination of proprietary X-band radar, acoustic array, camera for visual detection, and RF sensors. The most contemporary and cutting-edge technological method for acoustic drone control is a further development of the acoustic array detection system leading to the acoustic camera drone detection method. Companies that have large experience in acoustic cameras intended for other applications are trying to adapt their products and knowledge and create drone control acoustic cameras. Preliminary testing is carried out by the Swiss company Distran [21]. The company has been developing ultrasonic acoustic cameras like Ultra M used for ultrasonic examination and detection of mechanical faults in industrial equipment.

Table 4

Spectral region	Standard / sensor pixels	Lens type	Observed area	Spatial resolution	Maximum spatial resolution
Visible (Vis)	UHDTV 3840 × 2160	Fixed focus	20 000 km ²	2.4 m ² (1.6 × 1.6 m)	
			20 736 m ² (144 × 144 m)		5 × 5 cm
		Zoom lens	0.2 km ² (455 × 455 m)		5 × 5 cm
	HDTV 1920 × 1080	Fixed focus	0.05 km ² (227 × 227 m)	15 × 15cm	
		Zoom lens	0.05 km ² (227 × 227 m)		5 × 5 cm
	Infrared (IR)	TV 640 × 480	Fixed focus	0.05 km ² (227 × 227 m)	35 × 45cm

Other manufacturers of acoustic cameras, though not yet specialized in drone detection, are Acoustic Camera [22], Cae-Systems in Germany [23], Microflown [24], NLA Acoustics [25], Norsonic [26] etc.

The advantage of acoustic cameras over other acoustic methods for detection is the generation in real-time of acoustic color visualization of the observed volume and visual signaling of the operator about the position and other characteristics of the detected and tracked drone/drones.

In the Center for the operation, management and processing of received data and coordinates of the UAV flights in the airspace of intelligent city are received, analyzed and structured. The large volume of information received by them is networked with other similar centers, with cloud structures and with users of processed information. It carries out the maintenance of the UAV. After landing they are checked, information stored onboard is downloaded, reprogrammed and again depart on schedule.

In the Center for data processing is done the recognition of small drones resulting from images from cameras mounted on anchored platforms. Development of software for processing is performed on 3 main stages:

- the first stage involves creating algorithms for detection of small drones written in high level language: MatLab, IDL, TensorFlow and others;
- after setting up and tuning the algorithms proceed to their application in workstations for the collection of information in real conditions. There can be used

C, C++ CUDA or another language which allows speeding up the process of treatment;

- in the third stage-adapted algorithms tuned to specialized hardware mounted on board of the Central UAV using the DSP, FPGA, GPU or another approach allowing rapid real-time processing of the information received are implemented.

All these elements provide the necessary hardware, software, qualified staff and resources for long term and sustainable operation of the system.

Conclusions

The proposed concept and functional network scheme for an unmanned aerial system is the solution of the paradigm to detect, identify and track low-flying aircraft in urban terrain area characterized by tall buildings, moving people and vehicles, as well as in the presence of other sources of electromagnetic, thermal, and other emissions.

Conducted analysis and studies show that the development and use of hybrid power on-board unit will solve the issue of the flight endurance of unmanned platforms included in the composition of a network an unmanned aerial system and will increase the permissible weight for the sensor payloads, enabling the monitoring of the overall urban environment and low flying small moving objects.

Using the SIM modem on each UAV will provide the main advantages amongst any other technology for transmitting data and in flight communication: full integration; small dimensions and weight with practically unlimited range; high-end redundancy; full control of UAV; multi-data transmission.

Application of Phased Array Radars on the basis of new technologies and new signals and methods for their processing on board of UAV will increase their capabilities in urban areas.

The technology described, as a final conclusion will be the next century technology which will make the difference and will bring high-end accuracy together with all of the needed data during flight of any of the UAV in particular area, which will be the focus of all future regulations, regarding the usage of UAVs in urban areas.

Acknowledgements

I. The study was performed with the use of the:

1. Set up under the project BG161PO003-1.2.04-0053 "Information complex for aerospace environmental monitoring" (IKAMOS), financed by the operational program "Development of the competitiveness of the Bulgarian economy" 2007–2013, co-financed by the European Regional Development Fund and from the national budget of the Republic of Bulgaria.

2. Project "Strengthening and Expansion of the Aerospace Technology Transfer Office in the Field of Protection of Citizens' Health in Disasters" – BG161PO003-1.2.02 under the Operational Program "Development of the Competitiveness of the Bulgarian Economy" 2007–2013.

II. The authors gratefully acknowledged the support of K. C. Wong Education Foundation.

References

1. World's population increasingly urban with more than half living in urban areas, 10 July 2014, N. Y. <http://www.un.org/en/development/desa/news/population/world-urbanization-prospects-2014.html> (accessed on 10 Dec. 2017)
2. Alberding GmbH Solutions. <https://www.alberding.eu/en/ntripcaster.html#pic8>
3. Hex Aero. <http://www.hex.aero/> (last day accessed 10 December 2017).
4. DJI D-RTK. <https://www.dji.com/d-rtk/info> (last day accessed 10 December 2017).
5. Dragnet overview. <https://www.virginiabids.us/virginia-bids/bids-ADP1475885789000092.htm> (last day accessed 10 December 2017).
6. Aero Vision. www.aero-vision.net (last day accessed 10 December 2017).
7. CNH Industrial. <http://www.cnhindustrial.com/en-us/Pages/homepage.aspx>
8. Interagri Bulgaria JSC. <http://www.interagri.bg/> (last day accessed 10 December 2017).
9. Precision Hawk. <http://www.precisionhawk.com/latas> (accessed on 10 December 2017)
10. Trimble Positioning Services. http://www.trimble.com/positioning-services/pdf/whitepaper_rtx_fast.pdf (last day accessed 10 December 2017).
11. 18th International Technical Meeting report. http://www.geopp.com/pdf/ion2005_fw.pdf
12. 3DR Robotics. <https://3dr.com/> (last day accessed 10 December 2017).
13. Allistair Moses Matthew J. Rutherford , Kimon P. Valavanis, Radar-Based Detection and Identification for Miniature Air Vehicles, 2011 IEEE International Conference on Control Applications (CCA) Part of 2011 IEEE Multi-Conference on Systems and Control, Denver, CO, USA. September 28-30, 2011, 933–940.
14. Moses, A. M.J. Rutherford, and K.P. Valavanis, Radar-based detection and identification for miniature air vehicles, 2011 IEEE International Conference on Control Applications (CCA), Denver, CO, 2011, 933–940. DOI: 10.1109/CCA.2011.6044363 (last day accessed 10 December 2017).
15. Long, D., Compact, low-cost synthetic aperture radar, 30 December 2006, SPIE Newsroom. DOI: 10.1117/2.1200610.0456
16. Boyle, A. Echodyne gets \$29M from NEA, Bill Gates and others to boost radar for drones, GeekWire - Space & Science. <https://www.geekwire.com/2017/echodyne-gets-29m-boost-nea-bill-gates-others-low-cost-radar/> (online on May 22, 2017).
17. Synthetic Aperture RADAR. http://www.barnardmicrosystems.com/UAV/features/synthetic_aperture_radar.html (last day accessed 10 December 2017).

18. Ji, Z., Hu, E., Zhang, Y. et al. Research on micro-Doppler feature of spatial target, J. Wireless Com. Network, 2017, 177. DOI: 10.1186/s13638-017-0963-7
19. ADS-B Transceivers, Receivers and Navigation Systems for Drones, <http://www.unmannedsystemstechnology.com/company/uavionix-corporation/>
20. UAV Transponders & Tracker Kits. <http://www.unmannedsystemstechnology.com/company/sagetechnology-corporation/> (last day accessed 10 December 2017).
21. Advanced Protection Systems. <http://www.detectdrones.com/#system> (10 Dec. 2017).
22. Distran. <https://www.distran.ch> (last day accessed 10 December 2017).
23. Acoustic Camera. <https://www.acoustic-camera.com/en.html> (10 Dec. 2017).
24. CAE Systems. <https://www.cae-systems.de/en/products.html> (10 Dec. 2017).
25. Microflown Technologies. <http://www.microflown.com> (accessed on 10 Dec. 2017).
26. Noiseless Acoustics. <http://www.nlacoustics.com> (last day accessed 10 December 2017)
27. Acoustic Camera Nor848A. <https://web2.norsonic.com/product/324/>(10 Dec. 2017).
28. Ravi, A. and A.S Arena, Jr., UAV Power Plant Performance Evaluation, Department of Mechanical & Aerospace Engineering Oklahoma State University, 49-th AIAA Aerospace Science Meeting including the New Horizons Forum and Aerospace Exposition, 4-7 January 2011, Orlando, Florida, 1–6.
29. Campbell, C., E. Dittman, J. Mac Rae, C. Ehringer, A. Stone, K. Lake, S. Haskin, and R.R. Mankbadi, Design of a Hybrid Electrical Propulsion System, Embry-Riddle Aeronautical University and the FCAAP, Daytona Beach, 52nd AIAA/ASME/ASCE/AHS/ASC, Structures, Structural Dynamics and Materials Conference 4-7 April 2011, Denver, Colorado, 2–4.
30. Schomann, J., Hybrid-Electric Propulsion System for small Unmanned Aircraft, Technical University of Munich, Thesis, 15–26.
31. Richard, R. Glasscock, Design, Modelling and Measurement of Hybrid Powerplant for Unmanned Aerial Vehicles, School of Electrical Engineering and Computer Science Queensland University of Technology, M.Sc. of Engineering, 9–17.

БЕЗПИЛОТНА СИСТЕМА ЗА НАБЛЮДЕНИЕ В ГРАДСКА СРЕДА

*П. Гецов, В. Бо, Д. Зафиров, Г. Сотиров, Ст. Начев, Р. Янев,
П. Граматиков, В. Атанасов, Хр. Лукарски, Св. Забунов*

Резюме

Предложена е концепция за мрежа от безпилотни въздушни системи за събиране на информация в градска среда. Различните възможности се оценяват с помощта на различни видове въздухоплавателни средства, сензори и системи за получаване на необходимата цел, инструментална информация в реално време за подпомагане на вземането на адекватни и обосновани управленски решения, които значително ще допринесат за подобряване на качеството на живот на населението. Системата може да се използва за откриване на летящи обекти, за наблюдение, управление и сигурност на градските кръстовища, метростанции, обществени и частни сгради и за определяне състоянието на атмосферата и водните зони. Тя ще осигури възможност за прогнозиране и управление на кризи, които могат да възникнат в контекста на критичната градска инфраструктура.

INNOVATIONS IN THE AREA OF UNMANNED AERIAL VEHICLES

Petar Getsov^{1,2}, Wang Bo¹, Svetoslav Zabunov², Garo Mardirossian²

¹*Ningbo University of Technology - China*

²*Space Research and Technology Institute - Bulgarian Academy of Sciences*
e-mail: bo305@hotmail.com; office@space.bas.bg

Abstract

The current paper discloses some innovations in the field of unmanned aerial vehicles. The latter were developed recently at Space Research and Technology Institute at the Bulgarian Academy of Sciences. This article shows the advantages of the arrangement, and the technical and operating characteristics of the following inventions:

- *Multicopter Helicopter*
- *Tandem Helicopter*
- *Vertical Take-off and Landing Aircraft*
- *Three Phase Brushless Direct Current Motor Control System*
- *Unmanned Aerial Vehicles Antenna System*
- *Wireless Universal Serial Bus Realized through Telemetry Radio Link for Unmanned Aerial Vehicles*

All of the presented innovations are subject to patent protection, while most of them have been honoured with the highest awards at international foreign forums for innovations.

Introduction

Due to its simplicity, reliability, comparatively easy technical servicing and maintenance, as well as the ability to take-off and land from runways with minimal dimensions, the unmanned aerial vehicles (UAVs), also known as drones, are entering more and more different areas of human activities. This development motivates active work for optimization of their major technical and operating parameters – weight, energy consumption, flight duration, etc.

The current article is devoted to some innovations in the field of UAVs that were introduced in the last few years at Space Research and Technology Institute – the Bulgarian Academy of Sciences. All of the presented innovations are subject to patent protection, while most of them have been honoured with the highest awards at international foreign forums for innovations.

Multirotor Helicopter

The multirotor helicopter named "Bulgarian Knight" [7] is presented on Fig. 1. It consists of twelve rotors $1^I, 1^{II}, \dots, 1^{XII}$, mounted below the helicopter airframe plane 2 using an optimal configuration of the rotors. The latter establishes maximum coverage without overlap. The airframe configuration represents a pair of parallel beams 2^I (2^{I-1} and 2^{I-2}), to which another pair of parallel beams 2^{II} (2^{II-1} and 2^{II-2}) is attached. The two pairs of beams are orthogonal to each other and lie in the same plane.

This configuration is applicable to unmanned and manned aerial vehicles, propelled by electrical motors. Such aircraft may be used in various activities such as scientific research operational tasks with civilian or military pattern. By means of the aerodynamic forces, created by the rotors, flight of the helicopter is maintained and its motion in the air in vertical and horizontal direction is controlled. The accelerated airflow, created by the rotors, and directed downwards, does not interfere with the airframe, positioned above the rotors, and hence avoidance of aerodynamic drag in the downward direction is achieved. The latter drag is undesirable.

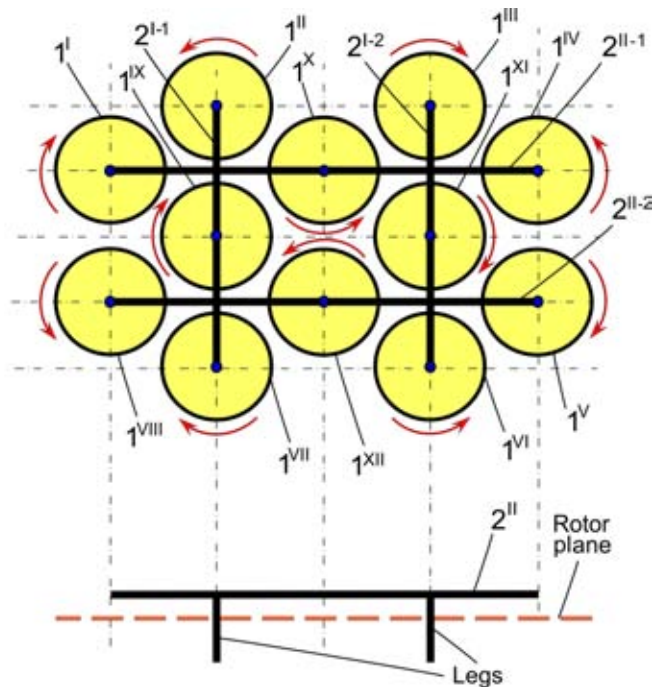


Fig. 1. Scheme of the twelve rotor helicopter "Bulgarian Knight"

On the other hand, the optimal rotor configuration (the position of rotors in respect to each other) and airframe topology guarantee minimal weight of the flying machine. By doing so, flight duration, range and payload capabilities are maximized.

Tandem Helicopter

The tandem helicopter [8] is denoted on Fig. 2. It consists of two horizontal rotors 1^I and 1^{II} , located under the airframe plane 2. The airframe configuration represents a horizontal beam 2^I , at the two ends of which two vertical consoles are mounted 2^{II} and 2^{III} . At the top ends of both consoles two pairs of vertical rotors 3^I , 3^{II} , 3^{III} and 3^{IV} are installed.

The application of this innovation is in unmanned and manned flying machines, with electrical motors that are used for aerial photography, remote sensing and other activities in the field of defence, fight against organized crime and terrorism.

By means of aerodynamic force, created by the rotors, sustained flight is achieved of the tandem helicopter and its motion in the air in vertical direction. Using the vertical rotors attitude control of the airframe is attained and further horizontal motion is achieved. The accelerated airflow created by the main horizontal rotors and directed downwards does not flow against the airframe. This is due to the airframe being positioned above the horizontal main rotors and in this way undesired aerodynamic drag in downward direction is avoided. Hence, the flight time, range, and the weight of the payload are maximized.

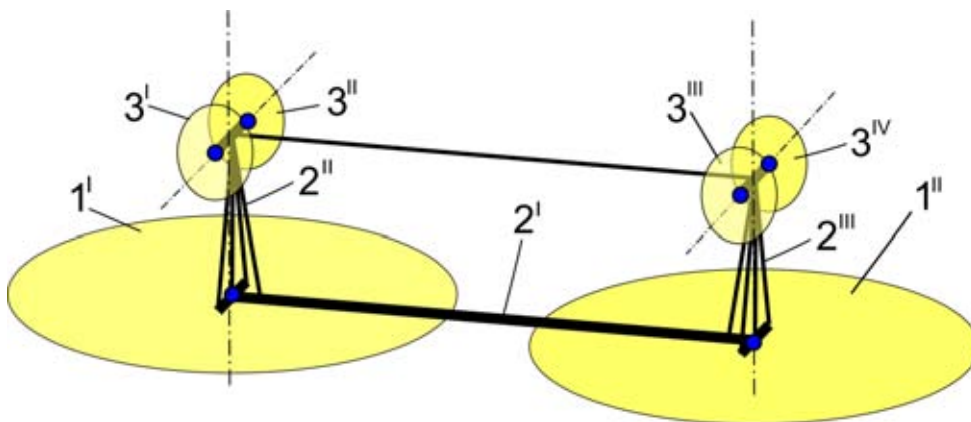


Fig. 2. Scheme of the tandem helicopter

Vertical Takeoff and Landing Aircraft

The innovation refers mostly to unmanned aerial vehicles [5]. It consists of a propeller driven fixed wing airplane with vertical take-off and landing capabilities.

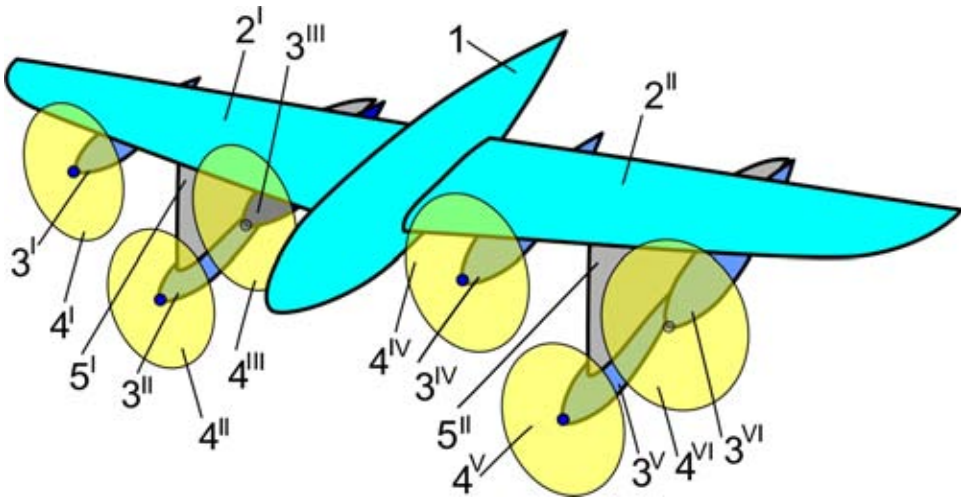


Fig. 3. General view of the VTOL aircraft configuration

The application of this invention is in remote sensing activities, people search and rescue operations, activities relevant to ecology, disaster and industrial accidents and catastrophes, intelligence and reconnaissance, etc. In principle the invention may be used with manned aircraft.

The discussed airplane has two modes of flight: helicopter and airplane mode. The take-off and landing procedures are carried out in helicopter mode. In this mode the aircraft lands on its tail using the consoles supporting motor nacelles as landing legs. The normal flight is performed in airplane mode. Transition from helicopter flight mode to airplane flight mode and vice versa, is achieved through reorientation of the airframe. Flight direction in airplane mode is defined by the fuselage streamlined form similarly with any other fixed wing airplane.

According to Fig. 3 the aircraft consists of a fuselage 1, fixed wing 2 attached to the latter (right half wing 2^I and left half wing 2^{II}). The wing carries six motor nacelles 3 with motors inside, four of which are mounted directly to the main wing and two – using consoles 5 (see Fig. 3). All motors are turning fixed pitch propellers 4.

Three Phase Brushless Direct Current Motor Control System Used in Drones

The following invention [1, 2] is a system for control of three phase brushless direct current motors used in drones. The invention improves the efficiency of motor control and consequently the efficiency of flight in comparison with the existing systems. It is applicable to drones (helicopters and airplanes) that are propelled using electric energy stored in batteries.

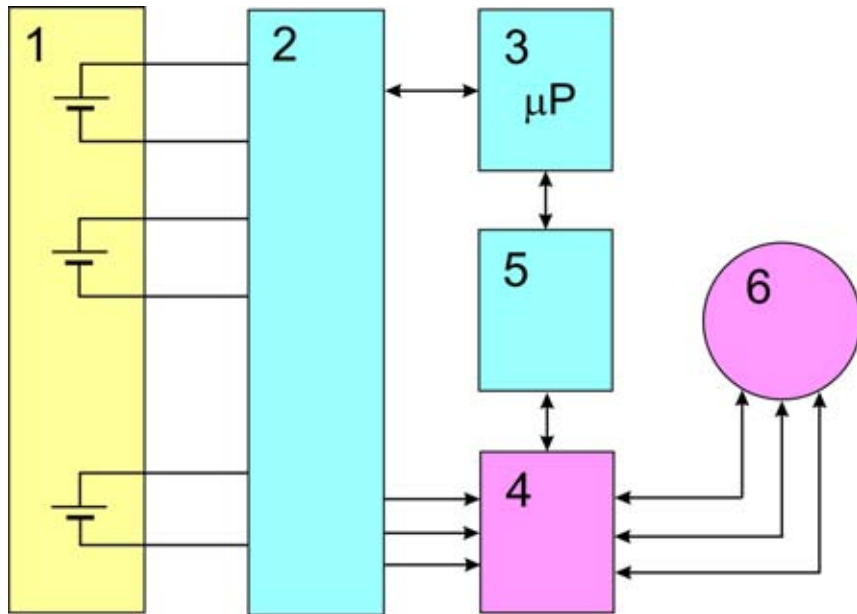


Fig. 4. Block schematic of the three phase brushless motor control system

Through commutation of the battery cells, according to the current mode of flight, efficiency is improved and flight time is enhanced. The system is shown on Fig. 4. It consists of battery block 1 with battery cells $1^I, 1^{II} \dots 1^n$. The battery cells terminals are connected to commutator block 2. The latter is connected to electric motor control block 4 and commutator control block 3. Commutator control block is connected to command block 5. The latter is in connection with the electric motor control block. Finally, the electric motor control block has three connections to the three phase coils of the electric motor 6.

The application of this invention, besides in electrically propeller UAVs, may be in home appliances, electric cars, boats and ships, etc. that use electric energy from an electric battery as power supply.

Unmanned Aerial Vehicles Antenna System

The invention [3, 4] realizes two-way radio link between unmanned aerial vehicle and a ground station. The application is in control of and information exchange with an UAV. The radio link uses circular polarization of the electromagnetic field. The antenna directivity diagram is adjusted electronically and dynamically through a phased antenna array in congruence with the momentary orientation of the drone.

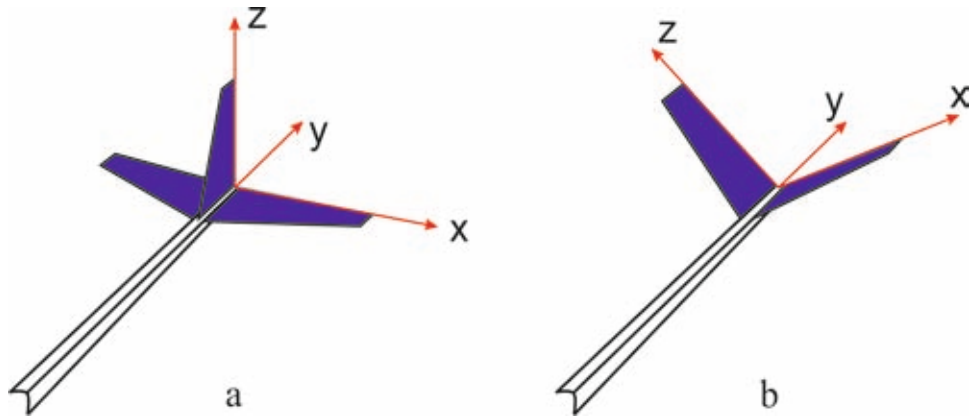


Fig. 5. Antenna elements position in the aircraft empennage:
a) Classic empennage, b) V-tail empennage

The antenna system uses the empennage of an unmanned aircraft to dispose the three mutually orthogonal antenna elements x , y and z (Fig. 5).

The block diagram of the invention is shown on Fig. 6. The system consists of three mutually orthogonal antenna elements 1^x , 1^y and 1^z of the airborne antenna array. The latter are connected to the three bilateral terminals of the commutation block 2 (Fig. 6). The three outputs of the commutation block are connected to the three inputs of the preamplifier 3. Preamplifier's output connections go to the three inputs of the receiver phasing and impedance matching block 4', output of which is connected to the input of receiver 5. The fourth input of 4' is connected to one of the outputs of autopilot 7. To a triad of inputs of the commutation block 2 the three outputs of the transmitter phasing and impedance matching block 4'' are connected. The output of the transmitter 6 goes to the input of block 4''. The second output of autopilot 7 is connected to the second input of block 4''. The fourth input of commutation block 2 receives signals from the output of command block 8, which is in bilateral connection with the receiver 5 and the transmitter 6.

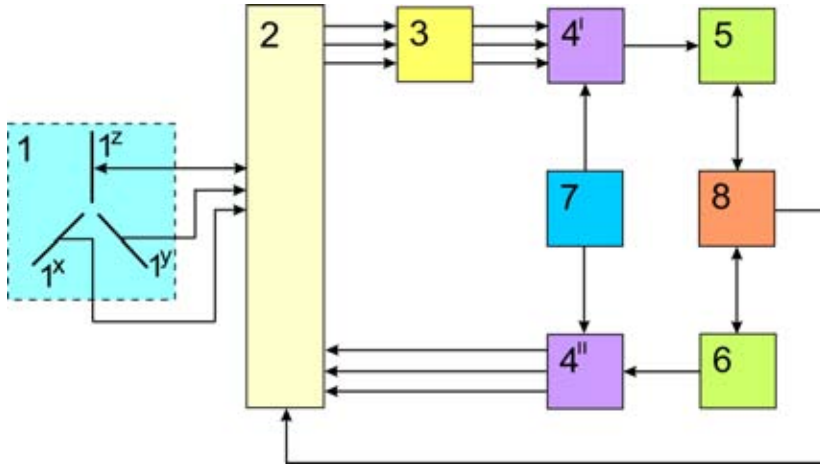


Fig. 6. Block-diagram of the antenna system

Wireless Universal Serial Bus Realized through Telemetry Radio Link For Unmanned Aerial Vehicles

This innovation refers to a wireless universal serial bus (USB), realized using wireless radio link through off-the-shelf telemetry modules for UAVs [6]. The application is with USB-devices onboard of UAVs that, using the invention, may have USB-wireless connection with a ground-based computer. Examples of such devices are web cameras, web microphones, USB-cameras, etc.

Drawbacks of the existing wireless USB technology are related to the used modulations and frequencies. The described invention aims at creating a wireless USB connection that will lack the so described disadvantages of the existing similar devices.

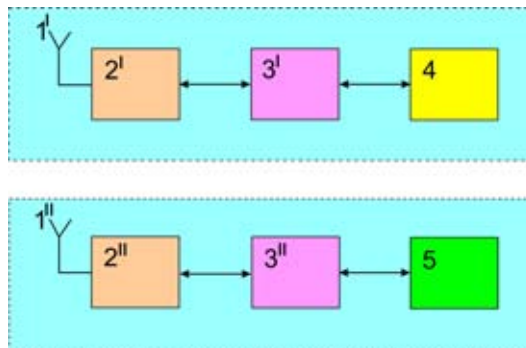


Fig. 7. Block diagram of wireless USB for use over the telemetry radio link of UAVs

The wireless-USB is presented on Fig. 7. It consists of airborne station and a ground station. The two stations are built out of airborne antenna 1^I and ground based antenna 1^{II} respectively. These are connected to airborne module for telemetry 2^I and ground based telemetry module 2^{II} respectively. The latter two are in respective bilateral connection with airborne USB interface module 3^I and ground based USB interface module 3^{II}, which on their part are in bilateral connection with airborne USB device 4 and ground based computer 5 respectively.

The application of this innovation is in electrically propelled unmanned and manned flying machines that are used for aerial photography, remote sensing and other activities in the field of defense, fight against organized crime and terrorism.

Development and testing of some prototypes will be provided in Ningbo University – China.

References

1. Zabunov, S., P. Getsov, and G. Mardirossian. Control System for Three Phase Brushless Direct Current Motor. Utility model № 2723/04.06.2014. *Patent Office of Republic of Bulgaria.*
2. Zabunov, S., P. Getsov, and G. Mardirossian. Control System for Three Phase Brushless Direct Current Motor. Patent application reg. № 111705/20.02.2014. *Patent Office of Republic of Bulgaria.*
3. Zabunov, S., P. Getsov, G. Mardirossian, and G. Sotirov. Unmanned Aerial Vehicles Antenna System. Utility model № 2737/17.03.2014. *Patent Office of Republic of Bulgaria.*
4. Zabunov, S., P. Getsov, G. Mardirossian, and G. Sotirov. Unmanned Aerial Vehicles Antenna System. Patent application reg. № 111720/12.03.2014. *Patent Office of Republic of Bulgaria.*
5. Zabunov, S., P. Getsov, and G. Mardirossian. Vertical Take-off and Landing Aircraft. Utility model № 2765/12.05.2014, *Patent Office of Republic of Bulgaria.*
6. Zabunov, S., P. Getsov, G. Mardirossian, and G. Sotirov. Wireless Universal Serial Bus Realized through Telemetry Radio Link for Unmanned Aerial Vehicles. Utility model № 2804/10.07.2014, *Patent Office of Republic of Bulgaria.*
7. Zabunov, S., G. Mardirossian. Multirotor Helicopter. Patent application reg. № 112131/02.11.2015, *Patent Office of Republic of Bulgaria.*
8. Mardirossian, G., P. Getsov, and S. Zabunov. Tandem Helicopter. Patent application reg. № 112529/15.06.2017, *Patent Office of Republic of Bulgaria.*
9. Ching, T.W. Soft-switching Converters for Electric Vehicle Propulsion. *Journal of Asian Electric Vehicles*, 2007, 5, 2.
10. http://www.usb.org/developers/docs/usb_31_031114.zip
11. IEEE GET ProgramTM, <http://standards.ieee.org/about/get/> (accessed 10 January 2018)
12. Robertson, P. and S. Kaiser, The effects of Doppler spreads in OFDM(A) mobile radio systems, Vehicular Technology Conference, 1999. VTC 1999 - Fall. IEEE VTS.

ИНОВАЦИИ В ОБЛАСТТА НА БЕЗПИЛОТНИ ЛЕТАТЕЛНИ АПАРАТИ

П. Гецов, В. Бо, С. Забунов, Г. Мардиросян

Резюме

В статията са представени някои иновации в областта на безпилотни летателни апарати, разработени през последните години в Института за космически изследвания и технологии при Българска академия на науките (ИКИТ-БАН). Показани са накратко идеята, конструкцията и технико-експлоатационните характеристики на следните иновационни разработки:

- Мултироторен хеликоптер,
- Тандем хеликоптер,
- Самолет с вертикално излитане и кацане,
- Система за управление на трифазен безколекторен електродвигател,
- Антенна система за безпилотен летателен апарат,
- Безжична универсална серийна шина за телеметрия на безпилотни летателни апарати.

Всички представени иновации са обект на патентна защита и са отличени с високи награди на наши и международни иновационни форуми.

ELECTRIC MOTOR-GENERATORS FOR UNMANNED AERIAL VEHICLES

Pavlin Gramatikov

*Space Research and Technology Institute – Bulgarian Academy of Sciences
e-mail: pgramatikov@space.bas.bg*

Abstract

Permanent magnets (PM) are used in the new multi-pole electric generators. Direct connection without a reducer greatly simplifies the design and provides a long life and low weight. To improve the technical parameters of electric generators, are used PM based on rare-earth Nd-Fe-B magnets. The absence of sliding electrical contacts significantly increases life and reliability in comparison with electric generators of direct current and synchronous generators.

Special attention is given to high specific indicators for the developed power per unit of weight. Additional computer simulation has been made. The results of calculating the magnetic field and moments for models of electric motors with permanent magnets are considered. It is shown that the configuration of the magnetic system has a significant effect on the electrical characteristics of the electric generator.

1. Introduction

Drone hybrid system (DHS) for hybrid drones (HD) is the most promising direction of development of the unmanned aerial vehicles (UAV). Usually HD refers to the aircraft with vertical take-off and landing (VTOL). Hybridity is the combination of several types of power unit in one drone.

Today, the U.S.A. has a "Section 333" of the rules of flight safety. It prohibits UAV from flying beyond line of sight of the operator, which is defined in 480 m and a height of more than 61 m. In August 2016 entered into force, the 107th section of the Chapter. It allows operators with permission to operate UAV beyond line of sight (up to 32 km) and at altitudes of up to 122 m. It is allowed to fly with UAV weighing up to 25 kg. These new rules will help the development of DHS and increase the flight time to 4 hours.

Lithium polymer batteries (Li-Po), which power the majority of UAV can withstand at least 30 min. For the record, Mavic Pro DJI drone has a flight time of about 25 min, the DJI Phantom 4 has about 30 min [1]. Unofficial record of 2015 was set from Energy Technologies, when its hydrogen-powered drone was airborne for 3 h and 43 min. Hydrogen fuel cells and hydrogen-acid fuel cells are the most

promising type of power plant for UAVs. They work on the principle of electroplating as a battery, but the fuel (hydrogen) is supplied from the tank. For efficiency, they are much superior to the batteries in the small UAVs. The HYCOPTER is the world's first hydrogen fuel cell powered multi-rotor UAV. It is currently being readied for a record flight endurance of over 4 h, or 8 to 10 times the flight duration of equivalent power systems today [2].

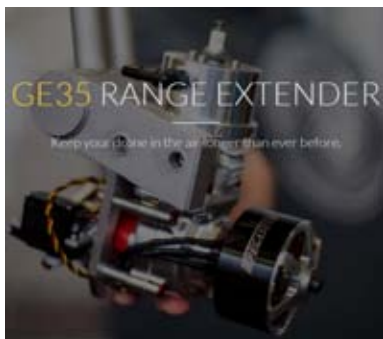
The company Quaternium Technologies, is a leading European brand for long flying drones, through his fuel-electric quadcopter - HYBRiX.20. It set a world record for flight duration - 4 h and 40 min. This HD is built on the classic by the electric BLDC motors with powerful generator set on the basis of the two-stroke engine, which supports energy in the battery of the drone throughout flight [3].

There are drawbacks for HD on gasoline engine (GE) such as the need to install an ignition system. The electromagnetic field (generated by the ignition system) also causes interference with the control channels and information transfer. Problem can be fixed with the help of additional equipment and a well-designed layout multicopter. For this purpose it is not allowed to place the radio receivers closer than 0.3 m from the ignition. Another significant disadvantage of the UAVs on the petrol engine is a fire hazard in the event of an accident.

Drones with a hybrid power plant have two types of propulsion:

- Power plant (GE or gas turbine engine, GTE) produces electricity, but in creating the thrust is not involved (hidden in the fuselage).
- The motor or turbine twists the propeller and generator.

The developers of Pegasus Aeronautics give the following example: drone DJI S1000 has a maximum take-off weight of 11 kg and uses 6S LiPo battery with weight 1.5 kg, with capacity of 16 Ah and can carry up to 5 kg of payload for 15 min. If we replace the electrical battery with generator GE-30 Range Extender with equivalent capacity 128 Ah and weighs just 0.45 kg more, will allow DJI S1000 flying time within 2 h with payloads up to 4 kg [4].



Technical Specifications:

- Base Weight: 2.60 kg
- Max Continuous Power Output: 2 000 W
- Max System Output: 4 000 W
- Operational Voltage: 24 V (6S) through 50 V (12S)
- Cooling: Liquid-Cooled, External Radiator
- Starting Method: Self Starting
- Fuel Delivery: Fuel Injected, ECU Controlled
- Interface Protocol: CAN, Serial
- Initial Time Between Overhaul: 200 h.

Fig. 1. GE-30 Range Extender

The "Year!" is the first quadcopter (Table 1) with control of 4 combustion engines (4 DHS) that can be controlled with the accuracy of an electric engine. Unfortunately, combustion engines are not very dynamic. The electric hub shaft is able to start the combustion engine from a small on-board battery. While in flight, it buffers the energy resulting from slowing down the engine and puts it on disposal again if acceleration is needed. Thus, one can end the flight with almost full battery. Malfunctioning of combustion engines or a controlling unit is swiftly compensated for. UAV "Year!" has built-in octocopter safety inside the quadcopter. The safe landing is guaranteed in contrast to conventional quadcopters with electric engines only [5].

Table 1. Technical Specifications of quadcopter "Year!"

Weight	4.9 kg empty weight
Payload	5.0 kg peak load, 3.0 kg nominal load
Speed	100 km/h maximum speed
Range	55 km maximum range
Fuel	1.5 l fuel tank, 25:1 gas/oil ratio
Engines	Engines with 4×1.6 kW maximum power (1 kW combustion engines plus 600 W BLDC engines). Combustion engine (two stroke with ignition) has 12 000 rpm. Self controlled engine start with running control for the combustion engines. The LiPo Battery for starting the combustion engine has 4S, 1250 mA/h

DHS with name "H2 UAV Generator" are presented in (Table 2), with 5 times more range and 5 times longer flying time. This DHS consist of: engine, generator with 24 coils and battery, 1 default fuel tank 3.5 and LiPo Battery 4S 1.8 Ah 75 C. "H2 UAV Generator" has a word record of 2 h with 3 kg payload [5]. Hexacopter Gaya 160 Hybrid with "H2 UAV Generator" have range 100 km and flying time 3 h is suitable for power line inspection and mapping industry [6].

Table 2. Drone Hybrid System - "H2 UAV Generator"

Weight	4.0 kg w/o Accessories and 5.2 kg Total
Power	1.8 kW Continuous / 2.0 kW Max. Power
Dimension (L × W × H)	260 × 1312 × 325 mm
Applicable UAV Types	Multicopters and VTOL Fix-wings
Max. Take-off Weight	18 kg or UAV suggested
Output Voltage	12 S (49 V +/- 1 V)
Fuel consumption	750 g/kw • h (hovering 1.5 L/h)
Service Temperature	- 20 to + 40 °C
Ceiling (above the sea)	2000 m

The "Russell Engine/Generator" (Eng/Gen) is a unique DHS design that offers extreme power density and high efficiency, united with a built-in, large diameter, high efficiency electric generator [7]. Its advantages are: vibration free operation, no torque transferred outside the Eng/Gen case, and sealed construction (waterproof and dustproof). This design reduced internal friction losses, due to: two cycle piston movement; low number of moving parts and low RPM operation. The weight of this Eng/Gen is 45 % of a conventional diesel engine with generator and all related ancillaries. The term 4×2 relates to a design with 4 cylinders (each firing 2 times in the course of a single revolution) has generator output 73.6 kW and operating speed 1200 rpm. The "Russell Eng/Gen" is predicted to a power density of 100 kW/l which compares with 50–60 kW/l for typical four stroke automobile engines [7].

2. Materials and methods

Electrical machine is an electromechanical device designed to convert either mechanical energy to electric (electric generator), or electric energy into mechanical (electric motor). The principle of operation of electric machines is based on the laws of electric and magnetic phenomena: the electromagnetic induction law and the Ampere law. The essence of the law of electromagnetic induction as applied to electric machine is that when a conductor moves in a magnetic field with velocity \mathbf{v} in directions perpendicular to the vector of magnetic induction \mathbf{B} , there is induced electromagnetic field \mathbf{E} :

$$(1) \quad \mathbf{E} = \mathbf{B} \cdot \mathbf{l} \cdot \mathbf{v},$$

where l is the active length of the conductor, i.e. a part of its total length, in the magnetic field.

If the conductor is closed, an electric current I will appear in it. As a result of the interaction of this current with an external magnetic field, the electromagnetic force F_{em} will act on the conductor, which is determined by the Ampere law:

$$(2) \quad F_{em} = \mathbf{B} \cdot \mathbf{l} \cdot \mathbf{I}.$$

With uniform motion of the conductor, the forces F acting on the conductor are equal to F_{em} . Multiplying both sides of the equality by the velocity of the conductor \mathbf{v} , we obtain equality [8]:

$$(3) \quad \mathbf{F} \cdot \mathbf{v} = \mathbf{B} \cdot \mathbf{l} \cdot \mathbf{I} \cdot \mathbf{v} = \mathbf{E} \cdot \mathbf{I}.$$

The left-hand side of (3) determines the value of the mechanical power expended on moving the conductor in a magnetic field; the right part - the value of the electric power, developed in a closed loop by an electric current. Electrical

machines can be multi-phase or single-phase. Asynchronous machines, depending on the design of the winding of the rotor, can be fitted with a short-circuited or phase rotor. Synchronous machines and collector machines with constant current, depending on the way in which they create the magnetic field are two types - with winding excitation and with permanent magnets.

The efficiency can reach significant values: in machines with a very large unit capacity, it can reach 99.5 %, in machines of medium power 70–90 %. The exception is electric machines of low power (not exceeding a few hundred Watts), the efficiency of which can be from 20 to 60 %. To improve the technical parameters of electric generators, PM are used, based on rare-earth NdFeB magnets. They have residual magnetic induction $B_r = 1.2\text{--}1.45$ T and operating temperatures up to 150 °C. Electric generators with PM have several advantages:

- The possibility of obtaining high values of the longitudinal component of the magnetic induction in the working gap,
- Contactless and lack of nodes that require maintenance. The absence of sliding electrical contacts significantly increases life and reliability in comparison with electric generators of direct current and synchronous generators,
- High efficiency,
- High specific indicators for the developed power per unit of weight.

Direct connection without a reducer greatly simplifies the design and provides a long life and low weight. At a wind with speed of 13 m/s on the shaft of one windmill, a power of about 0.95 kW was obtained (from surface 1 m² was obtained 300 W). When the rotational speed is 100–150 rpm, slow-moving multi-pole electric generators on permanent magnets are used [9]. In the boring of the stationary part of the asynchronous motor – stator, there is a rotating part of the motor – a rotor, consisting of a shaft, a core and windings. The winding of the rotor is a short-circuit structure consisting of several aluminum rods (in example with number 8), located in the longitudinal grooves of the rotor core and closed on both sides. The results of calculating the magnetic field and moments for three models of electric motors with permanent magnets are considered. It is shown that the configuration of the magnetic system has a significant effect on the torque characteristics of the electric motor [10]. The rotors in Model 1, are made in the form of an 8-pole, Model 2: 8-pole and for Model 3: 4-pole magnetic system. All three models of three-phase motors have stator phases included as follows: A (+), B (0), and C (-). Switching phases of the motor must be from three non-contact sensors. Every 15° for Model 1 and 2, and every 30° for Model 3 there is a change in the status of sensors and a command is issued to enable the respective phases of the motor. Algorithm switching is: A (+), B (0), C (-); A (+), B (-), C (0); A (0), B (-), C (+); A(-), B(0), C (+) and thus, within the zone switching includes only two phases in accordance with a predetermined algorithm. Switching zone 1 is equal to 15° (corresponds to the 8-pole models) and the area switching 2, is equal to 45°. In the commutation zone, the torque for Model 1 is 52 Nm, for Model 2,

46 Nm and for Model 3, 25 Nm. The mass of magnets is $M1 = 2.88$ kg, $M2 = 2.1$ kg and $M3 = 1.05$ kg. Comparing Models 1 and 2, increasing the mass of magnets for 1.37 times allowed increasing the torque only by 1.1 times. For the purpose of limiting tooth pulsations, various methods are used. One of them is the execution of the bevels on the rotor. Another way to reduce the magnitude of the pulsation of the electromagnetic moment is the profiling of the ferromagnetic poles according to a predetermined law or the shaping of the special shape of the poles on the rotor [10].

Asynchronous and reluctance machines can also be used for generating. Vehicle generators can be used to add torque for motoring as well. Traction motors can be used as generators during braking to convert kinetic energy to electrical energy. Asynchronous traction motor is used also for braking. Claw Pole alternator is the most popular-over 80 million produced in 2014 (not counting trucks). SR machines can be used as generators but the regulation of the voltage is more complex than the other machine types. Electric machines power density comparison: TESLA - 4.5 kw/kg, BMW i3 – 2.5 kw/kg, Siemens Aero PM motor – 5 kw/kg. Permanent magnets can only produce a maximum flux density of 1.4 T. Soft materials (electrical steels) become saturated at maximum flux densities in the range of 2.1 to 2.4 T. When number of stator poles is doubled, the back iron flux is cut in half. Yoke thickness and stator overall diameter (OD) increases with decreasing pole numbers with a fixed stator slot depth and rotor OD (the example on Fig. 2 is with fixed rotor diameter which reduces the stator OD) [11].

On Fig. 3 are given 4 most popular motor-generators machines – RSM, SRM and PM machines typically utilize boost converters for voltage, frequency and power regulation. SR machines can be used as generators but the regulation of the voltage is more complex than the other machine types [11]. Hybrid Starter Generator (HSG) are used in new cars - Sonata, KIA Optima Hybrid. Toyota 2004 Prius has separated PM synchronous generator and PM synchronous traction motor on the same motor shaft. Toyota 2010 Prius has PM generator 12 slot, 8 IPM poles, V shaped [12].

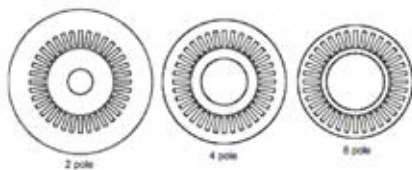


Fig. 2. Yoke thickness and stator versus stator pole

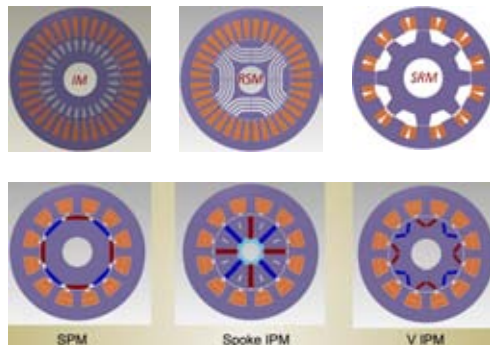


Fig. 3. Generators with three phase stators

To improve drive train availability for applications in electric vehicles, the article proposes the design of 6-phase permanent magnet machine as two independent 3-phase windings, Fig. 4. A number of possible phase shifts between two sets of 3-phase windings due to their slot-pole combination and winding configuration is investigated and the optimum phase shift is selected [13]. The 6-phase motor can operate as a single unit, in which the stator windings are excited with 6-phase balanced sinusoidal currents of the same magnitude and frequency but having a phase shift of 60° electrical with respect to each other. However, 6-phase motor can also be controlled as two separate and independent three-phase systems. Each set of the three-phase system is excited with 3-phase balanced sinusoidal currents of the same magnitude and frequency but having a phase shift of 120° electrical with respect to each other [13].

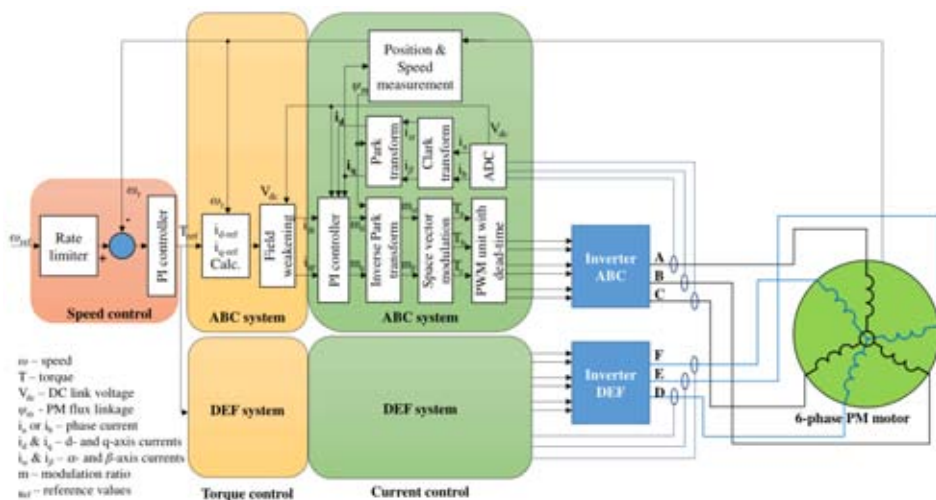


Fig. 4. Schematic of inverter control system having independent control for both set of three-phase system of six-phase permanent magnet machine

Here are presented the equations of the main parameters needed in the modelling of double-star PM machines. In a magnetically linear system (stator), the self-inductance L of a winding is the ratio of the flux ψ linked by a winding to the current I flowing in the winding with all the other winding currents zero. The self-inductance of a winding i can be expressed as follows [17]:

$$(4) \quad L_i = \psi_i / I_i.$$

Similarly, the mutual inductance linking the windings i and j results in the following expression:

$$(5) \quad M_{ij} = \psi_j / I_i .$$

The PM machines with buried magnets correspond to salient pole machines, in which the inductances depend on the rotor position. In such machines the fundamental wave of the self-inductance of a stator winding varies by $2\theta_e$. The dependency can be taken into account in the analytical expression of inductances with an inverse air-gap function. The inverse air-gap function is expressed with the following approximation [17]:

$$(6) \quad g(\varphi_s - \theta_e)^{-1} = \epsilon_1 - \epsilon_2 \cdot \cos(2\varphi_s - 2\theta_e).$$

$$(7) \quad L_i = \mu_0 \cdot r \cdot l \int_0^{2\pi} N_i(\varphi_s)^2 g(\varphi_s - \theta_e)^{-1} d\varphi_s ,$$

where l is the stack length, r is the effective radius of the stator bore, and μ_0 is the permeability of vacuum ($4\pi 10^{-7} \text{Vs/Am}$). The mutual inductance linking any two stator windings i and j can be expressed similarly where φ_s is the stator circumferential position and θ_e is the rotor position. The variables ϵ_1 and ϵ_2 , defined with the help of the minimum and maximum air-gap lengths g_{min} and g_{max} , respectively. According to [17] the torque characteristic of a multiphase machine, the armature of which consists of two three-phase winding sets having a displacement of 30° between the sets, is substantially better than for 0- or 60° -degree displacements. Moreover, by supplying the two three-phase sets displaced by 30° with two three-phase inverters instead of one set and one inverter, the amplitude of the pulsating torque component was reduced and the frequency was shifted to 12 times the supply frequency [17]. In [14] it is describes the development of new winding configurations for 6-phase permanent magnet (PM) brushless machines with 18-slot, 8-pole, that eliminate and/or reduce undesirable space harmonics in the stator magneto motive force, see Fig. 5 and Fig. 6.

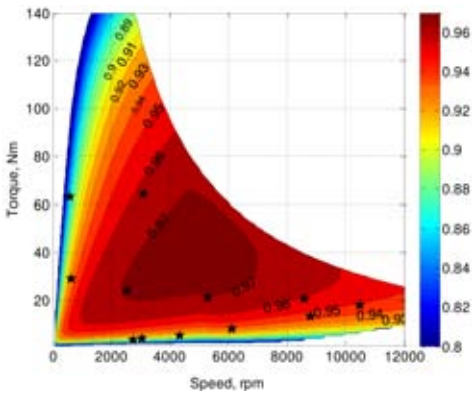


Fig. 5. Predicted efficiency map of optimized 6-phase, 18-slot, 8-pole IPM motor

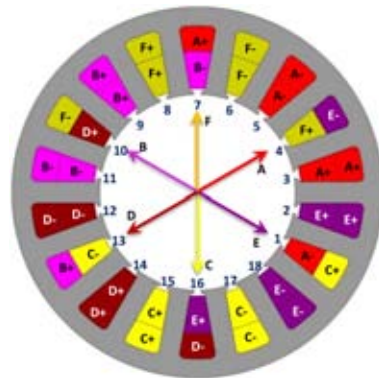


Fig. 6. Schematic of 6-phase, 18-slot, 8-pole winding configuration

The automotive industry is producing new Hybrid Electrical Vehicles (HEV) and pure Electric Vehicles (EV). Simulation of the BMW i3 Traction Motor is given on Fig. 7, with software MotorSolve [15]. It is assembled data from the Oak Ridge National Laboratory (ORNL) and from BMW to develop a MotorSolve model of the 2016 BMW i3 traction motor. The 2016 BMW i3 traction motor is a 12 pole/72 slot motor with an IPM rotor, rated at 125 kW. The rotor was designed to have a high saliency ratio; correspondingly the reluctance torque component was high as a consequence. It was also designed to have a very sinusoidal back EMF which is rare in motor designs.

Software analysis of the 2010 Toyota Prius Traction Motor (60 kW, rotation speed 13 500 rpm) can be modeled by importing a CAD created rotor DXF file in MotorSolve or in MagNet (Fig. 8). The performance of the magnetics within a motor the Toyota 2010 Prius is 37.5 mV rms per 1 rpm. At 4 000 rpm this is 150 V rms. MotorSolve predicts the Back EMF within 2 % of the measured values [16]. Toyota Prius 2010 PM generator 42 kW have 12 stator slot, 8 IPM poles (V-shaped), rotor mass is 3.93 kg and stator mass 8.53 kg. Bi-directional dc-dc converter, for Prius 2010 PM generator, has the following parameters: 200 Vdc, 27 kW. Battery is fan cooled, Ni-Mh with 201.6 Vdc and 6,5 Ah. It is given comparison between Specific power density of current piston engines, turbines and electric motors, Fig. 9 [16].

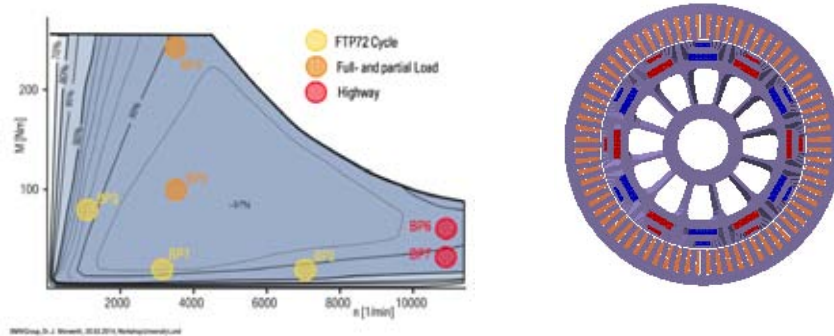


Fig. 7. Efficiency of BMW i3 traction motor with IPM rotor

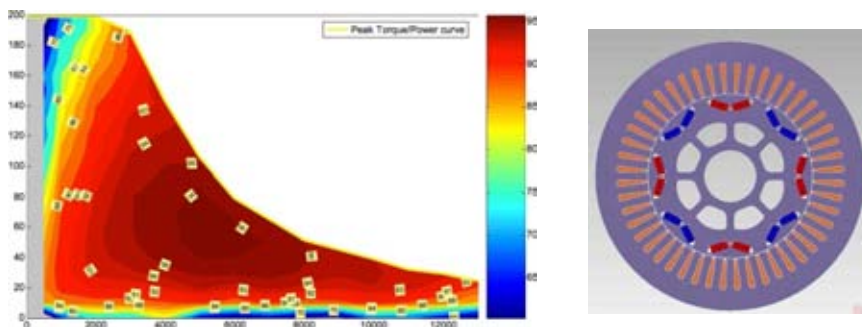


Fig. 8. Efficiency of Toyota traction motor with IPM rotor

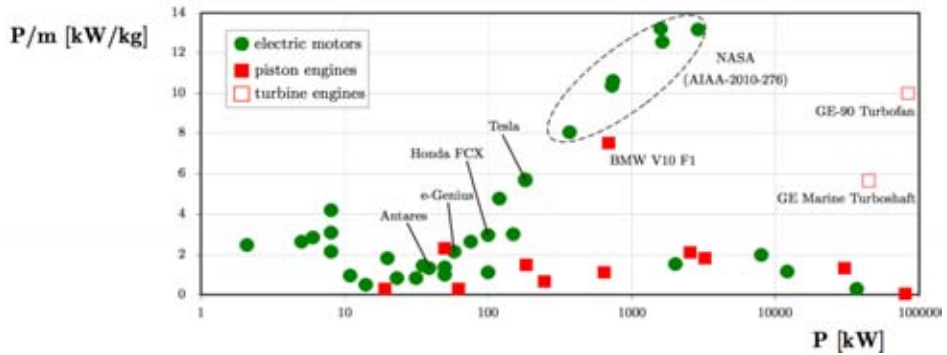


Fig. 9. Specific power density of current piston engines, turbines and electric motors

3. Results

A purely electric UAV, (VTOL type), designed with 5 electric motors (4 for vertical take-off and 1 for horizontal flight) is the objective of this work. The capabilities of without doubt helicopters are more versatile than fixed-wing and vertical take-off and landing (VSTOL) aircraft, when it is required to switch between several flight modes during a mission. The efficiency of VTOL aircraft during hovering is much less than helicopters due to the relatively small effective rotor area. The electric UAV is for a flight mission where the cruise time is much greater than the hover time pointing the choice towards a VSTOL aircraft, which can be thought of as a cross between a rotary and fixed-wing UAV. At least half the loiter energy of the electric UAV (E UAV) is required for the hybrid-electric UAV, one half of the E UAV battery is replaced by the hybrid-electric UAV propulsion weight and fuel. The lighter the propulsion weight, the more fuel can be put onboard and hence the more total energy is available on-board. As can be seen from Fig. 6, when the propulsion is one-third of the total E UAV battery weight, the total energy on-board is over three times that of the E UAV [18]. The generator S676-500U-01 has a mass of 1.15 kg and rated power is 2 250 W at 7 500 rpm. He will supply electric motor U8 kv170, with a mass of 5×0.242 kg, $1300 W_{max}$ for propeller. The O.S. 46FX is a glowplug reciprocating engine, with 1.39 kW/kg, at 17 000 rpm, with mass of 1.66 kg, $2\ 307 W_{max}$. The battery is with nominal voltage of 22.2, 8 Ah, with mass of 1.66 kg. If the multicopter with target mass 11.2 kg flight is only with battery, endurance is 38 min. But with DHS on board, with fuel 2.21 l, endurance is 61 min [19].

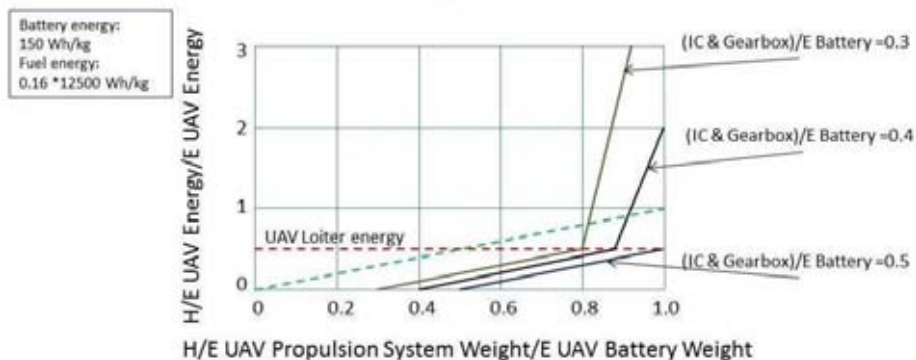


Fig. 10. Propulsion system considerations

4. Discussion

It was selected circuit with 6 rectifiers, (Larionov star, six-pulses), which will give for a 3-phase system a voltage absolute pulsation amplitude of 14 %. For the selected 6-phase permanent magnet generator, 12 rectifiers (two Larionov star, twelve-pulses, in the serial inclusion) will give pulsation 4 %.

References

1. Этот гибридный дрон установил новый неофициальный рекорд длительности полета. <https://lenskii.ru/technologies/gadgets/etot-gibridnyj-dron-ustanovil-novyj-neofitsialnyj-rekord-dlitelnosti-poleta/> (available online: 17 September 2017)
2. HYCOPTER. <https://www.h3dynamics.com/products/hycopter/> (online accessed: 10 January 2018)
3. HYBRiX.20: гибридный квадрокоптер установил рекорд по продолжительности полета. <https://dronomania.ru/news/hybrix-20-gibridnyj-kvadrokofter-ustanovil-mirovoj-rekord-po-prodolzhitelnosti-poleta.html> (online accessed: 10 January 2018)
4. GE35 Range Extender. <http://www.pegasusaero.ca/ge35-range-extender>
5. year! Table of Specs. <http://www.year.de/specs/> (online accessed: 10 January 2018)
6. Richen Power. H2 UAV Generator. <http://www.richenpower.com/uploads/file/H2en.pdf> (online accessed: 10 January 2018)
7. Russell Energy Corporation. URL: <http://www.russellenergy.com/includes/business-opportunity.php> (online accessed: 10 January 2018)
8. Кацман, М.М. Справочник по электрическим машинам: Учеб. пособие для студ. образоват. учреждений сред. проф. Образования - М.: Издательский центр «Академия», ISBN 5-7695-1686-0, 2005, с. 480.
9. Гребеников, В.В. Электрогенераторы с постоянными магнитами для ветроустановок и микро-ГЭС, УДК 621.313.17, Гідроенергетика України, ISSN 1812-9277, 1/2011, с. 43–48.

10. Гребеников, В.В., М.В. Прыймак, Исследование влияния конфигурации магнитной системы на моментные характеристики электродвигателей с постоянными магнитами, *Электротехника та електроенергетика*, 2009, 2, 57–60. ISSN 1607-6761, URL: <http://elcut.ru/publications/grebenikov1.pdf>
11. Hendershot, J.R., WORKSHOP Generator designs including choices for hybrid vehicles, CWIEMIE Chicago, 4-6 October 2016, DESC Chicago. https://www.coilwindingexpo.com/chicago/___media/pdfs/jim_hendershot_wed_5th_october.pdf (online accessed: 10 January 2018)
12. Hendershot, J.R., Designing a PM Generator for a hybrid vehicle with MotorSolve, 8-10 November 2016, Aria Resort and Casino, Las Vegas. <https://www.infolyticaengage.com/wp-content/uploads/2017/01/Design-a-PM-Generator-by-J-Hendershot.pdf> (online accessed: 10 January 2018)
13. Patel, V.I., J. Wang, et al., 6-phase Fractional Slot per Pole per Phase Permanent Magnet Machines with Low Space Harmonics for Electric Vehicle Application, 2014, 50, 4, 2554–63. ISSN 0093-9994. DOI: 10.1109/TIA.2014.2301871
14. Patel, V.I., J., Wang, D.T., Nugraha, R. Vuletic, and J. Tosen, Enhanced availability of drivetrain through novel multiphase permanent-magnet machine drive, *IEEE Transactions on Industrial Electronics*, 2016, 63, 1, 469–480. ISSN 0278-0046 DOI: 10.1109/TIE.2015.2435371
15. Simulation of the BMW i3 Traction Motor. <https://www.infolytica.com/en/applications/ex0214/> (online accessed: 10 January 2018)
16. Hendershot, J.R., Motor Solve analysis of the 2010 Toyota Prius Traction Motor, Hilton Rosemont, Chicago O'Hare, 27 October 2015. https://www.infolytica.com/Images/applications/engage2015/JamesHendershot_Prius.pdf (online accessed: 10 January 2018)
17. Kallio, S., Modeling and Parameter Estimation of Double-Star Permanent Magnet Synchronous Machines, Lappeenranta University of Technology, ISBN 978-952-265-563-9, ISBN 978-952-265-564-6 (PDF), ISSN-L 1456-4491, ISSN 1456–4491, Lappeenranta 2014, 68 p.
18. Jaeger, M., D. Adair. Conceptual design of a high-endurance hybrid electric unmanned aerial vehicle, 11 p. DOI: 10.1016/j.matpr.2017.04.018 (available online: 20 June 2017)
19. Donato, T., L. Spedicato, and D. Pio Placentino, Design and performance evaluation of a hybrid electric power system for multicopters, *Energy Procedia*, 2017, 126, 1035–42. DOI: 10.1016/j.egypro.2017.08.310

ЕЛЕКТРИЧЕСКИ МОТОР-ГЕНЕРАТОРИ ЗА БЕЗПИЛОТНИ ЛЕТАТЕЛНИ СРЕДСТВА

П. Граматиков

Резюме

В настоящата статия се разглеждат устройството и принципа на работа на съвременни електрически мотор-генератори, подходящи за използване в различни по размер и конструкция безпилотни летателни средства. Предложеното решение за използване на двигател с вътрешно горене за стопроцентно захранване на всички бордни електрически мотори за създаване на подемна сила за вертикален и хоризонтален полет може да се използва в хибридни БЛА, при което времето на полет се очаква да се увеличи 2 до 4 пъти, в сравнение с това при използване само на електрически батерии. Предлага се електронният контролер на мотор-генератора да обезпечи работа му в режим стартер и режим производство на електроенергия. Посочени са софтуерни продукти за компютърна симулация на процесите в електрическите мотор-генератори.

ONBOARD DIGITAL BLOCK FOR ELECTRIC FIELD MEASUREMENTS IN SPACE

Boris Hotinov, Pavlin Gramatikov

*Space Research and Technology Institute – Bulgarian Academy of Sciences
e-mail: bmh@space.bas.bg, pgramatikov@space.bas.bg*

Abstract

The article presents a Bulgarian digital block in a Bulgarian device – Analog Measurement of Electric Fields-Wide Band (AMEF-WB). This on-board instrument with 4 sensors was developed to measure electric fields in a wide frequency range. The measurement of the electromagnetic fields and plasma parameters are in compliance with the science purpose and technical tasks of the space experiments project RESONANCE. This block is a part of a scientific satellite instrument for electric fields amplitude and frequencies measurements from quasi constant DC up to 1 MHz. The device AMEF-WB give signals in 3 different frequency bands for processing by the external receivers ELMAWAN (Czech Republic) and HFA (Poland) from the composition of the wave complex.

1. Introduction

In the field of space technologies, for the RESONANCE project [3, 5] with high-apogee satellites Fig. 3 [2], was developed a new Bulgarian device AMEF-WB [4] for measurement of parameters of space plasma. The device was designed to study electromagnetic fields and interactions of waves and particles in the inner magnetosphere of the Earth. The Earth and Jupiter are well known as radio planets that are emitting very intense and coherent radio wave emissions. The Earth's auroral radio emissions, recorded by INTERBALL-1 satellite [12], also called auroral kilometric radiation – AKR, were observed by space-borne satellites and ground-based stations [8]. Radio emissions were also recorded by the DEMETER/ICE (Instrument Champ Electrique) experiment [9, 10]. This instrument measures the electric field components of electromagnetic and electrostatic waves in the frequency range from DC to 3.25 MHz [10]. Despite the limited satellite invariant latitude (data acquisition below $\sim 65^\circ$), specific events have been observed, close to the sub-aurora region, in the frequency range from 100 KHz to about 1 MHz [9, 10]. Van Allen probes A EMFISIS electric field intensity spectra 30 Hz÷500 KHz are shown during a period following the 17–18 March 2015 great storm in Plasmapause, $L = 2.4\div 4.4$ [13].

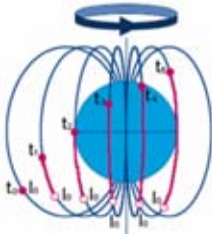


Fig. 1. Magneto-synchronous orbits of the RESONANCE project

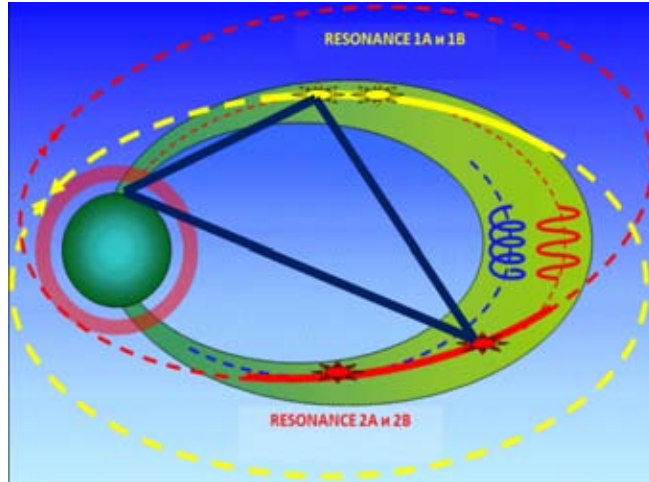


Fig. 2. Measurements with two pairs of satellites of the RESONANCE project

On Fig. 2 [2], is given the strategy for the measurements with two pairs of satellites. The dotted yellow curve is the orbit of the first pair of satellites (1A and 1B), the solid yellow line is the part of the orbit inside the selected power tube; red colored line – the same for the second pair of satellites (2A and 2B); dark blue line – the basic distance for ultra-low frequency (ULF) interferometer.

In the RESONANCE project, the task is to carry out non-linear and non-stationary processes in magnetosphere. ELMAWAN is a multi-component low-frequency receiver in the frequency range of 20 Hz ÷ 20 KHz. But, a high frequency analyzer (HFA) task is to study an AKR. The main tasks of RESONANCE experiment are the study of choral radiation in the equatorial region and various signals in the auroral region. Measurement of density and temperature of electrons will be performed by the device based on modified Langmuir probe. Prototypes of this device, such as KM (KM-7 on the satellite of the AURORAL PROBE), was repeatedly used in the space project and worked well. The satellites for the RESONANCE project will operate in pairs in intersecting elliptical orbits of 500 km × 28 000 km at an inclination of 63.4° [1]. On Fig. 1 [2] is depicted the principle of construction of the power line magnetic field correction, together with the Earth, in different points in time (t_1, t_2, \dots). The actual position of the satellite at each moment of time is marked by red circles, and the initial position is marked with white circles. It is possible to pick up parameters of an

orbit so that the satellite, on the one hand, is connected together with the Earth, and, at the same time, moves along the chosen power line of a magnetic field.

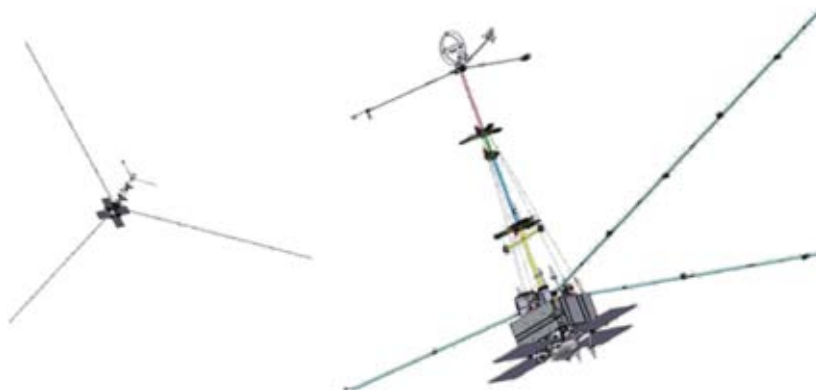


Fig. 3. A pair of satellites from RESONANCE project in flight configuration [2]

2. Materials and methods

The digital block, Fig. 5 (from device AMEF-WB, Fig. 4) consists of a galvanically separated analogue and digital part. The analogue part includes a 16-bit analog to digital converter (ADC) with 6 simultaneous inputs and a variable input range. Four of its entrances convert the electric fields with variable gain*4 through low-pass filters (LPF). Variable gain*2 of the ADC coupled with the assigned input range results in an increase in the dynamic range by 3 bits (plus 16 bits from ADC resulting in 19 bits). The data is measured 25 times in 1 s with a bandwidth from DC to 10 Hz. To control the operation of the device 16 slow values are measured: 6 temperatures and 10 supply voltages. From the measured values of the electric fields, a correction voltage DAC_{out} is calculated and output via two digital to analogue converter (DAC), which compensates for the polarization of all electric sensors (ES) [5, 6].

When shutdown protection of the central processing unit (CPU) is on (CPU stops transmitting signals) the polarizing voltage is reset to a further circuit, so that other devices using high frequency bands can continue to operate. Galvanic separation is performed through Analog Devices, Inc., iCoupler® technology integrated circuits that allow data transfer up to 10 Mb/s. The time of the measurement cycle is 40 ms, while four electrical field signals and two control signals are simultaneously measured. The collected data is collected in a total block of 224 bytes in length and sent over the communication channel by a signal from the on-board apparatus. As a backup, serial flash memory is provided in case of storage of large data for more than 4 h of measurements.

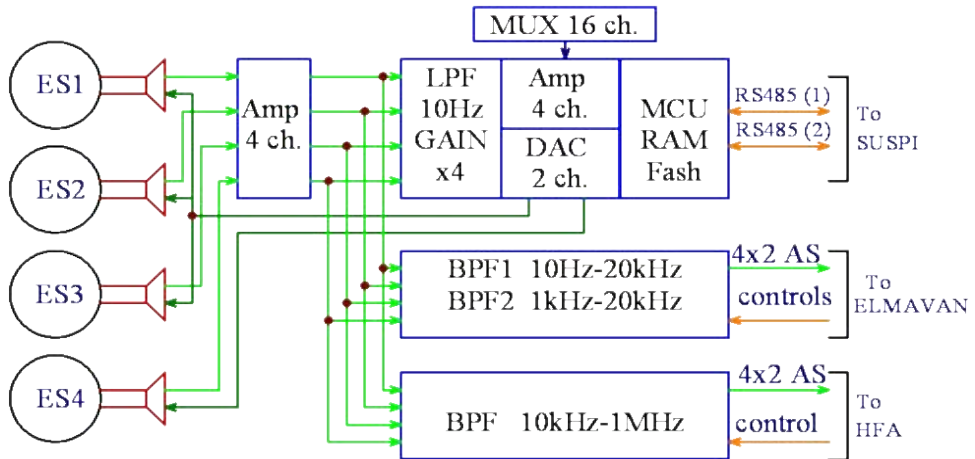


Fig. 4. Device AMEF-WB from RESONANCE project

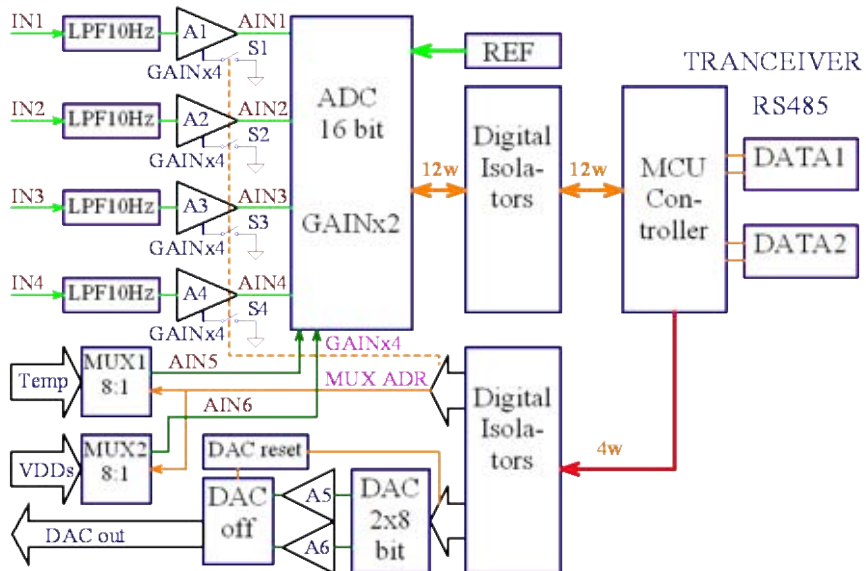


Fig. 5. Digital block from device AMEF-WB from RESONANCE project

2.1. Analogue part

For 16-bit ADC is used a chip with simultaneous converting bipolar inputs, manufactured by Analog Devices, Fig. 5. This allows at the same time measurement of the 4 wave inputs from the ES. The other two inputs measure 8 multiple values via MUX1 and MUX2. Through them is measured 6 temperatures: 4 from ES1, ES2, ES3, and ES4; 1 from the power supply unit and 1 from the digital unit. Power supplies are also measured. The ADC has a variable input gain*2, which extends the dynamic range of the input value conversion. The measurements are controlled by CPU. They are transmitted through a serial synchronous interface (SPI) [7].

The four analog signal inputs have one filter LPF-10 Hz which limits the input bandwidth to 10 Hz to ensure proper waveform measurement. The variable amplifiers with gain*4 are used to increase the input dynamic range. They are controlled by one chip with electronic switches. ES4 has a different gain compared to the ES1, ES2 and ES3 because of its shaded.

The accuracy and repeatability of the measurements is referenced by a precision reference voltage source of 2.5 V. Temperature measurement of the board are used for self-analyze the work of the board and eventually make adjustments to the data outputs.

To counteract the polarization of sensors, is used a DAC-voltage to symmetry them to the area around zero. That way is avoided the out of range output of the ES-signal. In this case is used one chip, 8 bit DAC. It is managed by the CPU through the SPI interface. The value is set according to the constant component of the measured inputs. Voltage correction for ES4 is operated differently from the ES1, ES2, and ES3 due to its shadowed position to the Sun.

2.2. Digital part

The digital part is galvanically isolated from the analogue part, to reduce harmful interference by integrated circuits. The allowed data transfer is up to 10 Mb/s [7].

A processor with own flash memory is used for the programs and is programmed on the board (Fig. 5). This CPU supports SPI interface for ADC and DAC. It has a built-in 2 serial communication interfaces. It uses a flash memory to save the settings. The CPU uses an random access memory (RAM) to collect the measured data in the sending blocks.

Duplicated RS485 serial interface is used for data exchange with control scientific equipment (CSE). It has a place for a high capacity 4÷8 MB (or 32÷64 Mb) serial flash memory to keep collected blocks for 4.5÷9 h in the event of an interrupted connection.

3. Results

The memory blocks consist of: an identifying header, next number, status and error codes, information section with data from the measurement of the input quantities, and slow voltage and temperature control measurements. The total block size is 224 Bytes per 1 second measurement. For each block, in order to recover properly the input values the amplifier gains and the input range of the ADC are recorded. The communication block can have up to 3 changes per second. Similarly, polarizing voltage corrections are recorded. The Bulgarian side provided in 2013 in the city of Moscow, a complete set of the technological copy: device AMEF-WB, sensors for electric field and control measuring equipment (CME). A full device test was performed for more than 2 years in *Lavochkin* Research and Production Association (or shortly *Lavochkin* Association, LA) a Russian aerospace company and Space Research Institute of the Russian Academy of Sciences (SRI-RAS).

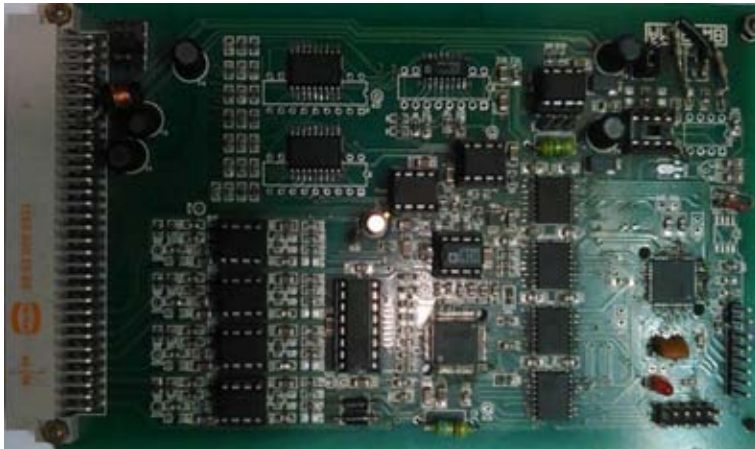


Fig. 6. Digital block for space electric field measurements

The device can be improved by using new electronic parts and by alteration of functional scheme. This is a preliminary study for next developments.

4. Discussions and Conclusions

The AMEF-WB is a 3-components (X, Y, Z) receiver of extremely low frequencies (ELF) space electric field. For high frequency electronic capacity suppression is applied in electric fields sensors. That and CPU control allows to use instruments in the entire frequency range from DC to 1 MHz electric fields.

References

1. The Internet site on Project Resonance: http://space.skyrocket.de/doc_sdat/rezonans.htm
2. Могилевский, М.М., Л.М. Зеленый, А.Г. Демехов, С.А. Немыкин. Изучение процессов во внутренней магнитосфере Земли: спутниковые и наземные измерения. В: Вторая научная конференция "Базы данных, инструменты и информационные основы полярных геофизических исследований", ИЗМИРАН, 22–26 мая, 2012, 15–18.
URL: http://www.ikfia.ysn.ru/images/doc/publication2013/Tezis_dokladov%20_2012_RUS.pdf
3. The Internet site on SRI-RAS for Project RESONANCE. <http://www.iki.rssi.ru/resonance/karta.html> (last day accessed 10 December 2017).
4. The Internet site of Scientific and Industrial Association named after S.A. Lavochkin. <http://www.laspace.ru/projects/information-systems/resonance/> (last day accessed 10 December 2017).
5. Бойчев, Б., М. Могилевский, Г. Беляев, Б. Хотинев, Т. Романцова, В. Бойчев, К. Методиев, П. Граматиков, Г. Сотиров, О. Сантолик, И. Колмашова, Л. Углирж, Й. Баше, Е. Мацушова, З. Хрбачкова, Я. Хум, Ф. Грушка, Р. Лан, Д. Чугунин, Эксперимент по измерению электрических полей в широком диапазоне частот АМЕФ-WB/ИЭСР-3Р и анализатор электромагнитных волн ELMAVAN для проекта РЕЗОНАНС, Space, Ecology, Safety - SES`2012, 4–6 December 2012, Sofia, 119–125, ISSN1313–3888.
6. Бойчев, Б., М., Могилевский, Г., Беляев, Б., Хотинев, Г., Сотиров, К., Методиев Сензори за измерване на електрични полета в йоносферата и контролно измервателна апаратура за тях. В: Юбилеен международен конгрес "Наука образование, технологии "40 години България –космическа държава", 12–14 септември 2012 г., Варна, Том 1, 131–144, ISBN 978-954-577-636-6.
7. Boychev, B., M. Mogilevsky, G. Belyaev, B. Hotinov, V. Boychev, and T. Romantsova. AMEF-WB/ИЭСР-3Р experiment to a measure electric fields in a wide frequency range of the Resonance Project, Scientific Conference on Aeronautics. Automotive and Railway Engineering and Technologies, BulTrans 2012, 26–28 September 2012, Sozopol, Bulgaria, Proceedings, 96–103, ISSN 1313–955X.
8. Boudjada, M.Y., P.H.M. Galopeau, M.M. Mogilevski, A. Lecacheux, V.N. Kuril'chik, and H.O. Rucker. RESONANCE Project: Comparative studies of observational features associated to auroral radio emissions, Resonance Meeting, 1–5 June 2010, Moscow.
9. Boudjada, M.Y., P.H.M. Galopeau, M.M. Mogilevski, S. Sawas, J. Blecki, J.J. Berthelie, and W. Voller. Study of sub-auroral radio emissions observed by ICE experiment on-board DEMETER satellite. EGU General Assembly 2012, Geophysical Research Abstracts, 2012, 14, EGU2012-2774-1.
10. Bertheliera, J.J., M. Godefroya, F. Leblanca, M. Malingrea, M. Menviellea, D. Lagoutteb, J.Y. Brochotb, F. Colinb, F. Elieb, C. Legendreb, P. Zamorab, D. Benoistc, Y. Chapuisc, J. Artrud, and R. Pfaffe. ICE, the electric field experiment on DEMETER. Planetary and Space Science, 2006, 54, 456–471. DOI: 10.1016/j.pss.2005.10.016

11. Mogilevskiy, M.M., T.V. Romantsova, J. Hanasz, T.M. Burinskaya, and R. Schreiber. On the Source of Auroral Kilometric Radiation, JETP Letters, 2007, 86, 11, 709–711. DOI: 10.1134/S0021364007230051
12. Teodosiev, D., P. Nenovski, P. Hristov, R. Koleva, J. Vojta, P. Triska, J. Chum, and I. Shibaev. ULF wave measurements aboard the Magion-4 subsatellite: narrow-band wave events observed in the magnetopause regions, Planetary and Space Science, 2005, 53, 1–3, 317–326. DOI: 10.1016/j.pss.2004.09.058
13. Gombosi, T.I., D.N. Baker, A. Balogh, P.J. Erickson, J.D. Huba, and L.J. Lanzerotti. Anthropogenic Space Weather, Space Science Reviews, 2017, 212, 3–4, 985–1039 DOI: 10.1007/s11214-017-0357-5

БОРДЕН ЦИФРОВ БЛОК ЗА ИЗМЕРВАНЕ НА КОСМИЧЕСКО ЕЛЕКТРИЧЕСКО ПОЛЕ

Б. Хотинов, П. Граматиков

Резюме

В статията е представен българският цифров блок от българския прибор Анализатор на многокомпонентно електрическо поле – широколентов (AMEF-WB).

Цифровият блок е разработен за измерване на космически електрически полета в широк честотен диапазон с помощта на 4 сензора. Измерването на електромагнитните полета и параметрите на плазмата е съобразено с научните цели и техническите задачи на космическите експерименти по проект РЕЗОНАНС. Цифровият блок е част от инструментите на научен спътник за измервания на амплитуди и честоти на електрически полета от квази постоянно напрежение до 1 MHz. Приборът AMEF-WB предава сигнали в 3 различни честотни ленти за обработка от външните приемници ELMAWAN (Чешка Република) и HFA (Полша) от състава на вълновия комплекс.

GENERATING A PULSE-WIDTH MODULATED SIGNAL BY MEANS OF TIMER MODULE INTERRUPT OF PIC18F2550 MCU

Konstantin Metodiev

*Space Research and Technology Institute – Bulgarian Academy of Sciences
e-mail: komet@space.bas.bg*

Abstract

The article hereby examines an approach towards pulse-width modulated (PWM) signal generation by means of PIC18F2550 microcontroller unit (MCU). The proposed technique employs the so-called internal interrupt by timer module. This solution may come into use in process automation as a terminal device, for instance putting in motion a servo motor. Although the MCU provides a hardware PWM module, it is dependant of the crystal oscillator frequency. Most of the time, it is difficult to generate a PWM signal at low frequencies. The proposed solution is shown to be versatile enough and suitable to actuate servomotors widely used in RC hobby activities.

Special attention is given to the MCU software peculiarities. Additional computer simulation has also been made. The used software was MikroC Pro for PIC and Proteus VMS. The proposed solution has been shown to operate with sufficient precision. The source code is also included in the present article.

1. Introduction

As the abstract suggests, the article topic is generating a PWM signal at low frequencies, precisely at 50 Hz. Most of the servomotors used by RC hobbyists nowadays operate at this frequency. The pulse width varies within 1 up to 2 ms. It is found to be difficult for the hardware to generate a PWM signal with aforementioned parameters. For instance, if the instruction clock is provided by a high-speed oscillator at 4 MHz, the PWM signal frequency will vary within 244 Hz to 1 MHz [1], which is quite above the designated value. In fact, the required PWM frequency of 50 Hz is achievable by means of the internal oscillator. The oscillator is capable of providing the MCU with a range of clock frequencies from 31 kHz to 4 MHz [2]. This clock source however is said to be quite temperature dependent and unstable. Given these impediments, developing an alternative technique to implement a PWM signal appears to be necessary.

The main purpose of the present article is to demonstrate the ability of a simple solution to generate a PWM signal at 50 Hz by triggering an internal interrupt from a Timer 1 module. In order to test the source code, a simulation has

been carried out by means of Proteus VMS. A real experiment is also implemented so as to make a comparison.

2. Materials and methods

The electronic circuit consists of minimum required parts that make the MCU running according to Fig. 1, i.e. a high-speed crystal of 20 MHz and 2 capacitors of 15 pF each. These are said to provide the MCU with stable instruction clock of 5 MHz [2]. In addition to it, three servomotors are connected to the MCU for verification reasons.

The program algorithm is following. In order to make sure interrupt occurs every 128 μ s, Timer 1 module is initially set to 0xFD80. This value is repeatedly reset each time Timer 1 overflows. The PWM period is obtained approximately by getting the product of 156 interrupts times 128 μ s equals 19 968 μ s. This value is derived as close as possible for given oscillator clock of 20 MHz and prescaler value of 1:1.

The number of interrupts is committed to a counter. As soon as the counter reaches value of 156, start pulse edge is triggered. The edge is rising for all attached servomotors. The falling edge is triggered afterwards depending upon what amount each motor has been assigned to. For instance, falling edge might occur after 12 interrupts times 128 μ s each or 1536 μ s in total. This value denotes the pulse width.

Desired time may be calculated by means of formula:

$$(1) \quad T = (0xFFFF + 1 - TMR1) \frac{4}{F_{osc}} \text{Prescaler}, \quad [s]$$

where TMR1 is initial Timer 1 value, hex, and F_{osc} is crystal oscillator frequency, Hz. In current case study, $TMR1 = 0xFD80$, $F_{osc} = 20E+06$ Hz, Prescaler = 1. Hence, for interrupt period it yields $T = 128 \mu$ s.

The proposed circuit has been put to the test as follows. Three servomotors are connected to the MCU. Each of them is controlled separately. Therefore, each servo is expected to rotate at different angle according to duty cycle value of the fed PWM signal.

3. Results

Having carried out a simulation by means of Proteus VMS, the obtained results are depicted in Fig. 1. Each servo cycles through distinct angular positions in accordance with set value of variables motor 1, 2, 3 in function main, Appendix 1. This value accounts for how many interrupts (128 μ s each) have been triggered. A delay of 500 ms is set between cycles so that each servo has enough time to complete its stroke. All servos operate the way they are expected.

In addition, a real experiment has been carried out by means of HXT 900 Micro Servo 1.6 kg/0.12 s/9 g. There is a full agreement between results obtained by both physical and simulated experiments.

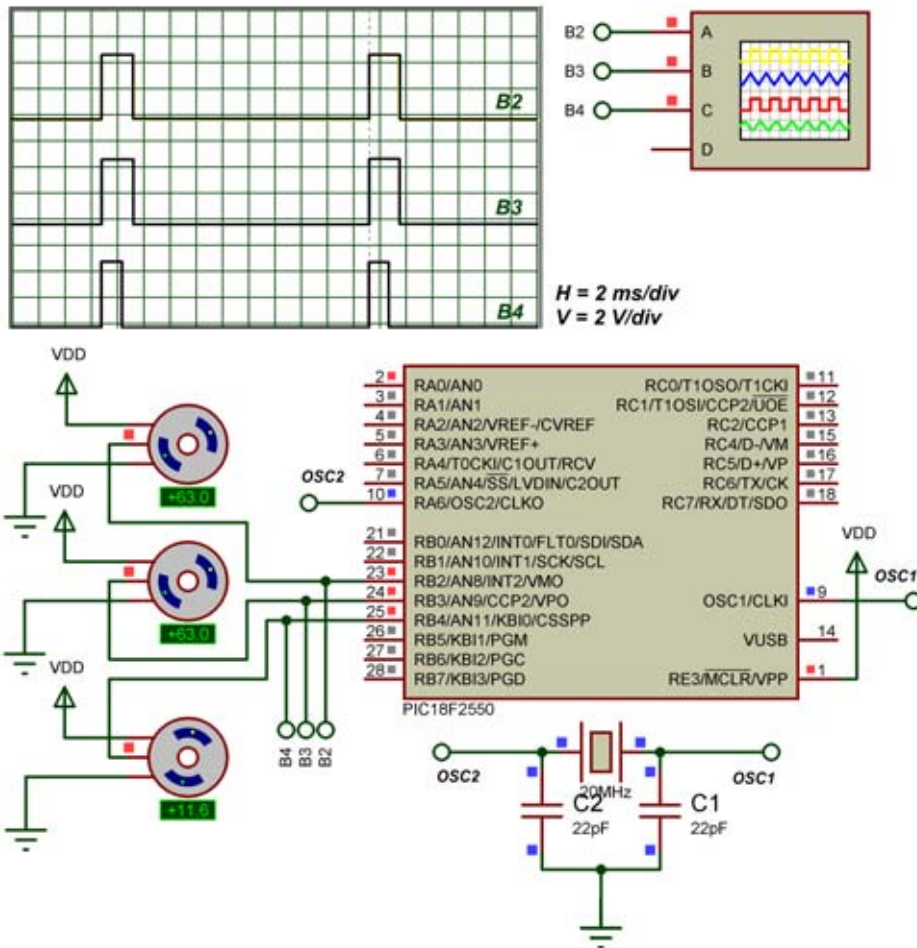


Fig. 1. Project simulation in Proteus VMS

4. Discussion

The described test case generates a PWM signal at 50 Hz. The signal at such a frequency is widely used in remotely controlled vehicles for hobbyists.

The proposed technique might be used in designing supplementary actuating devices for RC aircraft. In addition, this report might be found useful by developers who are less experienced in the interrupt technique.

References

1. PIC PWM Calculator & Code Generator. <http://www.micro-examples.com/public/microex-navig/doc/097-pwm-calculator.html> (date accessed 10 December 2017).
2. PIC18F2455/2550/4455/4550 Data Sheet, Microchip Technology Inc., 2006.

Appendix: Source code, MikroC Pro for PIC v.6.6.3

```
unsigned short counter = 0, motor1 = 0, motor2 = 0, motor3 = 0;

//Timer1: Prescaler 1:1; TMR1 Preload = 64896; Actual
//Interrupt Time: 128 us
void InitTimer1(void) {

    T1CON = 0x01;
    TMR1IF_bit = 0;
    TMR1H = 0xFD;
    TMR1L = 0x80;
    TMR1IE_bit = 1;
    INTCON = 0xC0;

    return;
}

void hereGoesMyISR(void) {
    if (TMR1IF_bit == 1) { //Check if Timer1 has
//overflowed
        TMR1IF_bit = 0; //Reset Timer1 flag
        TMR1H = 0xFD;
        TMR1L = 0x80;

        counter++; //Increase counter by 1
        //156 interrupts * 128 us = 19968 usec
        if (counter == 156) { //Check if interrupt was
//triggered 156 times
            PORTB.F2 = 1; //Start pulse to servo motor 1
            PORTB.F3 = 1; //Start pulse to servo motor 2
            PORTB.F4 = 1; //Start pulse to servo motor 3
            counter = 0; //Reset counter
        }
        if (counter == motor1) //Check if time to end left
//servo pulse
            PORTB.F2 = 0; //End pulse to left servo motor
        if (counter == motor2) //Check if time to end right
//servo pulse
            PORTB.F3 = 0; //End pulse to right servo motor
```

```

        if (counter == motor3) //Check if time to end right
servo pulse
            PORTB.F4 = 0;      //End pulse to right servo motor
        }
    return;
}

void interrupt(void) {
    hereGoesMyISR();
}

void main() {

    CMCON = 0x07; //disables comparators
    ADCON1 = 0x0F; //disables analogue functions
    GIE_bit = 1; //Enable global interrupts
    TRISB.F2 = 0; //Set up Port B2 as an output
    TRISB.F3 = 0; //Set up Port B3 as an output
    TRISB.F4 = 0; //Set up Port B4 as an output
    TRISA.F0 = 0; //Set up Port A0 as an output
    PORTA.F0 = 1;

    InitTimer1();

    while(1) { // Set up infinite loop
        motor1 = 6; // Falling edge after 6 interrupts *
//128 us each = 768 us
        motor2 = 6;
        motor3 = 6;
        Delay_ms(500);
        motor1 = 18; // Falling edge after 16 interrupts
//* 128 us each = 2048 us
        motor2 = 18;
        motor3 = 12; // Falling edge after 12 interrupts
//* 128 us each = 1536 us
        Delay_ms(500);
    }
    return;
}

```

ГЕНЕРИРАНЕ НА ШИРОЧИННОИМПУЛСНО МОДУЛИРАН СИГНАЛ ЧРЕЗ ПРЕКЪСВАНЕ ОТ ТАЙМЕР НА МИКРОКОНТРОЛЕР PIC18F2550

К. Методиев

Резюме

В настоящия доклад се разглежда подход за генериране на широчинноимпулсно модулиран (ШИМ) сигнал посредством микроконтролер PIC18F2550. Предложената техника използва т. нар. вътрешно прекъсване от таймер. Това решение може да се използва в автоматизиран процес, като изпълнително звено, например за задвижване на сервомотор. Въпреки че контролерът разполага с модул за генериране на ШИМ сигнал, този модул е зависим от честотата на кристалния осцилатор. В повечето случаи е трудно да се генерира ШИМ сигнал на ниски честоти. Показано е, че предложеното решение е гъвкаво и подходящо за задвижване на сервомотори, широко използвани от ентусиасти в радиоуправляеми модели.

Специално внимание е отделено на особеностите на програмата за микроконтролера. Допълнително е направена компютърна симулация. Използван е софтуер MikroC Pro for PIC и Proteus VMS. Показано е, че предложеното решение функционира със задоволителна точност. Кодът на програмата също така е публикуван в настоящата статия.

DEVELOPMENT OF ADVANCED SPACE SCIENCES AFTER FIRST ARTIFICIAL SATELLITE. 60-TH ANNIVERSARY OF THE SPACE AGE

Peter I. Y. Velinov

*Space Research and Technology Institute – Bulgarian Academy of Sciences
e-mail: pvelinov@bas.bg*

Abstract

The development of the various space sciences has been demonstrated since the launch of the first artificial Earth's satellite "Sputnik 1" on 04 October 1957. A number of data and characteristics for this satellite are presented in the present work.

There are also the first discoveries (1957–1958) in space age – the van Allen-Vernov radiation belts of the Earth. The history of radio observation of "Sputnik 1" in the 22-day period – 04–26 October 1957, of satellite transmitter operation was presented.

The first radio measurements in Bulgaria were made by Dr. G. Nestorov (later professor and correspondent member of BAS) from the Special department established at the beginning of 1957 in the Research Institute for Communications - Radio-measuring Control and Ionospheric Center – RIKIC. Dr. G. Nestorov makes measurements of the effect of Doppler and determines the height of the satellite. He finds that during the second and third week, "Sputnik 1" begins to noticeably reduce its height due to its drag and friction with the substance in the upper atmosphere.

Subsequently, after 1958, optical, laser and radar observations of artificial satellites on Earth began to take place in Bulgaria. During the period 1958–1959 three observation stations were set up – in Sofia, Stara Zagora and Varna. These observations continue until 2002, when they are gradually ceased to be done due to a lack of funding and the moving of the world observation centers to a higher technological level.

Introduction

The year 2017 marks the 60th anniversary of the arrival of the space age. On 4 October 1957, our planet's first artificial satellite, "Sputnik 1" (Russian for "satellite") – Fig. 1, was launched into low-Earth orbit by the Soviet Union. Although little more than a radio beacon, it showed the world that intercontinental ballistic missiles (ICBMs), at the core of Cold War military arsenals, could also place satellites into space. A mere month later, on 3 November, Soviet scientists launched a much larger and more sophisticated spacecraft – "Sputnik 2", the

second satellite sent into orbit and the first with a live animal – the dog *Laika*; a model with a doll stand-in is pictured in Fig. 2. The event was timed to coincide with the eve of the 40th anniversary of the Bolshevik Revolution.

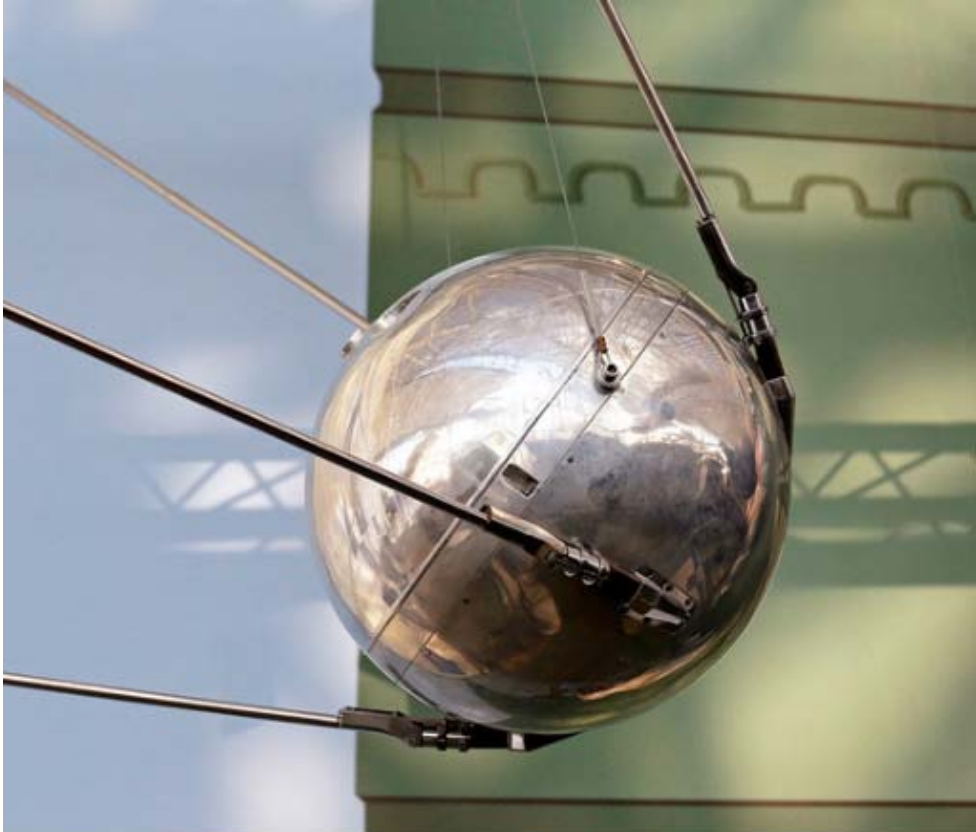


Fig. 1. A replica of Sputnik 1, the first artificial satellite in the world to be put into outer space: the replica is stored in Russian National Museum of the First Flight



Fig. 2. Sputnik 2 was a 4-meter-tall, cone-shaped capsule designed to remain attached to the rocket that launched it into orbit on 3 November 1957. It held radio transmitters, a telemetry system, a Geiger counter, and a temperature-control system for the cabin, which carried the dog Laika. The model shown here is now at the Polytechnical Museum in Moscow.

The arrival of the space age has led to the creation and development of a number of new space sciences: aeronautics and astronautics or cosmonautics - aerospace engineering, space navigation, space communications, space astronomy, space physics, space weather and space climate, space climatology, extrasolar planetary systems, exoplanetology, space chemistry or cosmochemistry, cosmic ray physics, heliospheric physics, planetary magnetospheres and ionospheres, Earth's space environment, space geophysics, space meteorology, space medicine and biology, micro-g environment research, space dosimetry, aerospace technology, space materials science, space dynamics, remote sensing from space, space exploration, space colonization, space law, and many others. With the help of these advanced space sciences humanity began confidently the exploration of space. But these studies led also to numerous new technologies and applications to improve people's lives.

Sputnik-1 proclaimed the arrival of space age on 4 October 1957

"Sputnik 1" ("Satellite-1", or "PS-1", Простейший Спутник-1, "Elementary Satellite 1") was the first artificial Earth satellite. The Soviet Union launched it into an elliptical low Earth orbit on 4 October 1957 at 19:28:34 UTC. The satellite had an initial orbit with perigee 228 km and apogee 939 km (eccentricity 0.05201), an inclination of 65.1 degrees and a period of 96.2 minutes [1, 2].

It was a 58.5 cm diameter polished metal sphere, with four external radio antennas to broadcast radio pulses. Its radio signal was easily detectable even by radio amateurs, and the 65° inclination and duration of its orbit made its flight path cover virtually the entire inhabited Earth.

Tracking and studying "Sputnik 1" from Earth provided scientists with valuable information, even though the satellite wasn't equipped with sensors. The density of the upper atmosphere could be deduced from its drag on the orbit, and the propagation of its radio signals gave data about the ionosphere.

"Sputnik 1" was launched during the International Geophysical Year from Site No.1/5, at the 5th Tyuratam range, in Kazakh SSR (now known as the Baikonur Cosmodrome). The satellite travelled at about 29 000 km per hour (8 100 m/s), taking 96.2 minutes to complete each orbit. It transmitted on 20.005 and 40.002 MHz, which were monitored by radio operators throughout the world. The signals continued for 21 days until the transmitter batteries ran out on 26 October 1957. Sputnik burned up on 4 January 1958 while reentering Earth's atmosphere, after three months, 1 440 completed orbits of the Earth, and a distance travelled of about 70 million km.

At 19.9 seconds after engine cut-off, PS-1 separated from the second stage and the satellite's transmitter was activated. These signals were detected at the IP-1

station by Junior Engineer-Lieutenant V. G. Borisov, where reception of Sputnik 1's "beep-beep-beep" tones confirmed the satellite's successful deployment. Reception lasted for two minutes, until PS-1 fell below the horizon. The Tral telemetry system on the R-7 core stage continued to transmit and was detected on its second orbit.

The designers, engineers and technicians who developed the rocket and satellite watched the launch from the range. After the launch they drove to the mobile radio station to listen for signals from the satellite. They waited about 90 minutes to ensure that the satellite had made one orbit and was transmitting, before the chief constructor of Sputnik 1 academician Sergej Korolev called Soviet premier Nikita Khrushchev.

On the first orbit the Telegraph Agency of the Soviet Union (TASS) transmitted: "As result of great, intense work of scientific institutes and design bureaus the first artificial Earth satellite has been built". The R-7 core stage, with a mass of 7.5 t and a length of 26 m, also reached Earth orbit and was visible from the ground at night as a first magnitude object following the satellite. Deployable reflective panels were placed on the booster in order to increase its visibility for tracking. The satellite, a small, highly polished sphere, was barely visible at sixth magnitude, and thus more difficult to follow optically. A third object, the payload fairing, also achieved orbit. The core stage of the R-7 remained in orbit for two months until 2 December 1957, while "Sputnik 1" orbited for three months, until 4 January 1958.

The surprise success of "Sputnik 1" precipitated the American Sputnik crisis and triggered the Space Race, a part of the Cold War. The launch ushered in new political, military, technological, and scientific developments. The USSR's launch of "Sputnik 1" spurred the USA to create the Advanced Research Projects Agency (ARPA, later DARPA) in February 1958 to regain a technological lead.

The success of "Sputnik 1" seemed to have changed minds around the world regarding a shift in power to the Soviets. In whole world the media and people initially reacted with a mixture of fear for the future, but also amazement about humankind's progress. Many newspapers and magazines heralded the arrival of the Space Age. After a month on November 3, 1957 the Soviet Union launched a second spacecraft containing the dog *Laika*. It became clear that the first man's flight into space was coming.

Construction

The chief constructor of "Sputnik 1" at OKB-1 was Sergej Pavlovich Korolev. The satellite was a 585-millimetre diameter sphere, assembled from two hemispheres that were hermetically sealed with o-rings and connected by 36 bolts (Fig. 3, 4). It had a mass of 83.6 kg. The hemispheres were 2 mm thick, and were covered with a highly polished one-millimeter thick heat shield made of aluminium-magnesium-titanium AMG6T alloy – "AMG" is an abbreviation for "aluminium-magnesium" and "T" stands for "titanium"; the alloy is 6 % magnesium and 0.2 % titanium. The satellite carried two pairs of antennas designed by the Antenna Laboratory of OKB-1 led by Mikhail V. Krayushkin. Each antenna was made up of two whip-like parts: 2.4 and 2.9 m in length, and had an almost spherical radiation pattern, so that the satellite beeps were transmitted with equal power in all directions, making reception of the transmitted signal independent of the satellite's rotation [1, 2].



Fig. 4. The structure inside the satellite "Sputnik 1". The model shown here is now at the Polytechnical Museum in Moscow.

The power supply, with a mass of 51 kg, was in the shape of an octagonal nut with the radio transmitter in its hole. It consisted of three Ag-Zn batteries, developed at the All-Union Research Institute of Current Sources (VNIIT) under

the leadership of Nikolai S. Lidorenko. Two of these batteries powered the radio transmitter and one powered the temperature regulation system. The batteries had an expected lifetime of two weeks, and operated for 22 days. The power supply was turned on automatically at the moment of the satellite's separation from the second stage of the rocket.

The satellite had a one-watt, 3.5 kg radio transmitting unit inside, developed by Vyacheslav I. Lappo from NII-885, the Moscow Electronics Research Institute, that worked on two frequencies, 20.005 and 40.002 MHz. Signals on the first frequency were transmitted in 0.3 sec pulses (under normal temperature and pressure conditions on-board), with pauses of the same duration filled by pulses on the second frequency. Analysis of the radio signals was used to gather information about the electron density of the ionosphere. Temperature and pressure were encoded in the duration of radio beeps. A temperature regulation system contained a fan, a dual thermal switch, and a control thermal switch. If the temperature inside the satellite exceeded 36 °C the fan was turned on and when it fell below 20 °C the fan was turned off by the dual thermal switch. If the temperature exceeded 50 °C or fell below 0 °C, another control thermal switch was activated, changing the duration of the radio signal pulses. "Sputnik 1" was filled with dry nitrogen, pressurized to 1.3 atm. The satellite had a barometric switch, activated if the pressure inside the satellite fell below 130 kPa, which would have indicated failure of the pressure vessel or puncture by a meteor, and would have changed the duration of radio signal impulse.

While attached to the rocket, "Sputnik 1" was protected by a cone-shaped payload fairing, with a height of 80 cm. The fairing separated from both Sputnik and the spent R-7 second stage at the same time as the satellite was ejected. Tests of the satellite were conducted at OKB-1 under the leadership of Oleg G. Ivanovsky.

First discoveries in space

The first Russian and USA artificial satellites discovered Earth's radiation belts. J. van Allen (USA) discovered inner radiation belt by the satellites "Explorer 1" and "Explorer 3" (1958) and S. N. Vernov (USSR) discovered outer radiation belt with the satellites "Sputnik 2" and "Sputnik 3" (1957–1958) [3, 4].

Since properly interpreting the data from the Explorer and Sputnik satellites, scientists have wondered about the radiation belts' origins. It was obvious that cosmic rays themselves had too much momentum to become trapped. Soviet scientists Sergej Vernov and Alexander Lebedinsky of MSU proposed that when cosmic rays bombard Earth's atmosphere, they could produce nuclear reactions that create neutrons, which subsequently decay into electrons and protons that are then trapped by the planet's magnetic field [4]. The proposal was the first physical model to explain the nature of the radiation belts. Vernov and Lebedinsky

announced the neutron-decay mechanism in July 1958, only a few months after the belts' discovery. Just two weeks later, US scientist Fred Singer independently published a description of a similar mechanism [4].

Space surveillance and tracking in Bulgaria

In 1956 the Soviet government addressed the Bulgarian government with a recommendation to start space research in Bulgaria in view of the future Russian program. In 1957, Dr. Eng. Georgi Nestorov (then Professor and Corresponding Member of the Bulgarian Academy of Sciences - BAS) [5–8] was commissioned to create in 1957 a special department to the Research Institute for Communications - Radio-measuring Control and Ionospheric Center – RIKIC. In this department he attracted the future academicians – then young engineers, Kiril Serafimov and Dimitar Mishev, who grew up as scientists with world renown.

The Ionospheric Center began studying the propagation of radio waves in the ionosphere, using mainly the A+ method. Immediately after the launch of first artificial satellite on the Earth in orbit on October 4, 1957, RIKIC began to receive the signals from the on-board transmitter "Mayak" and analyze the Doppler Effect. With some interruptions, the study of the integral electron content in the ionosphere by BAS scientists continues to this day [9–11].

Nestorov measurements of the Doppler Effect: the satellite travels in a well-known path and broadcast their signals on two known radio frequencies 20.005 and 40.002 MHz. The received frequencies will differ slightly from the broadcasting frequencies due to the satellite movement relative to the receiver. By monitoring this frequency shift over a short period of time, the receiver can determine its location to one side or the other side of the satellite, and several such measurements combined with the exact knowledge of the satellite orbit can determine a certain position, for example, the height of the satellite.

Nestorov found that during the second and especially in the third week, "Sputnik 1" began to noticeably decrease its height due to its drag and friction with the substance in the upper atmosphere. Nestorov's proposed method of determining altitudes of satellites can be widely used in space research.

Subsequently, after 1958, optical, laser and radar observations of artificial satellites on Earth began to take place in Bulgaria. During the period 1958–1959 three observation stations were set up – in Sofia, Stara Zagora and Varna [12].

The visual, photographic and laser observations in Bulgaria continue until 2002, when they are gradually ceased to be performed due to a lack of funding and the moving of the world observation centers of the satellites to a higher technological level [12].

World Space Week (WSW)

On December 6, 1999, The United Nations General Assembly declared World Space Week as an annual event celebration to be commemorated between 4–10 October. The choice of dates was based on recognition of two important dates in space history: the launch of the first man-made Earth satellite "Sputnik 1" on October 4, 1957 and the signing of the Outer Space Treaty on October 10, 1967. World Space Week is the largest annual space event in the world. In 2017, World Space Week was celebrated with over 3 700 events in 80 countries. Events included school activities, exhibitions, government events, and special activities at planetaria around the world.

Each year, a theme for World Space Week is established by the World Space Week Association. Under the theme "Exploring New Worlds in Space", many events of World Space Week 2017 focused on plans for human exploration of space and recent discoveries of Earth-like planets in nearby solar systems.

In 2018, the theme for World Space Week will be "Space Unites the World". This in part recognizes the historic UNISPACE+50 gathering to be held in Vienna this year. UNISPACE I held in Vienna from 14 to 27 August 1968. This was the first major space conference of the United Nations on the occasion of the 10th anniversary of space age.

References

1. SPUTNIK–1. October 4, 1957: Dawn of the Space Age. <https://www.space.com/17888-first-satellite-sputnik-1-explained-infographic.html> (accessed 20 December 2017)
2. Wade, M., Encyclopedia Astronautica, 2017. URL: www.astronautix.com
3. Stern, D.P., M. Peredo, The Exploration of the Earth's Magnetosphere, 12. The radiation belt – history, 2004. URL: <http://www.phy6.org/Education/whradbel.html>
4. Baker, D., M. Panasyuk, Discovering Earth's radiation belts, Physics Today, 2017, 70 12, 46–56. DOI: 10.1063/PT.3.3791
5. Несторов, Г., М. Топалов, Предавателна, антена и УКВ техника, Държавно издателство „Наука и изкуство“, София, 1955.
6. Несторов, Г., Разпространение на УК Вълни. Държавно издателство „Медицина и физкултура“, София, 1958.
7. Несторов, Г., Физика на ниската йоносфера. Издателство на Българската академия на науките, София, 1969.
8. Велинов, П., Г. Несторов, Л. Дорман, Воздействие космических лучей на ионосферу и распространение радиоволн, Издательство Болгарской Академии Наук, София, 1974.
9. Andonov, B., Vertical Total Electron Content and receiver bias calculations for Balkan Peninsula GNSS stations, C. R. Acad. Bulg. Sci., 2017, 70, 12, 1719–28.
10. Velinov, P.I.Y., S. Delistoyanov, D. Mishev, G. Nestorov, and Chr. Spassov, Ionospheric TEC measurements by informational radioline of satellite "Meteor-Prroda", In: Remote Sensing of Earth by Satellite "Meteor-Prroda", St. Peterbourg, Gidrometeoizdat, 1985, 145–151.

11. Mukhtarov, P., B. Andonov, and D. Pancheva, Empirical model of TEC response to geomagnetic and solar forcing over Balkan Peninsula. *Journal of Atmospheric and Solar-Terrestrial Physics*, 2018, 167, 80–95.
12. Ognyanov, O., Y. Shopov, P. Getsov, P. Malgova, A. Stoev, S. Kusun, and A. Pertcov, History, present and perspectives of space surveillance and tracking, In: *Proceedings of SES'2017*, 2017, 95–100.

РАЗВИТИЕ НА СЪВРЕМЕННИТЕ КОСМИЧЕСКИ НАУКИ СЛЕД ПЪРВИЯ ИЗКУСТВЕН СПЪТНИК НА ЗЕМЯТА. 60 ГОДИШНИНА НА КОСМИЧЕСКАТА ЕРА

П. Велинов

Резюме

Представено е развитието на различните космически науки след изстрелването на първите изкуствени спътници на Земята. Дадени са редица данни и параметри на първия изкуствен спътник „Спутник 1”. Показани са и първите открития на космическата ера – радиационните пояси на Земята, открити от ван Ален и Вернов. Представена е и историята на радио наблюденията на „Спътник 1” в 22-дневния период на работата на спътниковия предавател, 04–26 октомври 1957 г.

Първите радиоизмервания в България са направени от д-р Г. Несторов (впоследствие професор и член-кореспондент на БАН) от създаденото в началото на 1957 г. специално звено към Научно-изследователския институт по съобщенията – Радио-измервателен контролен и йоносферен център (РИКИЦ). Д-р Г. Несторов прави измервания на ефекта на Доплер и определя височината на спътника. Той установява, че през втората и особено през третата седмица „Спътник 1“ започва да намалява чувствително височината си поради триенето си с веществото във високата атмосфера.

Впоследствие, след 1958 г. в България започват да се провеждат оптически, лазерни и радарни наблюдения на изкуствени спътници на Земята (ИСЗ). През периода 1958–1959 г. се създават три наблюдателни станции – в градовете София, Стара Загора и Варна. Тези наблюдения продължават до 2002 г., когато постепенно те престават да бъдат извършвани поради липса на финансиране и преминаване на световните наблюдателни центрове на по-високо технологично ниво.

NEW HOT SPOT FOR HIGH-GROWTH EUROPEAN MARKETS FOR SATELLITE SERVICES

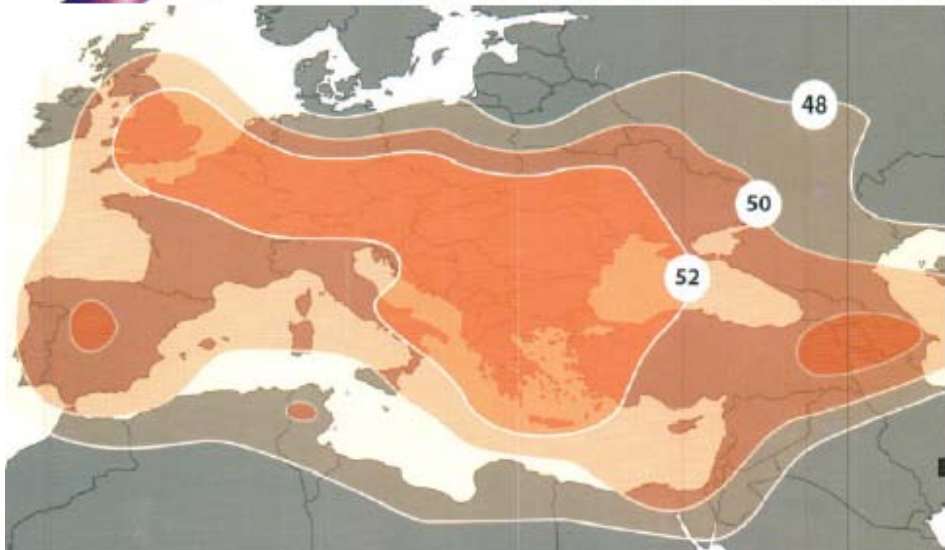
“Bulgaria Sat” EAD is a Bulgarian licensed satellite operator. Bulgaria Sat’s first commercial satellite, BulgariaSat-1 mission is to develop a new “hot-spot” at a nominal position 1.9°E for DTH operators and video markets across the Europe, Middle East and South Africa.

BulgariaSat-1, manufactured by Space System Loral (SSL) and based on SSL’s high quality and reliability 1300 series platform, was launched on June 23, 2017 by SpaceX from Cape Canaveral. Its payload comprises of over 30 Ku-band BSS and FSS transponders meeting the current demand for high quality HDTV and Ultra HDTV broadcasting.

BulgariaSat-1@1.9°E



 **BulgariaSat**
A NEW STAR FOR THE
EUROPEAN BROADCASTERS



The satellite is designed to cover with high power the Balkans, Turkey, West and East Europe, Middle East, North Africa and Caucasus with its European beam. In addition, the satellite is equipped with a spot beam, which can be used to provide extra capacity over the Balkans, or over Southern Africa.